UNIVERSIDAD DE CHILE
FACULTAD DE CIENCIAS FÍSICAS Y MATEMÁTICAS
DEPARTAMENTO DE GEOLOGÍA

MAGMATIC EVOLUTION THROUGH MELT INCLUSIONS OF THE HOLOCENE ALKALINE LAVAS OF PUYUHUAPI VOLCANIC GROUP, CHILEAN SOUTHERN ANDES

TESIS PARA OPTAR AL GRADO DE MAGÍSTER EN
CIENCIAS, MENCIÓN GEOLOGÍA
MEMORIA PARA OPTAR AL TÍTULO DE GEOLOGA

MARIANA ALEJANDRA WONG AGUIRRE

PROFESORA GUÍA:

CLAUDIA CANNATELLI

MIEMBROS DE LA COMISIÓN:

DOLORINDA DANIELE

DANIEL MONCADA DE LA ROSA

JAMIE BUSCHER

SANTIAGO DE CHILE

2019

RESUMEN DE LA MEMORIA PARA OPTAR AL TÍTULO DE:

Geóloga y grado de Magíster en Ciencias, mención geología.

Por: Mariana Alejandra Wong Aguirre

Fecha: octubre 2019

Profesora guía: Claudia Cannatelli

"GEOCHEMICAL EVOLUTION THROUGH MELT INCLUSIONS OF THE HOLOCENE ALKALINE LAVAS OF PUYUHUAPI VOLCANIC GROUP, CHILEAN SOUTHERN ANDES, AYSEN REGION"

Los nueve centros eruptivos menores del grupo volcánico Puyuhuapi (PVG) ubicados en el segmento sur de la Zona Volcánica sur, se distribuyen en dos lineamientos, siguiendo una de las trazas principales de la zona de falla Liquiñe – Ofqui, estructura mayor (>1000 km de extensión) de rumbo NS. Sus productos son de composición basáltica y de afinidad alcalina.

El principal enfoque de este estudio es determinar condiciones y procesos pre-eruptivos registrados por las lavas en cuanto a su mineralogía y a la petrografía de las inclusiones vítreas y determinar que procesos magmáticos generan variabilidad en la composición de los distintos centros eruptivos. Para ello se analizan inclusiones vítreas alojadas en fenocristales de olivino, utilizando distintas metodologías como Microsonda electrónica, ablación laser y espectroscopia Raman.

Se encontraron variados tipos de inclusiones que se distinguieron por su forma y composición entre homogéneas y recristalizadas. Inclusiones homogéneas muestran fraccionamiento y reequilibrio con el mineral hospedante, por lo que la composición inicial del magma parental tuvo que ser modelada.

La temperatura pre-eruptiva máxima registrada por las inclusiones vítreas es de 1280°C y la presión mínima se encuentra entre 4-5 Kbar, condiciones obtenidas a partir del equilibrio con el mineral hospedante y con la presión de vapor de CO_2 y H_2O retenido en las inclusiones. Lo que implica la existencia de un reservorio donde se detectaron procesos de fraccionamiento temprano de olivino y contaminación cortical, preferentemente en el lineamiento norte.

Diferencias sistemáticas en la composición de los centros eruptivos, sugiere que el magma que forma las lavas PVG se genera a partir de dos fuentes de manto diferentes, en el campo de estabilidad del granate como se sugiere para las altas razones de LILE/HFSE. El cono Puyu 9 del lineamiento norte tendría una fuente magmática más profunda con un contenido de granate mayor, evolucionando químicamente de manera independiente al lineamiento sur. Menor enriquecimiento en elementos incompatibles y mayor contenido de magnesio muestran que el magma que forma el cono Puyu 4, sería el magma más primitivo del PVG.

La firma geoquímica particular de las lavas alcalinas de PVG estaría más influenciada por la fusión sedimentos que de fluidos de la placa subductante, lo que es consistente con los bajos grados de fusión parcial (Nb/Y, La/Sm elevados) que producen volúmenes pequeños de magma.

AGRADECIMIENTOS

En primer lugar, quiero agradecer a mi familia y en especial a mis padres, Gilda y Fernando por todo el apoyo y amor que me han brindado, por creer en mí y enseñarme que ningún desafío es demasiado grande si hace con perseverancia y dedicación; mis hermanas Javiera y Valentina, por el infinito apañe, porque somos el triángulo perfecto y no podría pedir mejores brothers en este mundo; Cristian mi querido cuñi, por ayudarme cada vez que lo necesité y los vinitos de viernes; a mis abuelos, Darío, Nelly, Carlos y Carmen, todos ellos pilares fundamentales en mi vida.

Agradezco al proyecto CONICYT-FONDAP 15090013, Centro de Excelencia en Geotermia de los Andes (CEGA), ya que mis estudios fueron financiados por la Beca de Magíster y por el financiamiento otorgado para la obtención de las muestras, diversos análisis, pasantías y congresos a los que asistí.

Agradezco a todos los profesores del departamento de Geología con los que me cruce en estos años, de cada uno me llevo aprendizajes, en especial agradezco a mi profesora guía Claudia Cannatelli por creer en mi desde el día uno, por su apoyo a toda hora y por motivarme a sacar la mejor versión de mí. A los profesores de la comisión Daniel Moncada, Jamie Buscher y Linda Daniele, por su cooperación en el desarrollo de este trabajo, por sus correcciones y preguntas desafiantes, ingredientes clave para el desarrollo de la tesis.

A los funcionarios del Departamento de Geología, especialmente Blanca Baccola, Maritza Acuña y Rosita por su incansable ayuda y por resolver mis dudas siempre amables y cariñosas. A Roberto, por recibirme siempre con una sonrisa y por haber hecho que el trabajo de laboratorio fuera siempre grato.

A todos mis amigos y compañeros que hecho en este camino que comenzó el año 2010 en Bachillerato, lugar donde conocí a quienes hoy son mis grandes amigas, Javi, Pati, Ale, Caro, Lore y Maca, por esas noches de no estudio en la casa de la Javi y por estar siempre. A mis compañeros y amigos de generación, Natu, Cami Lizana, Marta, Inca, Aquiles, Coni Bravo, Ara, Franco, Fran Sandoval, Fonseca, Guille, Fonsi, Naty, España, etc. En especial Mati Paredes por los cafecitos y lindas conversaciones. Domi Kausel, gracias por ayudarme en etapas clave de la tesis, por las risas y todos los stickers. También a los chi@s de Post grado, en especial a los inclusionistas Lore, Cami Pineda, Fabi, Marce por la linda cooperación que nos hemos dado entre todos.

Y, por último, pero no menos importante a Phía Bustamante, por todo tu amor, por darle luz a mi vida y por acompañarme en esta titánica misión.

Tabla de Contenido

Índice de figuras

Índice de tablas

CAPÍTULO 1:

INTRODUCCIÓN

1.1 Estructura de la tesis

El presente trabajo se centra principalmente en estudiar los procesos pre-eruptivos que quedan registrados en inclusiones vítreas alojadas en fenocristales de olivino. El **capítulo 1**, se expone una breve introducción teórica de lo que son las inclusiones vítreas y la información que podemos obtener de su análisis geoquímico. También se expone de manera breve las principales características del volcanismo monogenético y por último se exponen las metodologías utilizadas para el cálculo de las condiciones termodinámicas del sistema.

El **capítulo 2** consiste en un manuscrito de artículo científico, escrito en inglés, el cual será posteriormente modificado para ser sometido a una revista científica internacional. El contenido corresponde a los resultados, discusiones y principales conclusiones que se desprenden del estudio.

1.2 Motivación (Formulación del problema)

Sistemas volcánicos de pequeña escala, en su mayoría basálticos, son una de las formas de magmatismo más extendidas en el planeta, aunque la cantidad de material extruido es baja, composiciones primitivas de magma son más propensas a encontrarse en estos centros eruptivos menores (MEC), ya que se caracterizan por un estadío magmático breve en la corteza.

El grupo volcánico de Puyuhuapi (PVG), ubicado en la Región de Aysén y formado por nueve centros eruptivos monogenéticos de composición basáltica y afinidad alcalina se disponen sobre una de las trazas principales de la Zona de Falla Liquiñe-Ofqui (Cembrano and Hervé, 1993), un importante sistema estructural, que representa un fuerte control estructural del volcanismo cuaternario a lo largo de la Zona Volcánica sur, que facilitaría la circulación de fluidos y el ascenso magmático a través de la corteza. Sumado a lo anterior, el PVG representa una zona de interés al tratarse de volcanismo postglacial (Holoceno) en un área que tiene un alto potencial geotérmico, con manifestaciones termales con temperaturas en superficie de hasta 80°C (Hauser, 1989)

Se propone estudiar el PVG en cuanto a geoquímica y petrografía, teniendo como enfoque principal las inclusiones vítreas alojadas en cristales de olivino, con el fin de obtener la composición del magma parental que formó las lavas del grupo volcánico y las condiciones pre-eruptivas del magma.

¿Qué rol desempeña la ZFLO en el área de estudio, ¿bajo qué condiciones termodinámicas se forman los fenocristales?, ¿el magma habría ascendido directamente desde profundidades mantélicas o hubo un periodo de asentamiento en la corteza?, ¿El magma que formo el PVG corresponde a una fuente única? Son algunas de las preguntas a las cuales se intentará dar respuesta con el presente trabajo.

1.3 Objetivos

1.3.1 Objetivo general

Proponer un modelo petrogenético que describa las posibles fuentes y procesos pre-eruptivos necesarios para la formación del grupo volcánico Puyuhuapi

1.3.2 Objetivos específicos

-Determinar la mineralogía y petrografía de las lavas

-Determinar la composición química (elementos mayoritarios y trazas) de las inclusiones vítreas alojadas en olivino, a través de técnicas microanalíticas (EMPA y LAICPMS)

-Determinar el contenido de volátiles en el magma a través de análisis de espectroscopia Raman en las inclusiones vítreas alojadas en olivino

-Determinar la composición del magma parental

1.4 Hipótesis de trabajo

El estudio de inclusiones vítreas alojadas en fases que cristalizan en etapas tempranas del sistema magmático, como por ejemplo el olivino, brinda una fuente de información importante sobre la composición de magmas primitivos y las condiciones en que se forma. Esta información, al ser complementada con la composición de los minerales, nos permite estimar condiciones de temperatura, presión y de oxidación/reducción del magma parental necesarias para generar modelos termodinámicos de evolución. Centros eruptivos menores con depósitos de similar composición y bajo contenido de fenocristales pueden compartir un mismo reservorio magmático. Por el contrario, fuentes distintas, evolución magmática independiente, variable participación de fluidos producto de la subducción o distintos grados de contaminación cortical, pueden registrarse en heterogeneidades preservadas en las inclusiones vítreas alojadas en los fenocristales.

1.5 Fundamento teórico

1.5.1 Que es una inclusión vítrea y como de forman

Las inclusiones vítreas (MI, por su sigla en inglés *melt inclusion*) son pequeñas parcelas de magma (típicamente <100 µm en la dimensión más larga) atrapadas en cristales durante su

crecimiento dentro de sistemas magmáticos (Sorby, 1858). Audétat and Lowenstern (2014) definen como inclusión vítrea a fundidos atrapados durante el crecimiento de cristales magmáticos que contienen >50 % de fases silicatadas disueltas. En sistemas volcanicos las inclusiones vitreas consisten en vidrio + una o mas burbujas $\pm$ fases de minerales hijos. Se denomina cristal hijo a todos aquellos que cristalizan a partir del fundido de la MI, de lo contrario si el mineral es previo, se denomina cristal atrapado.

Las inclusiones se atrapan generalmente debido a irregularidades en la superficie de los cristales. En la **Fig. 1**, se detallan los principales mecanismos de atrapamiento (Roedder, 1979). Cambios repentinos en las condiciones del magma, como una despresurización pueden aumentan el grado de supersaturación, y causar el crecimiento de un borde esqueletal que luego al cubrirse con el crecimiento cristalino puede atrapar zonas de inclusiones (**Fig. 1.a**; Roedder, 1979), también un aumento de temperatura u otros desequilibrios podría generar periodos de rápida disolución mineral, dando lugar a la textura *sieve*, común en cristales de plagioclasa. En general los desequilibrios se dan por etapas de alta tasa de crecimiento seguido de una etapa de crecimiento lento, permitiendo el atrapamiento de inclusiones a lo largo de las zonas de crecimiento (Audétat and Lowenstern, 2014).

Solidos que cubran el cristal en crecimiento pueden quedar atrapados y pueden causar el atrapamiento de magma (**Fig. 1.b**), estas inclusiones minerales son útiles para determinar que el magma se encontraba saturado, al menos localmente, con respecto a esta fase. Un mecanismo común en la formación de inclusiones en olivino es por defectos localizados en la interfaz del cristal, quedando inclusiones distribuidas al azar en el cristal hospedante (**Fig. 1.c**).

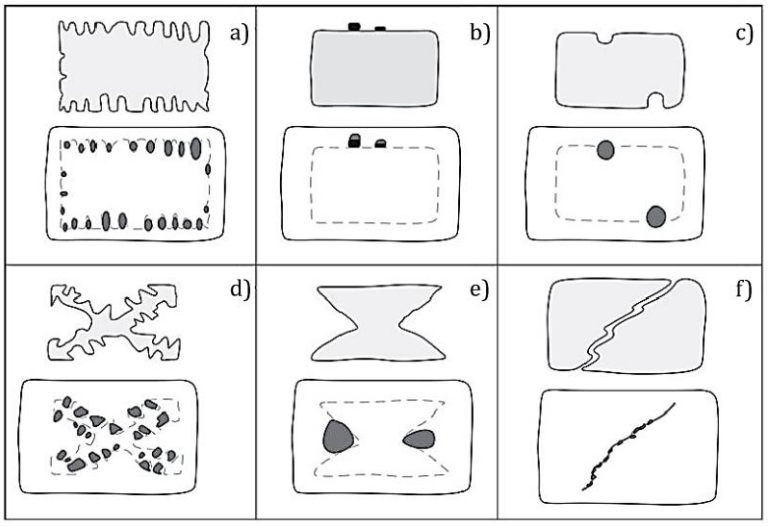

Fig. 1: Ilustraciones esquemáticas de mecanismos comunes de formación de inclusión vítreas relevantes para rocas basálticas. Las imágenes superior e inferior en cada panel representan fases tempranas y posteriores en el crecimiento de los cristales. Imagen modificada de (Kent, 2008). a) Por desarrollo de un borde esqueletal, b) otros cristales que se apoyan en la superficie, c) defecto localizado en la interfaz del cristal, d) crecimiento dendrítico, la distribución de las inclusiones siguen la orientación cristalográfica, e)

Continuación Fig. 1: crecimiento esqueletal en cristales tolva, inclusiones con localización geométrica, f) vidrio rellenado fracturas, inclusiones pequeñas que definen una superficie.

Las inclusiones proporcionan una posibilidad única de reconstruir la composición química de un magma (fundido silicatado + vapor) en una etapa específica de su evolución, desde su formación a la profundidad del manto hasta su ascenso y liberación en la superficie (Frezzotti, 2001), esto debido a que en su mayoría se forman previo a que ocurran procesos como desgasificación, fraccionamiento, mezcla de magmas y asimilación cortica, que puede alterar en gran medida la composición final del magma (Kent, 2008).

Las MI se comportan como sistemas cerrados y aislados, conservando potencialmente la composición original del fundido (incluido su contenido volátil), sin embargo, podrían no ser representativas de la composición original atrapada debido a procesos ocurridos en la interfaz con el cristal hospedante o por heterogeneidades del magma a micro escala. Incluso cuando las MI son representativas del fundido circundante en el momento de la captura, los procesos posteriores al atrapamiento pueden modificar o comprometer la composición inicial (Cannatelli et al., 2016).

Los cambios físicos y compositivos en las inclusiones vitreas después de su formación son comunes, incluso en rocas volcánicas. El grado de modificación es más bajo para las inclusiones que surgieron poco después de su atrapamiento (Audétat y Lowenstern, 2014). El proceso llamado cristalización posterior al atrapamiento (PEC) es la cristalización de la fase del huésped en la pared de inclusión y comenzará una vez que la inclusión quede atrapada y la temperatura disminuya antes de la erupción. Esta es una consecuencia inevitable del enfriamiento del sistema de vidrio-huésped y ocurrirá en todas las inclusiones vítreas (Danyushevsky et al., 2002; Kent, 2008). Durante el enfriamiento y cristalizacion post atrapamiento, la cristalización de la masa fundida incluida continúa a lo largo de la interfaz fundido-cristal, agotando la masa fundida en constituyentes que entran en la fase cristalina y enriqueciéndola en elementos incompatibles en el cristal. Puede ocurrir difusion de H+ atraves del cristal hospedante, que resulta en la perdida de H_2O (Hauri, 2002; Massare et al., 2002; Severs et al., 2007 Gaetani et al., 2012)

A medida que la MI y el cristal se enfrian el volumen ocupado por la masa fundida disminuira más que el del fenocrital, debido a sus diferentes propiedades de expansion termica, es decir el fundido silicatado se contrae mas que el criatal hospedante, produciendo una disminución de la presión interna, lo que causa una la nucleacion de una burbuja y la perdida de volatiles desde el fundido hacia la burbuja (Roedder, 1979; Moore et al., 2015; Wallace et al., 2015).

Al poder reconstruir el contenido de volatiles del magma, las inclusiones perminten determinar las condiciones de P-T al momento del atrapamieto. Ya que la solubilidad del H_2O y CO_2 en el magma es fuertemente dependiente de la presion (Aster et al., 2016), la concentracion de ambos

puede ser utilizada para calcular la profundidad minima de atrapamiemto basado en una temperatura conocida del magma y asumiendo que este estaba saturado en fluidos (Audétat and Lowenstern, 2014)

1.5.2 Rocas intrusivas de Batolito Nor-Patagónico

El Batolito Patagónico, que se extiende por más de 1300 Km (40-56° S) es producto de la amalgamación de plutones que representan actividad ígnea extendida por *ca.* 150 Ma a lo largo del margen occidental de América de Sur (Pankhurst et al., 1999). El Batolito Patagónico norte corresponde a la parte más septentrional, al norte del Golfo de Penas (47°S; Hervé et al., 1993)

Al sur de los 44°S las rocas plutónicas expuestas son típicamente, granodioritas y tonalitas de hornblenda y biotita y escasos cueros de leucogranitos de biotita. Afloran principalmente a ambos lados de canal Moraleda y fiordos transversales asociados como los fiordos Puyuhuapi y Aysén. En el área de estudio se pueden distinguir dos unidades graníticas mayores, una diorítica y otra tonalítica.

1.5.2.1 Diorita Risopatrón, BMdr (Mioceno)

Unidad informal definida en la Investigación geológica minera ambiental de Aysén por SERNAGEOMIN-GORE Aysén (2011), aflora en el borde oriental del canal Puyuhuapi, hacia el norte del rio Oscuro y en los alrededores del puerto de Puyuhuapi, corresponde a un cuerpo ígneo, elongado en dirección NNE-SSW, las rocas características corresponden a dioritas mesocráticas a melanocráticas, equigranulares, de grano fino a medio, compuestas esencialmente por plagioclasa, anfíbola y escasa biotita, además de algunos cuerpos de granodioritas. En el puerto Puyuhuapi se presenta cortada por fallas normales (N65°-80°E/70°-85°S) y por diques microdioriticos (N103°E/45°S). Es común que esta unidad se encuentre intruida por diques de tonalita y se exprese, además, como inclusiones máficas en cuerpos tonalíticos.

Estudios petrográficos muestran presencia de plagioclasa sódica, euhedral a subhedral, zonadas y macladas. Los ferromagnesianos corresponden a cristales subhedrales de hornblenda verde, como accesorios se encuentran cuarzo y piroxeno. Antecedentes geocronológicos disponibles para esta unidad permiten asignarla al Mioceno, con un importante evento de deformación dúctil ocurrido en el Plioceno (Cembrano et al., 2002).

1.5.2.2 Tonalita Puyuhuapi, BMtp (Mioceno)

Corresponde a afloramientos de tonalitas y granodioritas y escasos cuerpos de leucotonalitas, equigranulares, de grano grueso a medio, leucocráticas a mesocráticas, compuestas, esencialmente, por plagioclasa, hornblenda, cuarzo y en menor medida biotita, con apatito, zircón

y titanita como minerales accesorios. Los afloramientos se distribuyen principalmente, al Sur-este de Rio Oscuro, como una franja N-S que es limitada por la traza principal del sistema de falla Liquiñe-Ofqui que define el canal de Puyuhuapi. Es común encontrar en esta unidad, inclusiones de diques microdioríticos y enclaves máficos centrimétricos a métricos de microdioritas y dioritas de grano fino.

Estudios petrográficos muestran la presencia de plagioclasa subhedral con zonación oscilatoria, la biotita es anhedral, mientras que la hornblenda se presenta con bordes corroídos y extinción ondulosa. Antecedentes geocronológicos permiten asignar esta unidad al Mioceno, con un importante evento de exhumación ocurrido en Plioceno y hasta posiblemente Pleistoceno superior (Pankhurst et al., 1999).

1.5.3 Volcanismo monogenético

Centros eruptivos menores (MEC) , en su mayoría basálticos, son una de las formas de magmatismo más extendidas en el planeta, ocurriendo en todos los ambientes tectónicos mayores (Cañón-Tapia and Walker, 2004) y producen magmas con un rango composicional desde insaturados en sílice hasta saturados y sobresaturados, dentro del espectro basáltico, SiO_2 wt.%. <53 (Mcgee and Smith, 2016).

Los volcanes monogenéticos ocurren como conos de escoria, conos y anillos de ceniza y maars, su expresión en la superficie terrestre ocurre de dos maneras: (1) como campos aislados de uno o varios MEC, en corteza que va desde una litosfera delgada (<30 Km) resultado de extensión a una litosfera normal a engrosada; (2) como conductos parasito a lo largo de zonas de dorsal o en flancos de volcanes poligenéticos mayores.

Los conos de escoria son volcanes que se forman por erupción de magma basáltico, de baja viscosidad en erupciones estrombolianas o hawaiianas y se forman en condiciones secas o a una razón agua/magma muy baja (<0,1). En cambio, los anillos de toba, conos de toba y maars son formados en ambientes subaéreos o en presencia de aguas superficiales. Ellos se generan desde una erupción freatomagmática debido a la mezcla de magma ascendente y agua superficial (Sigurdsson, 1999).

Un volcán monogenético según Németh and Kereszturi 2015 se define como un edificio volcánico con bajo volumen acumulado (típicamente $\leq 1Km^3$) que ha sido construido por una pequeña erupción continua o muchas discontinuas alimentadas por uno o múltiples lotes de magma a través de un sistema de dique alimentador relativamente simple y poco espaciado, con un sistema de cámara magmática poco desarrolladas.

A partir de estudios como los de McGee et al., 2015, 2012; Németh et al., 2003 y Smith et al., 2008 se ha determinado que existe una evolución sistemática en la composición del magma

durante el desarrollo de una erupción de un volcán monogenético. Muestreos a través de la secuencia estratigráfica de una secuencia volcánica revelan variaciones composicionales que serían el resultado del fraccionamiento del magma a nivel profundo, cercano a la fuente (Smith et al., 2008).

Por otro lado, también se ha encontrado que hay una significante correlación positiva entre el volumen de magma de un pulso individual y su composición dentro del espectro basáltico.

En genera volúmenes de magma menores tienen composiciones en el extremo de bajo SiO_2 y alto álcalis del espectro, mientras que los volúmenes más grandes tienden hacia composiciones menos alcalinas y más saturadas de sílice. (McGee and Smith, 2016).

Debido a que están involucrados volúmenes de magma muy pequeños y su existencia en la superficie requiere un ascenso rápido desde la fuente mantélica, las erupciones monogenéticas tienen el potencial de revelar características sutiles de procesos magmáticos que se enmascaran en sistemas más grandes como estratovolcanes, islas oceánicas y grandes provincias ígnea (McGee et al., 2013).

1.5.4 Condiciones de oxidación magmáticas

La fugacidad de oxigeno ejerce un importante control sobre la mineralogía y la composición de un basalto, es el resultado de la compleja historia de fusión parcial, extracción, ascensión y emplazamiento del magma (Herd, 2008). Su influencia en el transporte de metales y en la formación de óxidos magmáticos la convierten en una variable clave al estudiar la evolución magmática ya que esta varía durante la cristalización y exsolución de volátiles (Burgisser and Scaillet, 2007), cualquier cambio en la fugacidad de oxigeno debería dar como resultado un cambio en la relación redox de hierro tanto en los sólidos como en los líquidos, controlando la aparición de óxidos de Fe-Ti, silicatos ferro magnesianos, y la composición química del fundido coexistente (Carmichael y Ghiorso, 1990)

El estado redox de magmas derivados del manto varían con la configuración tectónica (Carmichael, 1991), trabajos como Eggins, 1993; Kelley and Cottrell, 2009; Wood et al., 1990 han sugerido que lavas de arco volcánico tienen un estado de oxidación significativamente mayor que el basaltos de dorsal oceánica (MORB). Evans 2012 determino fO_2 para basaltos de arco de 2 a 4 unidades sobre el buffer QFM (cuarzo-fayalita-magnetita), magmas ricos en K presentan los niveles más altos, con un ΔQFM de 2.9 $\pm$0.7 en promedio, superior a lo encontrado en magmas K-intermedios (2.1$\pm$0.6).

Existen varios métodos (oxibarómetro) para determinar la fO_2 en los basaltos, basados en la partición de hierro ferroso y férrico entre pares de óxidos, tales como los propuestos por Ghiorso y Sack, 1991; Lindsley y Frost, 1992; Lattard et al., 2005 aunque la limitación de estos es que los

óxidos de Fe-Ti como la titanomagnetita y la ilmenita en general aparecen tardíamente en la evolución de cristalización de los magmas basálticos y en rocas primitivas con poco fraccionamiento no se encuentran tales fases.

El oxibarómetro olivino-piroxeno-espinela fue desarrollado para su aplicación en xenolítos mantélicos en facies de espinela. Ballhaus et al. (1991) proporciona una calibración empírica del oxibarómetro de olivino-piroxeno-espinela de O'Neill y Wall (1987), usando pares de harzburgita de espinela y lherzolita sintéticas entre 1040 y 1300 ° C y 0.3 a 2.7 Gpa, el modelo se limita a fundidos primitivos, derivados del manto, y no es apropiado para basaltos más evolucionados. La ventaja de la formulación es que evita la necesidad de un cálculo explícito de la actividad del componente de magnetita en la espinela; sin embargo, se simplifica suprimiendo el ortopiroxeno usando la parte ideal de la actividad de fayalita en el olivino. No se puede esperar que esta simplificación sea válida en XFe Ol> 0.15.

1.5.5 Condiciones P-T de cristalización

Las condiciones temperatura se determinaron mediante el uso de geotermómetros de olivino – vidrio, basado en una relación empírica independiente de la presión propuesta por Putirka (2008), con un error asociado de 52° C.

Además, se utilizó el software de modelamiento Petrolog para reconstruir la composición inicial de las inclusiones y la respectiva temperatura de atrapamiento (Danyushevsky and Plechov 2011) El algoritmo simula en intercambio de Fe y Mg entre el olivino y el fundido de acuerdo al modelo de Ford et al., 1983, se compara el contenido de FeO en la inclusión con una cantidad especificada por el usuario, si la cantidad de FeO ingresada por el usuario es mayor que la contenida en la inclusión, el software simula un aumento de Temperatura y la consiguiente fusión de olivino, en el caso contrario ocurre cristalización de olivino en la pared de la inclusión lo que disminuye la cantidad de FeO y MgO en esta.

Para determinar las condiciones de presión, se estiman las presiones de saturación de vapor de las inclusiones utilizando la concentración de H_2O-CO_2 (**Fig. 2**)

La solubilidad de ambos volátiles en el magma dependen de la composición del fundido y de la temperatura, por lo que estos efectos también deben tenerse en cuenta al realizar los cálculos de presión de saturación de vapor (Metrich y Wallace, 2008).

Con modelos de solubilidad termodinámica (Papale et a., 2006) calibrados con datos experimentales, se puede calcular la solubilidad y la desgasificación de H_2O y CO_2 para fundidos nefeliníticos a basálticos y riolíticos.

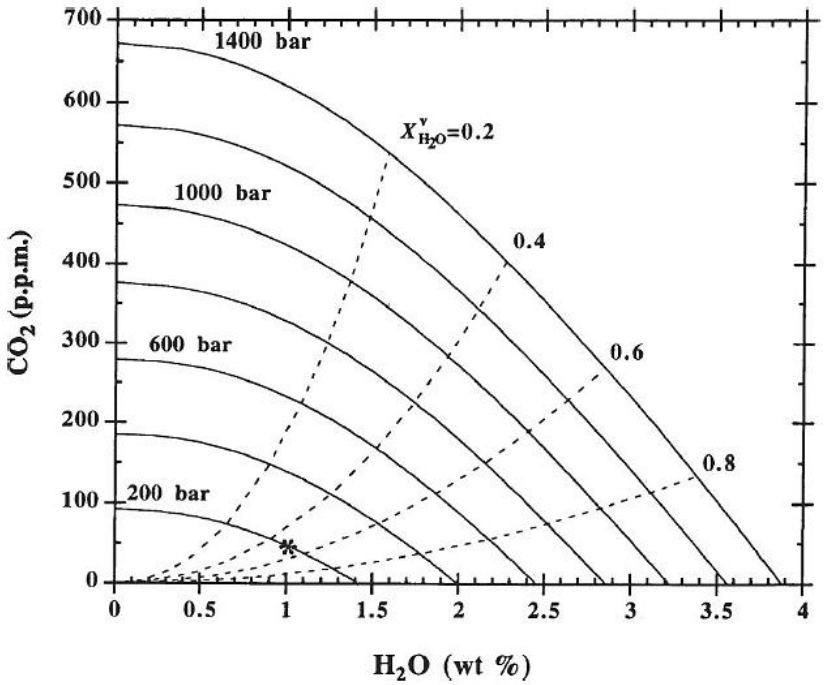

Fig. 2: Relación inversa de CO_2 - H_2O en fundido basáltico, saturado en vapor a 1200°C. Curvas continuas para cada presión constante (isobaras), línea discontinuas son corresponden a isopletas de composición de vapor. Ambas curvas calculadas usando modelos termodinámicos calibrados con datos experimentales (Dixon y Stolper, 1995). Figura de Metrich y Wallace, 2008.

1.6 Marco geológico y tectónico regional

El grupo volcánico Puyuhuapi (PVG) se localiza en la Zona Volcánica Sur (SVZ) de los Andes, en la comuna de Cisnes, en la región de Aysén (44°20'S y 72°34'W) y se puede acceder al área directamente por la carretera Austral R-7. Esta compuesto por un set de nueve centros eruptivos menores, de los cuales 4 estan alineados al borde noroeste del fiordo de Puyuhuapi, 4 estan alineados entre el poblado de Puyuhuapi y el lago Risopatrón, y uno se encuentra aislado en el borde este del fiodo de Puyuhuapi, a unos 6 Km al sur del pueblo. Los dos lineamientos tienen una orientación de N40°E y se separan por una distancia de 2Km (Lahsen et al., 1994).

El arco volcánico Los Andes, es el resultado de la subducción de las placas oceánicas Nazca y Antártica bajo la placa continental Sudamericana, que se contactan en el punto triple de Chile, punto que se ha movido hacia el norte a lo largo del margen continental desde el Mioceno aproximadamente hace 14 Ma, momento en el cual la Dorsal de Chile, que separa las placas Nazca y Antártica, alcanzó el margen continental.

El arco de los Andes se subdivide en cuatro segmentos conocidos como Zonas Volcánicas Norte, Central, Sur y Austral, estas zonas a su vez se dividen en segmentos menores por diferencias en

la distribución del volcanismo y diferencian es la composición de los productos volcánicos. Los segmentos de mayor escala con volcanismo activo ocurren en zonas donde el ángulo de subducción es relativamente inclinado (25°) y entre ellos existen zonas en que el ángulo de subducción es relativamente plano (11°) donde el volcanismo está ausente (Pardo et al., 2002)

La SVZ, se ubica entre las latitudes 33º y 46ºS, se limita al norte por la subducción de la dorsal de Juan Fernández y al sur por la subducción de la dorsal de Chile. En este tramo la placa de Nazca subduce bajo el continente a una tasa de 7-9 cm/año que ha prevalecido durante los últimos 20 Ma (Pardo-Casas y Molnar, 1987), esta placa subduce en una dirección de 22-30º NE de la ortogonal con la trinchera, y el ángulo de subducción aumenta de ~20° en el límite al norte a >25° hacia el sur. En consecuencia, la distancia del arco a la fosa varia de >290 Km al norte a <270 Km hacia el sur (Stern, 2004).

La subducción ligeramente oblicua de la placa de Nazca bajo la placa Sudamericana producen características geológicas complejas a lo largo del borde continental. En la SVZ los esfuerzos son acomodados a través de la zona de falla Liquiñe-Ofqui (LOFZ, Hervé 1994), esta se extiende por aproximadamente 1000 Km, entre las longitudes 38° y 47° S. La LOFZ es una megafalla intra-arco transcurrente dextral. Representada por lineamientos de rocas cataclásticas y miloníticas con dirección NNE-SSW, NE-SW y NNW-SSE, y fracturas de orientación preferente N50°-60°W y N50°-70°E que la cortan transversalmente (Cembrano et al., 1996).

Esta estructura favorece la ubicación de muchos edificios volcánicos a lo largo de su traza principal y ramas asociadas (**Fig. 3**). La distribución de la mayoría de los MEC está controlada por la traza de la LOFZ. Los basaltos de olivino de algunos MEC podrían representar alguna de las rocas más primitivas de todo el arco volcánico de Los Andes (López-Escobar y Moreno, 1994).

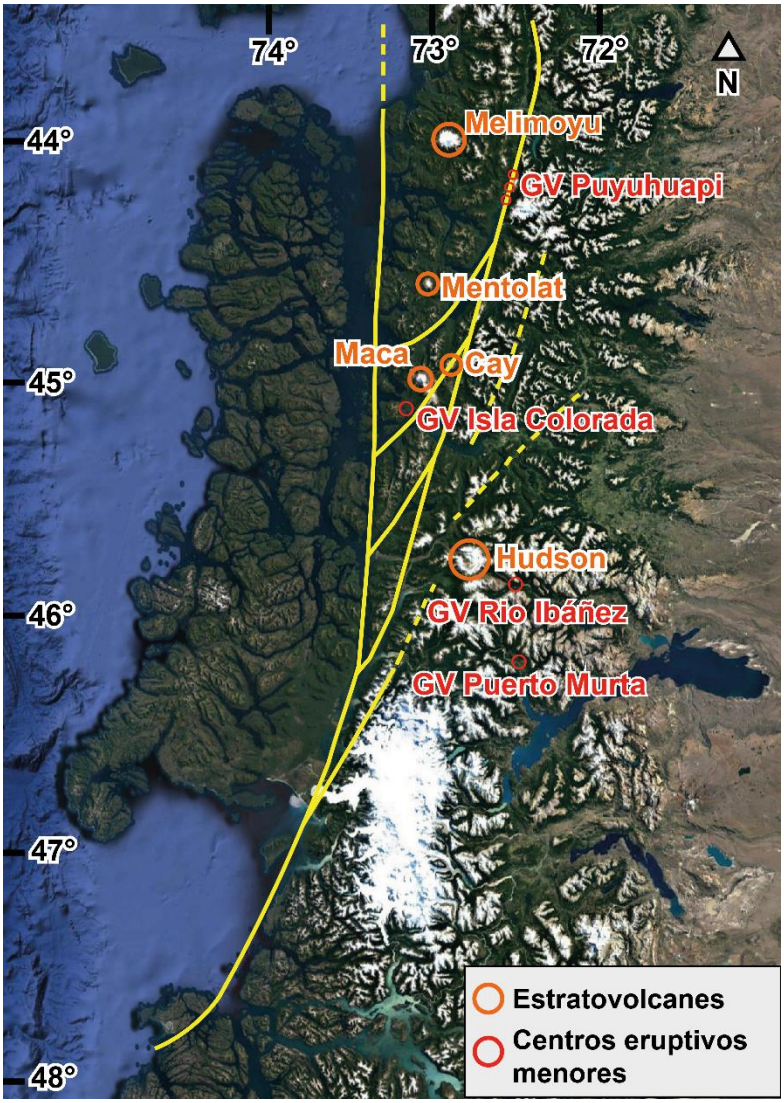

Fig. 3: SSVZ con las principales trazas de la LOFZ y la ubicación de diferentes edificios volcánicos. Imagen modificada de Cembrano y Lara (2009)

La SVZ incluye al menos unos 60 edificios volcánicos, del tipo estratovolcán (SV), histórica y potencialmente activos, además de 3 complejos de calderas silícicas y cientos de centros eruptivos menores, distribuidos en las provincias norte (NSVZ= 33,0°-34,5° S), transicional (TSVZ= 34,5°-37,0° S), central (CSVZ= 37,0°-41,5° S) y sur (SSVZ= 41,5°-46,0° S). (Stern, 2004). A lo largo de la SVZ, en las provincias centro y sur, el volcanismo es activo e intenso, el ancho del arco volcánico es de aproximadamente 80 Km (en la CSVZ) y 40 Km (en la SSVZ), y la actividad volcánica post glacial ha sido continua con erupciones en volcanes del tipo SV y MEC. Las rocas son predominantemente basaltos y basalto andesitas, aunque algunos SV exhiben productos de intermedios a ácidos (López-Escobar and Moreno, 1994)

1.6.1 Geología del área de Puyuhuapi

A continuación, se presenta una descripción de la geología base realizada en el área de Puerto Puyuhuapi, por SERNAGEOMIN-GORE Aysén, 2011 (**Fig. 4**)

El área se caracteriza por una geomorfología dominada por un modelado glacial de serranías elevadas, con altitudes máximas del orden de 1.600 s.n.d.m. y pendientes abruptas, en ocasiones >45°, con valles glaciales profundizados por sistemas fluviales tardíos, estrechos y profundos. Además, posterior a la erosión glaciar, el paisaje ha sido modelado por actividad volcánica reciente. Lo anterior se ve representado por el valle glacial de orientación N-NW sobre el cual se localiza el lago Risopatrón, el cual fue represado por lo cono monogenéticos en estudio, y su continuidad hacia el sur se expresa en el Canal Puyuhuapi. Se reconocen tres unidades geológicas mayores: Rocas volcanosedimentarias y volcánicas, rocas Intrusivas de Batolito Nor Patagónico y Depósitos sedimentarios no consolidados

1.6.2 Rocas volcanosedimentarias y volcánicas.

1.6.2.1 Formación Traiguén, EMt (Eoceno-Mioceno)

Sucesión volcanosedimentaria (Espinoza y Fuenzalida, 1971; Fuenzalida y Etchart, 1975; Hervé, et al., 1995), compuesta por basaltos almohadillados, lutitas, areniscas y cherts, generalmente metamorfoseados y con enjambre de diques asociados. En el área de estudio los afloramientos se distribuyen, en el costado occidental del Canal Puyuhuapi en especial en el borde occidental de la Isla Magdalena, corresponden principalmente a lavas macizas, en algunos casos con litofacies de lavas almohadilladas (‘*pillow lavas*’) cuerpos gábricos y en menor proporción, tobas de lapilli y brechas volcánicas y areniscas. Estos se disponen en franjas discontinuas de orientación N-NE a S-SW, definiendo pliegues isoclinales de orientación semejante al eje del canal Puyuhuapi (137°/50°)

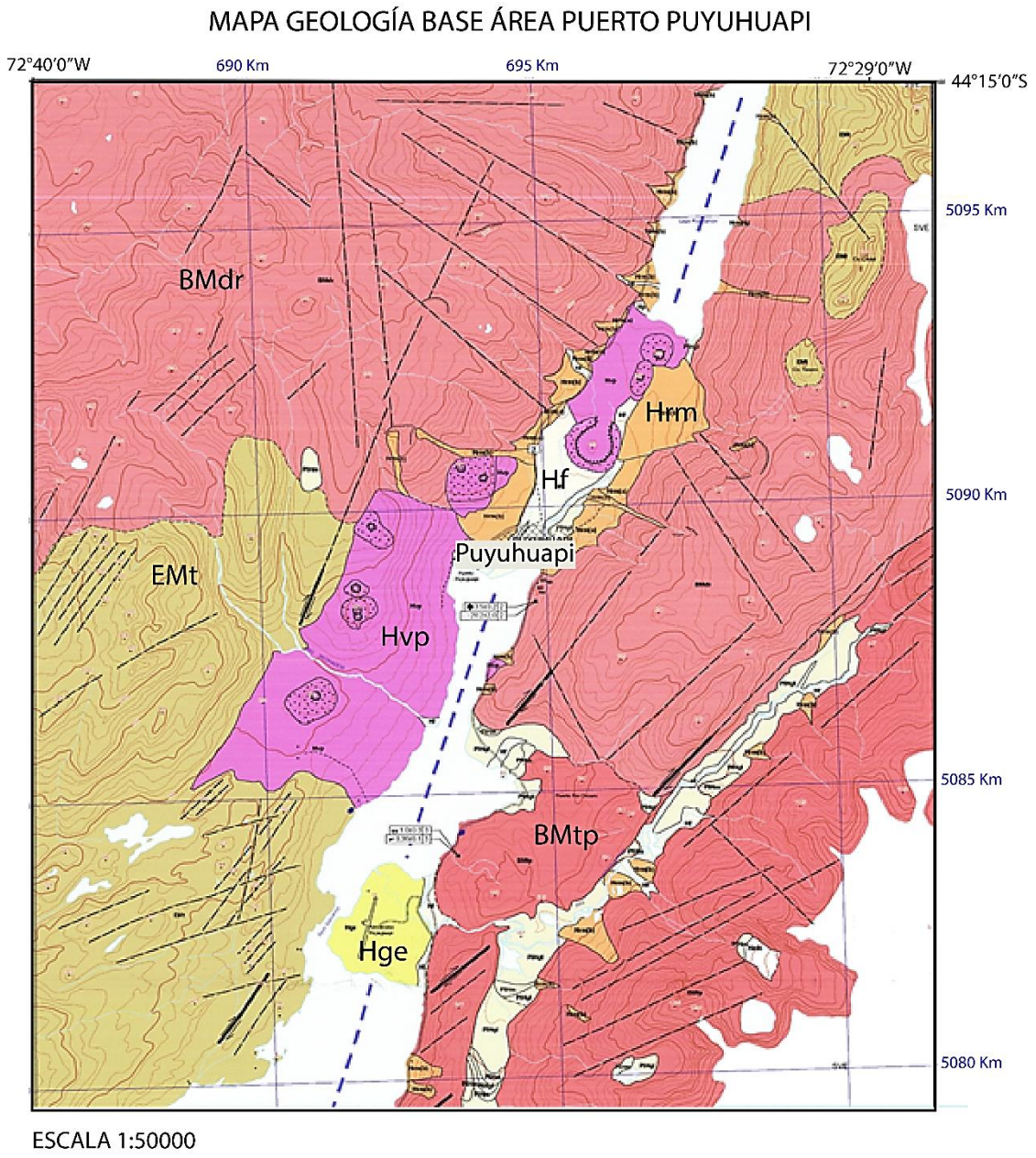

Fig. 4: Mapa geología base puerto Puyuhuapi. Fuente: Servicio nacional de Geología y Minería – Gobierno Regional de Aysén. Mella y Duhart (2011)

Estudios geocronológicos Rb-Sr en roca total permitieron asignar una edad de entre 46 y 20 Ma (Hervé, et al., 1995), sin embargo, estudios recientes U-Pb SHRIMP en circones detríticos han revelado una edad neógena para la Formación Traiguén.

1.6.2.2 Grupo volcánico Puyuhuapi, Hvp (Holoceno)

Grupo de al menos nueve centros eruptivos menores (Fuenzalida y Etchart, 1974; Lahsen et al., 1994) se disponen como centros aislados de conos de escoria y flujos de lava basáltica, que cubren una superficie aproximada de 9 Km^2. Los MEC están distribuidos dos lineamientos con dirección N40°E, consistente con una de las trazas principales del sistema de Falla Liquiñe – Ofqui. Uno de los lineamientos con cuatro MEC se emplaza en el borde NW del Fiordo Puyuhuapi

y el otro, a una distancia de 2 Km, también con al menos 4 MEC, se emplaza al norte del poblado Puyuhuapi hasta el Lago Risopatrón, además por el borde este del fiordo Puyuhuapi se observa un flujo de lava basáltica que desciende de lo alto de un acantilado, que habría eruptado también desde una fractura con dirección N40°E, falla llamada Puyuhuapi-Rio Frio. (Lahsen et al., 1994)

El grupo volcánico se encuentra emplazado en un basamento de tonalitas, dioritas y gabros que forman parte del Batolito Norpatagónico y se caracteriza por flujos de lavas menores y conos piroclásticos bien preservados, sin erosión glaciar, por lo que el complejo seria de edad post glaciar.

El material extruido de los conos son basaltos vesiculares de olivino, de textura porfídica con fenocristales de olivino magnésico y pequeños fenocristales de clinopiroxeno y plagioclasa cálcica, la masa fundamental va de hialopilítica a fluidal pilotaxítica y contiene microlitos de plagioclasa, gránulos de olivino, minerales opacos y vidrio basáltico. De acuerdo a su composición los basaltos de Puyuhuapi pueden ser considerados como calcoalcalinos ricos en K, aunque debido al alto contenido de Na, estas rocas también pueden ser consideradas como alcalinas (Lahsen et al., 1994).

En general la actividad que produjo estos centros eruptivos fue en una primera etapa fisural, en que se produjeron los flujos de lava y luego se volvió centralizada formando los conos piroclásticos, además es probable que la actividad del lineamiento norte haya sido sub-acuática (freatomagmática), lo que habría represado el canal Puyuhuapi, formando el lago Risopatrón.

1.6.3 Depósitos sedimentarios no consolidados

Corresponden a Depósitos de playa, fluviales, de remociones en masa, glacioestuarinos, morrénicos, glaciofluviales y glaciolacustres.

Los depósitos de playa (Hp), se encuentran en las playas al sur del poblado de Puyuhuapi, presentan buena selección, constituidos por guijarros redondeados, de tamaño variable y arenas gruesas y finas con laminación paralela y ondulitas en el fondo.

Los depósitos fluviales (Hf), generados por los cursos de actuales de agua, asociados a los márgenes de los ríos Ventisqueros y Pascua, están constituidos principalmente por gravas clastosoportadas e incluyen intercalaciones de lentes de arena, con estratificación cruzada o plana y de limos laminados y arenas indicando planicies de inundación.

Los depósitos de remociones en masa (Hrm) son de tipo diamicto, polimícticos a monomícticos, mal seleccionados, de tamaños variables clasto a matriz soportados. Se encuentran en zonas al pie de las laderas de alta pendiente y en la descarga de los cursos de agua desde dichas laderas,

formando morfologías de abanico de diferente magnitud y extensión, en el área de estudio se pueden observar en ambas vertientes del canal Puyuhuapi y en los valles secundarios interiores.

Los depósitos glacioestuarinos (Hge), localizados en los entornos del poblado de Puyuhuapi en el aeródromo, son bien seleccionados, caracterizados por una sucesión rítmica de limos y arena fina con laminación paralela y ondulitas de fondo, con intercalaciones de gravas, en ocasiones, se observan guijarros inmersos en una matriz soportada de arena fina, indicando un ambiente transicional entre estuario y glaciar.

Los depósitos morrénicos (PIHm)son macizos con mala selección, matriz a clasto soportado, polimícticos, compuestos por guijarros y bloques angulosos a subredondeados, localmente estriados y facetados, en una matriz de arena fina y limo. Se encuentran bien expuestos en los valles glaciares asociados a las descargas del nevado de Queulat en la porción superior del valle del rio Ventisquero.

Los depósitos glaciofluviales (PIHgf), están escasamente representados en el área, en los alrededores de los ríos Ventisquero y Oscuro, se componen de gravas, parcialmente imbricadas, moderadamente a bien seleccionadas, clasto a matriz soportadas, con clastos redondeados a subangulosos de tamaño guijarro, en una matriz de arena gruesa, intercaladas con lentes de arena, con estratificación planar y cruzada, y limos laminados.

Los depósitos glaciolacustres (PIHgl), se componen de una sucesión rítmica de arenas finas, limos y arcillas e intercalaciones menores de gravas. Se exponen en la ribera sur del Lago Risopatrón y en los valles glaciares colgados del Rio Ventisquero.

CAPÍTULO 2:

MAGMATIC EVOLUTION THROUGH MELT INCLUSIONS OF THE HOLOCENE ALKALINE LAVAS OF PUYUHUAPI VOLCANIC GROUP, CHILEAN SOUTHERN ANDES

Wong, M.[1*], Cannatelli, C.[1], Moncada, D.[2], Buscher J.[1], Frezzotti, M.L.[3], Morata, D[1]

1 Departamento de Geología y Centro de Excelencia en Geotermia de Los Andes (CEGA), Facultad de Ciencias Físicas y Matemáticas, Universidad de Chile, Chile

2 Departamento de Geología, Facultad de Ciencias Físicas y Matemáticas, Universidad de Chile, Chile

3 Department of Earth and Environmental Sciences, University of Milano-Bicocca, Milano, Italy

* Corresponding author: Centro de Excelencia de Geotermia de Los Andes (CEGA), Departamento de Geología, Facultad de Ciencias Físicas y Matemáticas, Universidad de Chile, Santiago 8370450, Chile. E-mail address: mariana.wong@ug.uchile.cl

Abstract

The Puyuhuapi volcanic group (PVG) comprises nine minor eruptive centers (MEC), located at 44°16'-44°22'S/72°31'-72°37'W. The centers are pyroclastic cones associated with limited lava flows, separated into two lineaments with a N40°E direction. Products of the PVG show an alkaline affinity whereas large active stratovolcanoes in this region have a calc-alkaline affinity. Two compositional groups associated with each lineament are inferred to belong to two magmatic sources. This study focuses on olivine-hosted melt inclusions (MI) to constrain the primitive magma composition and determine the igneous processes that caused the compositional differences between and along lineaments of the PVG.

The composition of the melt phase before the eruption was determined by analyzing the major, minor, trace element, and volatile contents of olivine-hosted MIs from four cones of the PVG. These results are combined with major and trace element compositions of the mineral host and whole rocks. Several types of MIs were observed and were classified according to petrographic characteristics. MIs show a spectrum of basaltic compositions from Mg# 55 to #Mg 68 and basanite to trachy basalt andesite. Olivine compositions vary from Fo_{75} to Fo_{87}, with some displaying resorption and/or reverse zoning.

The particular geochemical signature of the PVG alkaline lavas are expected to be influence largely by the melting of slab sediments rather than fluid input, which would be consistent with a low degree of melting. The lower amount of SiO_2 and greater amount of alkalis of Puyu 9, in

addition to the greater enrichment of incompatible elements (Sr, Zr, Rb), allow us to determine that Puyu 9 would not only have a deeper source of magma but was probably one of the first MEC to erupt.

2.1 Introduction

Melt inclusions (MIs) are small volumes of melt typically 1–100 μm in size, that are trapped in surface irregularities or defects of crystals during growth in a magma body (Sorby,1858), in volcanic rocks, silicate-melt inclusions consist of glass + one or more gas bubbles $\pm$ daughter mineral phases (Frezzotti, 2001). They can record pristine concentrations of volatiles and metals usually lost by degassing and fractionation during magma solidification (Audétat and Lowenstern, 2014)

Because melt inclusions trap silicate melts prior to eruptive degassing, they are useful recorders of melt volatile concentrations during crystallization (e.g. Lowenstern, 1995; Metrich and Wallace, 2008). However, during post-entrapment cooling and crystallization, the pressure within a melt inclusion decreases. This causes nucleation of a vapor bubble and loss of volatiles from the melt into the bubble. The pressure drop within a melt inclusion has a particularly strong effect on CO_2 because of its strong pressure-dependent solubility in silicate melts (Aster et al., 2016). Therefore, to access the initial volatile content it is necessary to measure them both in the glass and in the bubble.

When studying the composition of melt inclusions in early formation phases such as olivine it is more likely to obtain the parental magma composition. This study aims to determine pre-eruptive conditions and processes recorded by the lavas of different minor eruptive centers from the PVG, in terms of their mineral chemistry and the olivine-hosted melt inclusion composition to determine the origin and magmatic evolution.

Small eruptive centers representing short-lived, isolated eruptions are effectively samples of mantle heterogeneity over a given area, as they are generally of a basaltic composition and show evidence of little magmatic processing. This is particularly powerful in volcanic arcs where the original melting process generating stratovolcanoes is often obscured by additions from the down-going slab (fluids and sediments) and the overlying crust (McGee et al., 2017).

The PVG lavas represent a point of interest since they are almost the only products of alkaline signature in the arc of the Southern Volcanic Zone. Through this study, it is determined how small scale heterogeneities in the magma source can generate compositional changes in low volumes of magma.

2.2 Geologic background

The Andean Southern Volcanic Zone (SVZ) is a ~1400 Km-long volcanic chain whose activity has produced 60 Quaternary stratovolcanoes (SV) and numerous minor eruptive centers (MEC; Stern, 2004). The SVZ is the result of the subduction of the Nazca plate beneath the South American plate between latitudes 33°S and 46°S. The tectonic setting is characterized by slightly dextral-oblique convergence between the Nazca and the South American plates at a rate of ca. 7-9 cm/year that has prevailed for the last 20Ma (Cembrano and Lara, 2009).

This segment of the Andes reflects important variations from north to south in its composition and cortical thickness. Between 33° and 37°S, the basement is made up of extensive outcrops of Meso–Cenozoic volcano–sedimentary rocks and south of 38°S, volcanoes are built directly onto Meso–Cenozoic plutonic rocks of the Patagonian Batholith (Cembrano and Lara, 2009). The overriding plate thickness ranges from 25 to 60 Km, with an average of 25-30 Km between latitudes 42.5-45°S and 34-40 Km between latitudes 37-42.5° S, increasing systematically up to 60 Km northwards to latitude 33° S (Stern, 2004). In addition, the trench morphology changes from deep and sediment poor in the north to shallow and sediment filled toward the south (Voelker et al., 2013).

According to Thomson (2002) and references therein, large intra-arc strike slip faults are a common feature in the overriding plate where subduction convergence is oblique to the plate margin, and their existence can be explained by intraplate coupling causing partitioning of the convergence vector into two orthogonal components: trench orthogonal compression and trench-parallel strike-slip motion accommodated by discrete transcurrent faults. In the SVZ the stress is accommodated by the Liquiñe-Ofqui Fault Zone (LOFZ), a major intra-arc fault system with dextral transpresional displacement (Pankhurst et al, 1999).

Spatial volcanic distribution and differences in the geochemistry of the erupted rocks have been used to subdivide the SVZ into four arc segments (Lopez-Escobar et al., 1995), northern (NSVZ; 33°S–34.5°S), transitional SVZ (TSVZ; 34.5°S–37°S), central (CSVZ; 37°S–425°S) and southern (SSVZ: 42°S–46°S).

Based on magnetic anomaly patterns, the age of the subducting oceanic lithosphere on the SVZ varies from about 35 Ma in the north to zero age at the Chile Rise (Tebbens et al., 1997). In addition, the southern part hosts a number of fracture zones from north to south, named, Mocha, Valdivia, Chiloé, Guafo, Guamblin and Darwin (Weller and Stern, 2018). Fracture zones are likely to promote an enhanced transport of water via altered oceanic crust and possibly serpentinized mantle into the subduction system (Wehrmann et al., 2014)

Crustal deformation not only plays a significant role in magma migration, but it may a exert a fundamental control on magma differentiation processes that in turn can determine the nature and

composition of volcanism along and across continental margins (Cembrano and Lara, 2009). The distribution of most MEC are controlled mainly by the LOFZ, which are predominantly basaltic, and basaltic-andesites, which may represent some of the most primitive magmas erupted in the entire Andean range (Lopez-Escobar and Moreno, 1994).

In a summary of SVZ magmatism, López-Escobar et al. (1995a) divided all SVZ basaltic rocks into two types. Type 1, having low LREE/HREE common in largely basaltic CSVZ volcanoes and depleted in K and in other incompatible elements such as Rb, La and Th. Type 2, having higher LREE/HREE, that are K-rich and also enriched on incompatible elements, as found in back arc volcanoes, most NSVZ and TSVZ centers, and numerous MEC found along the LOFS in the CSVZ and SSVZ.

The Puyuhuapi volcanic group (PVG) comprises nine small basaltic centers located at 44°16'-44°22'S/72°31'-72°37'W, in the southernmost border of the SVZ, about 260 Km east of the Nazca-South American trench. PVG is composed by pyroclastic cones associated with limited lava flows, predominantly basaltic in composition (Gonzalez-Ferran et al., 1994), separated into two lineaments with a N40°E direction, following the principal trace of LOFZ (Hervé et al., 1995). According to López-Escobar et al., 1995a, Puyuhuapi lavas belong to Type 2 basalts.

2.3 Sample description and preparation

We collected lava samples from four MEC; labeled Puyu3, Puyu4, Puyu9 and Puyu18 (**Fig. 5**) Petrographic observations indicate that all samples are porphyritic basalts. The samples display different degrees of vesicularity and phenocrysts content, ranging from 7% for Puyu 3 and Puyu 18, 10% for Puyu 4 and 13% for Puyu 9.

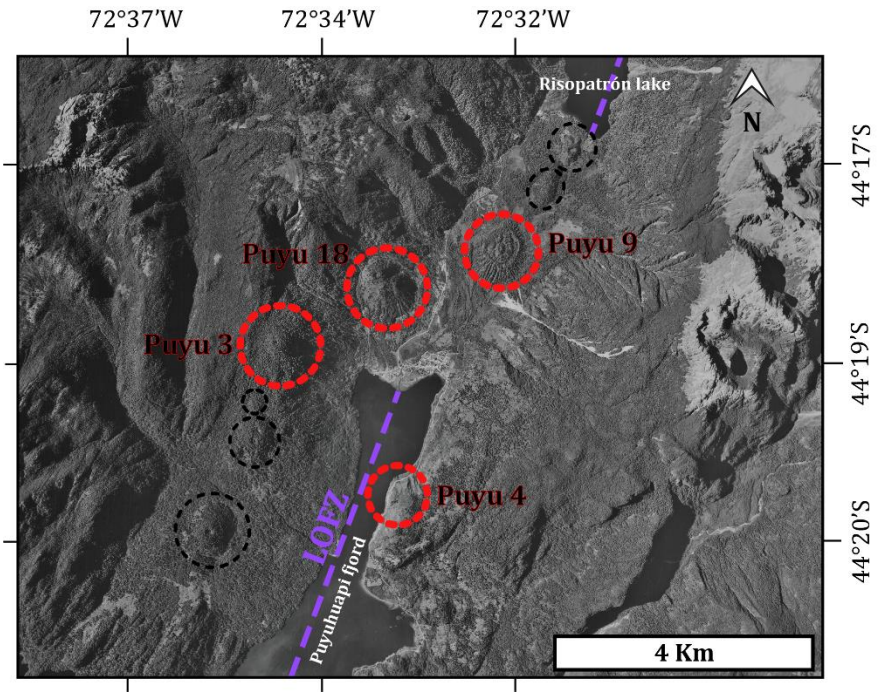

Fig. 5: satellite image with the location of the sampled eruptive centers (red circles), black circles: other minor eruptive centers of PVG. LOFZ: fault orientation from Mella and Duhart (2011). Source: servicio aerofotogramétrico – Fuerza Aérea de Chile

Puyu3, Puyu4 and Puyu18 samples display subhedral olivine (Ol) as the only phenocrysts phase (up to 2 mm in size), which it is often found forming glomerophyric aggregates or as isolated crystal, as well as microphenocrysts (0.03 mm). Generally, Ol contains numerous spinel inclusions and melt inclusions (MIs) in varying amounts. Some Ol show disequilibrium, as normal zoning and resorption that can occur in the core of the crystals or at the rim. Puyu 9 also presents subhedral Ol as phenocrysts together with euhedral to subhedral clinopyroxene (Cpx) microphenocrysts. Cpx, reaches just 1% in volume, and contains olivine and Fe-Ti oxides inclusions.

Plagioclase (Pl) is distinctly smaller than olivine, up to 0.2 mm on average, with some exceptions of 0.8 mm, but most are found as microlites. The intergranular groundmass generally contains anhedral Ol and Cpx, euhedral Pl and Ox, and very little glass. Puyu 9 is the only sample that differs from the others, by displaying an intersertal groundmass texture with a blackish iron-rich glass.

In order to study the mineralogy and geochemistry of collected Puyuhuapi lavas, we performed a petrographic study on thin sections to establish both the paragenesis of our collected rocks and the type of mineral phase hosting the MIs. Based on this first step, we crushed and sieved all samples in order to handpick Ol crystals and then mount them into 1 inch-round glass slides using an acetone-soluble resin. The obtained mounts were then polished with disks starting from 800 to 5000 grit, and then finishing with 0.1 µm alumina powder. We selected and analyzed crystals

containing homogeneous or recrystallized melt inclusions without cracks or other visually apparent defects.

The volume of each bubble and MIs were calculated using the open-source program ImageJ (Abràmoff et al., 2004), by measuring their dimensions from a photo. We assumed that bubbles were spherical and MIs were ellipsoidal in volume and calculated their volumes. The third, unobservable ellipsoidal axis (extending in and out of the plane of each photo) was estimated by using the smaller ellipsoidal axis measured on the photograph, following the procedure proposed by Aster et al. (2016).

2.4 Analytical procedures

We performed a detailed petrographic study of MIs by using a FEI Quanta 250 Scanning Electron Microscope (SEM) available at CEGA (Andean Geothermal Center of Excellence) in the Department of Geology at the University of Chile, to verify homogeneity of the glass and, in case of recrystallized MIs, to determine which minerals were present. Using backscattered electron (BSE) images, inclusions and their respective phases were characterized

Major element concentrations (Si, Al, Fe, Mg, Ca, Na, K, Mn, Ti, Cr, Ni, Cl and P) in MIs and host Ol were determined using an electron microprobe analyzer (EMPA) at the University of Milan (JEOL 8200 Super Probe) and at the LAMARX- National University of Cordoba (JEOL JXA-8230), with four detection crystals (TAP, PETJ, LIF and LIFH). Polished Ol grain mounts and thin sections were carbon-coated, and glass and minerals were analyzed with a 15-kV accelerating voltage. Minerals were analyzed with a focused beam, a beam current of 5 nA and a counting time of 10s for peaks and 5s for background. Volatile elements in MIs, such as Na and Cl, were analyzed first, with a 5nA defocused beam, to minimize loss from the glass. Counting times were 5-20 s on peak and 2.5-10 s. on background for major and minor elements. Water content in MIs was estimated by applying the difference method. With the obtained data, the structural formula of each mineral was calculated, using excel spreadsheets made for each phase (plagcalc, olicalc, pyxcalc, spincalc), obtained from http://www.gabbrosoft.org.

Trace element concentrations in MIs and minerals were obtained by Laser Ablation Inductively Coupled Plasma Mass Spectrometry (LA-ICPMS), using an iCapQ Thermo Scientific quadrupole at CEGA, in the Department of Geology at the University of Chile. Laser spot size was 10 to 25 µm for MIs and 20 µm for Ol, pulsed at 7 Hz, with a counting time of 10ms for each isotope. For every fifteen analyzed points, we used two check standards from the USGS, Nist SRM 610, as the primary one, and MRM BHVO-2 (basaltic glass).

Data reduction for recrystallized MIs was performed using the AMS software (Mutchler et al., 2008), which allows the determination of the concentration of the MI without knowing any major

oxide composition (i.e, without having an internal standard), assuming that the 44 measured elements represent 100 wt. % of the MI. We used the Iolite software program (Paton et al., 2011) to reduce data for homogeneous MIs analyzed by EMP, where we could use the known 29Si as an internal standard.

Whole-rock compositions were analyzed by XRF (major elements) and ICP-MS (trace elements) at Bureau Veritas Mineral Laboratories (Vancouver, Canada) using inductively coupled plasma–atomic emission spectroscopy and mass spectroscopy (ICP-ES, ICP-MS). The ICP-ES and ICP-MS analyses were carried out on lithium metaborate/ tetraborate fusions following dilute nitric acid digestion. Loss on ignition (LOI) was determined as the weight difference after ignition at 1000 °C. The detection limits for the analyses were between 0.002 and 0.1 wt. % for major elements, 0.01 and 5 ppm for trace elements, and 0.01 to 0.5 ppm for REE (rare earth elements). The accuracy and analytical precision of the measurement of major and trace elements were analyzed against standard reference material STD SO-19 and duplicate analyses for each sample. The iron redox state of two samples (Puyu 4 and Puyu 9) were determined by titration.

The density of CO_2 in each bubble was calculated with the densimeter equation proposed by Lamadrid et al. (2017), which uses the distance in wavenumber between the two characteristic peaks, called the Fermi diad located around 1285.4 cm^{-1} and 1388.2 cm^{-1} (Wright and Wang, 1973; 1975), As CO_2 density increases, the peaks of the Fermi diad shift farther apart

$$\rho = -36.42055 + (0.354812 \times \Delta) \quad (2)$$

Where ρ is the density of CO_2 (g/cm^3) and Δ is the Fermi diad splitting (cm^{-1}).

The splitting of the Fermi diad in the Raman spectrum of CO_2 was calibrated as a function of pressure and temperature, using a high-pressure optical cell (HPOC) in the Vibrational Spectroscopy Laboratory at Virginia Tech, using a JY Horiba LabRam HR (800 mm) spectrometer. The experimental set up is similar to the one used in Lamadrid et al., 2017. The Raman spectrometer was equipped with a 400-μm diameter confocal hole and the slit width was set to 150 μm. Excitation was provided by a 514nm (green) Laser Physics 100S-514 Ar and laser set at 50mW, with Raman shifted photons diffracted by an 1800 grooves/mm grating to an Andor electronically cooled open electrode 1024 × 512 pixel CCD. The mean value of three collections of 45 s each were taken to determine the Raman peak positions at each pressure. In some cases, the Fermi diad was outside of the range over which the equation of Lamadrid et al. (2017) is valid, or the peaks did not allow precise determination of the Fermi diad splitting.

2.5 Results

2.5.1 Mineral Chemistry

2.5.1.1 Mafic minerals

Olivine (Ol) is the most abundant and large mineral phase in all studied lavas. Ol compositions for all samples range from Fo_{74} to Fo_{87}, Table 1 shows compositional ranges for each sample, with forsteritic percentage calculated including the Mn content.

Table 1; Olivine compositions measured with electron microprobe. * Data obtained by LAICPMS

Sample	Phenocrysts size (mm)	Fo (%) core	Fo(%) rim
Puyu3	0.5-1.9	74-87*	80-84
Puyu4	0.5-1.6	82-87	81-86
Puyu9	0.5-2.6	75-87	78-84
Puyu18	0.5-1.9	83-86	77-84

Most Ol has sub-euhedral shapes and displays minor zoning on the rims. **Fig. 8 a-b-d** shows typical Ol phenocryst from Puyu 9, Puyu3 and Puyu18 respectively, with a very slight zoning at the rim, mineral inclusions and MIs. Some Ol present disequilibrium features such as partial resorption (i.e., embayments and dissolution zones) and/or reverse zoning. Olivine B21 from Puyu9 has a central resorption and reverse zoning (**Fig. 8d**) showing Fo_{77} at the core and Fo_{84} at the rim, olivine A21 from Puyu3 presents widespread resorption, and reverse zoning with Fo_{74} at the core and Fo_{80} at the rim (**Fig. 8 e**), suggesting dissolution and recrystallization processes.

We identified a bimodal composition for Ol in Puyu 9 and Puyu 3; these samples also had larger crystals than the others did, Puyu 4 shows a more limited compositional range, displaying mostly smaller crystals of higher Fo content. In all of the samples, Ol microlites occur as intergranular grains of 40-100 μm in size, with compositions in the Fo_{73} - Fo_{79} range, compositionally coinciding with the rims of phenocrysts.

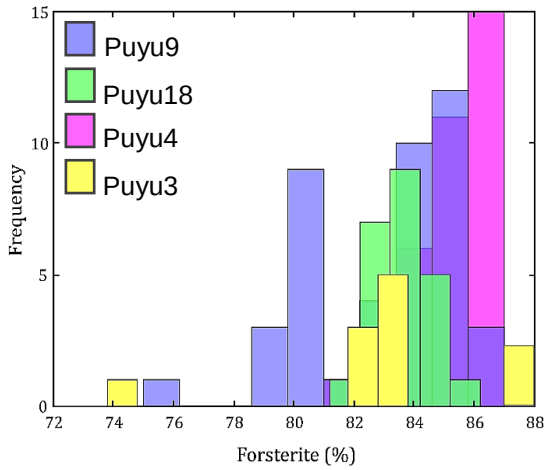

Fig. 6: Histogram of forsterite content for olivine, measured in the core of phenocrysts.

Puyu 18 and Puyu 4 present some phenocrysts with resorption but no reverse zoning, only compositional rims. Skeletal growth is present in some microlites from Puyu 4.

Cpx is very scarce; in Puyu9, phenocrysts and microphenocrysts do not exceed 1%, are diopside in composition, and are in the range of Wo_{43-50}, En_{35-45}, and Fs_{9-18}. Some crystals show sector and/or oscillatory zoning (**Fig. 8**) and mineral inclusions of Ol are common. It is not possible to recognize compositional families (**Fig. 7.a**), but rather a compositional gradation in the magnesium and iron content.

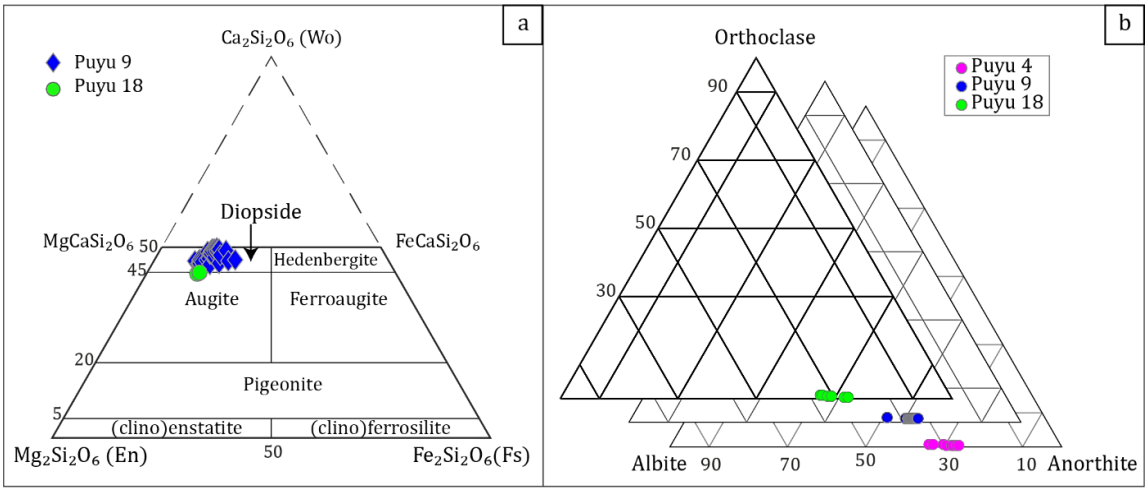

Fig. 7: (a) Cpx composition from samples Puyu9 and Puyu18 (microlites). (b) Pl compositions of the studied samples.

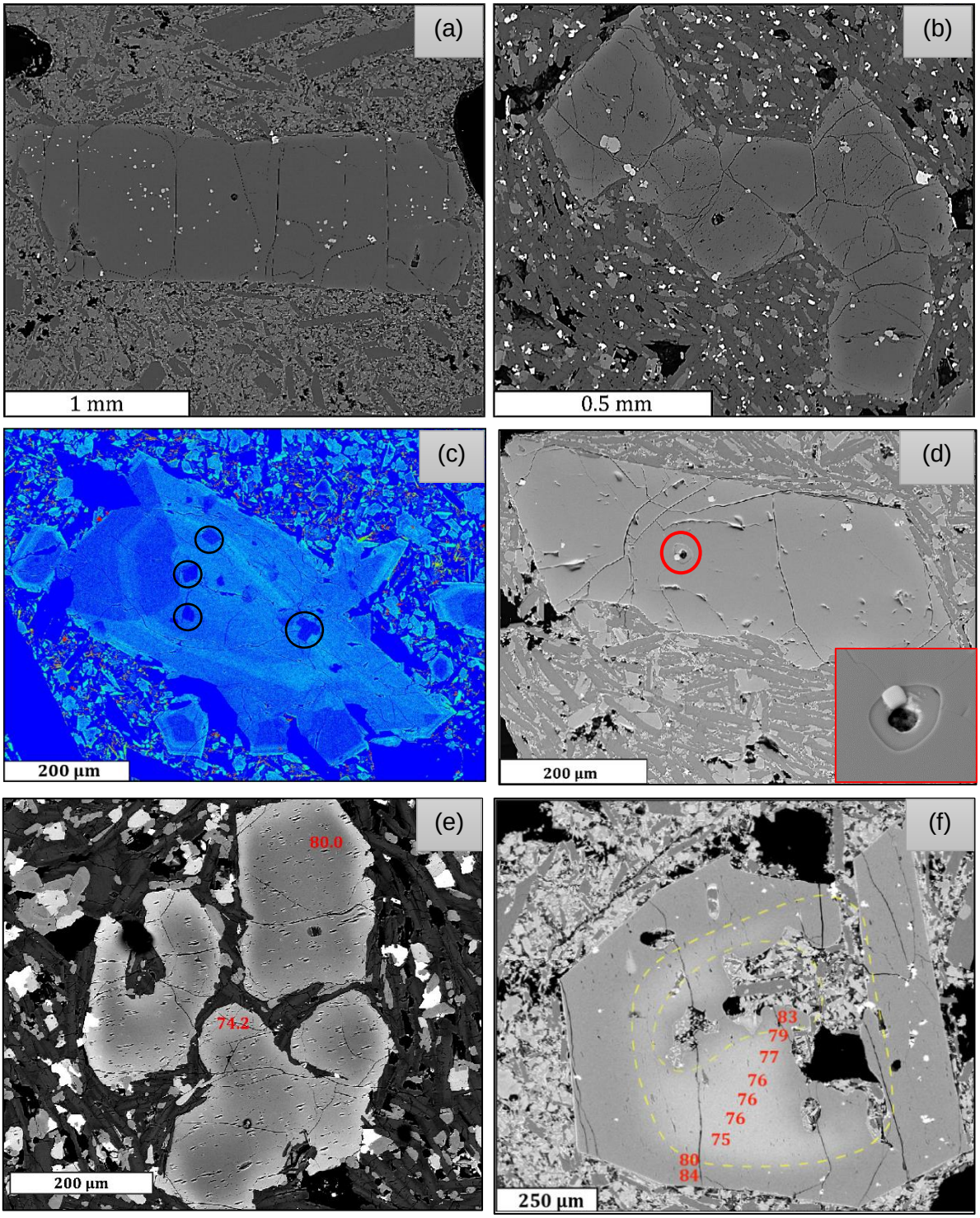

Fig. 8: BSE images taken by EMPA (a) Puyu9: Ol phenocryst with numerous spinel inclusions, distributed throughout the crystal. (b) Puyu3: aggregate of Ol crystals with large spinel inclusions. (c) Puyu9: Cpx microphenocrysts with sector (blue triangular zone) and/or oscillatory zoning: black circles: olivine inclusions. (d) Puyu18: pristine Ol phenocryst, with central melt inclusion. Red box: inclusion detail with trapped spinel crystal (e) Puyu3: Ol phenocryst with resorption and reverse zoning. Fo percentage in red (f) Puyu9: Ol phenocryst with resorption and reverse zoning. Fo percentage in red. Yellow zone marks the original crystal.

2.5.1.2 Plagioclase

Plagioclase (Pl) phenocrysts are scarce, with sizes distinctly smaller than olivine, being the largest in Puyu9, where they reache up to 0.8 mm. Generally, in all of the samples Pl varies from 0.1-0.4 mm in size and some microphenocrysts are found forming aggregates (**Fig. 9**). The composition at the core of Pl phenocrysts is relatively constant from An_{64} to An_{73} (**Fig. 7.b**).

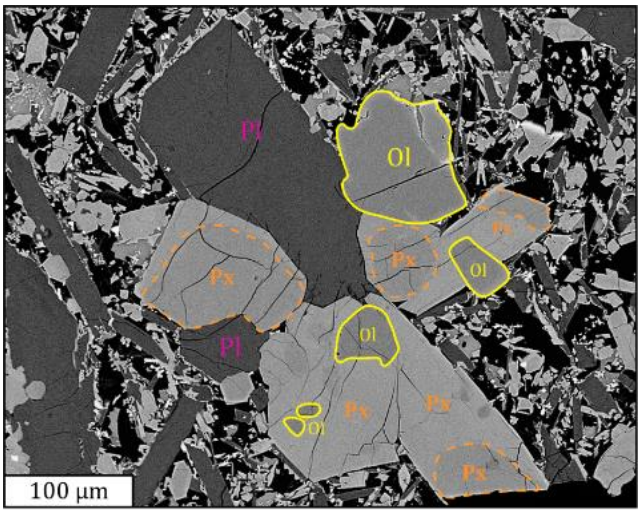

Fig. 9: BDE image by EMPA of sample Puyu9 (D14) showing glomerophyric texture.

Pl is mostly subhedral and display well-preserved edge and normal zoning, without disequilibrium features. Microlites are euhedral in shape and range from $An_{65\text{-}70}$, $Ab_{28\text{-}33}$. Puyu3, Puyu4, and Puyu18 lavas have glass-free matrices with abundant microlites commonly forming part of a trachytic or intergranular texture. MIs are scarce in this phase and are found only in Puyu 9, but in general, they are recrystallized and angled shaped.

2.5.1.3 Spinel

Spinel-group minerals (general formula: AB_2O_4) are important geological tools to understand the petrogenetic properties and geodynamic environment of the rocks in which they occur. Generally, $MgAl_2O_4$-rich spinel is considered the characteristic mineral of the uppermost lherzolite facies of the mantle. The spinels may be subdivided on the basis of the dominant A^{2+} (as Mg, Fe^{+2}, Zn, Mn) and B^{3+} (Al, Fe^{+3}, Cr, V) ions, the varieties being designated by the next most dominant constituent, picotite, which is conventionally used to describe Cr-bearing spinel and pleonaste for spinel containing some Fe^{2+}.

Spinel inclusions are abundant in Ol phenocrysts, and depending on the size of the host, we could observe up to ~30 inclusions in a single crystal, with size varying between 10 and 60 µm. Spinel also occur as isolated crystals in the groundmass, with the groundmass of Puyu 3 being the sample with greater amounts.

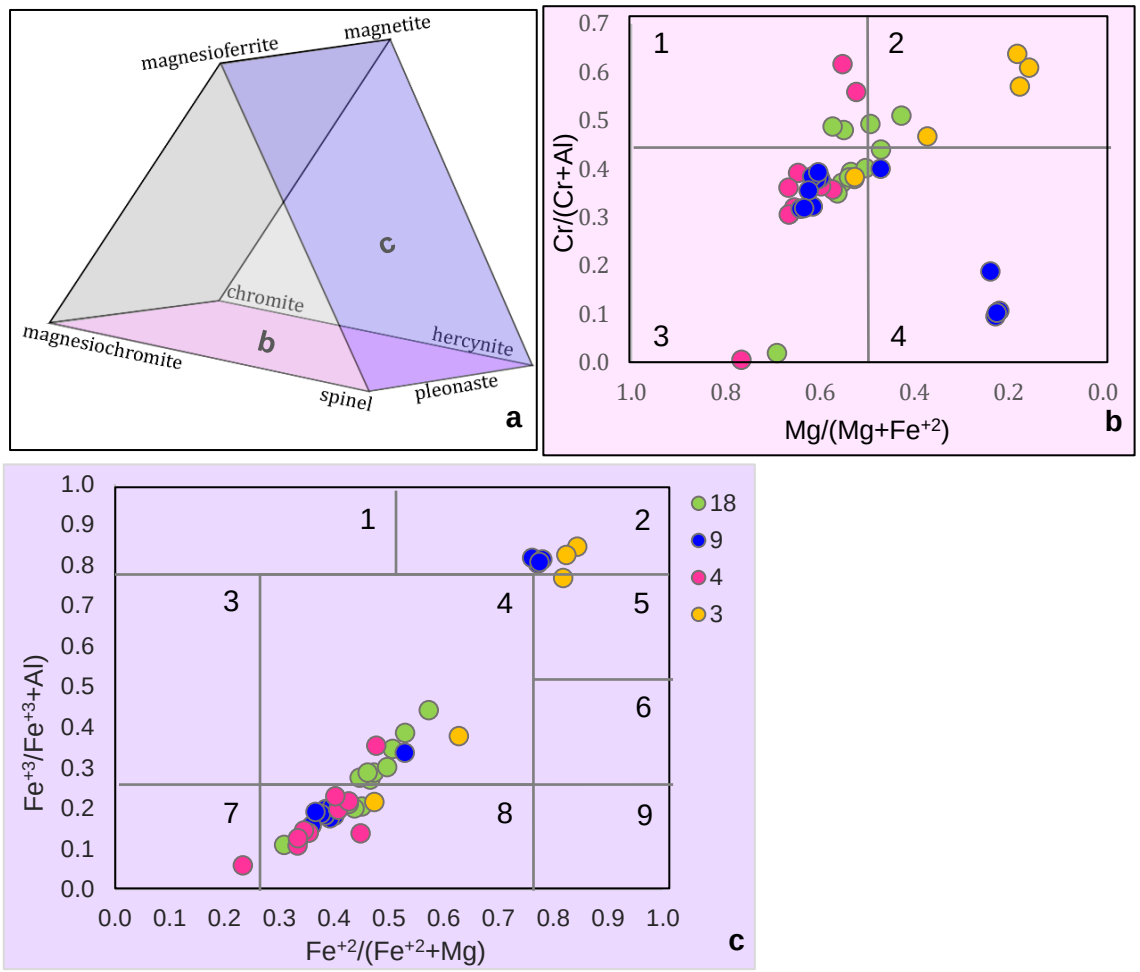

Fig. 10: (a) Spinel prism for the multi-component system: spinel (MgAl2O4) - hercynite (Fe Al2O4)-chromite (FeCr2O4) – magnesiochromite (MgCr2O4) – magnesioferrite (MgFe2O4) - magnetite FeFe2O4), after Deer et al.,1992.The projections of the basal face and the lateral-right face of the prism, represent the diagrams in “b” and “c” (b) Binary classification diagram considering the Cr-Al and Mg-Fe+2 exchange; 1=Magnesiochromite, 2=chromite, 3= spinel, 4= Hercynite. (c) Binary classification diagram considering the Fe+3-Al and Fe+2-Mg exchange; 1=magnesioferrite, 2= magnetite, 3= ferrian-spinel, 4= ferrian-pleonaste, 5=Al-magnetite, 6= ferrian-picotite, 7= spinel, 8= pleonaste, 9= Hercynite.

The composition of Ol-hosted spinels inclusions were obtained by EMPA and are plotted in (**Fig. 10**), using a simplified classification diagram of the main members of the spinel group. It can be seen that the trend in the composition is from pleonaste to ferrian pleonaste in which Fe^{+2} and Fe^{+3} increases with decreasing Mg and Al, with some more extreme compositions (magnetite) in the case of Puyu9 and Puyu3 (higher Cr#= 100 × Cr/[Cr+Al]). Their Cr# and Mg# range from 0.54 to 63.84 and from 15.60 to 76.62 respectively. Spinels also occurs frequently as trapped mineral in MIs, based on the inclusion/crystal volume ratio, suggesting that the magma was saturated in oxides.

2.5.2 Melt inclusion petrography

Several types of MIs were observed and were classified according to petrographic characteristics, although it was difficult to identify melt inclusion assemblages (MIAs, Cannatelli et al., 2016 and references therein) in Ol since most MI were randomly trapped in the crystals. Compositionally, we distinguished Type I MIs, which include inclusions that contained only homogeneous glass and MIs that contained one or more bubbles, and Type II MIs, which includes all recrystallized MIs with daughter and/or trapped crystals.

Both types are also classified by shape, which can be regular (oval or ellipsoidal) or irregular (from polygonal or negative crystal-shape to completely irregular). Recrystallized MIs were not re-homogenized, but analyzed directly by LA-ICPMS, and previously analyzed by SEM to document the mineral phase(s).

The vast majority of MIs hosted in phenocrysts from **Puyu3** were completely recrystallized (**Fig. 11.d**), with sizes ranging from 20 to 80 µm, and daughter crystals of clinopyroxene were observed. Some crystals contained MIs coexisting with fluid inclusions (FIs) where a rapidly moving vapor bubble was visible at room temperature, although the analysis of fluid inclusions is beyond the scope of this study.

In **Puyu4**, homogenous MIs have colorless to transparent light brown glass, sizes ranges from a few microns up to 100 µm (**Fig. 11.a**); the majority being between 15 to 20 µm), and V_{bubble}/V_{melt} is 3.9% in average. Recrystallized MIs are less abundant, and the majority of them contains only Ox crystals. In general, the shape of the MIs varies between oval and irregular, and sometimes coexist with FIs.

Homogenous MIs from **Puyu9** have colorless to pale brown glass (**Fig. 11.b**) and shapes varying from oval to completely irregular, sizes range from a few microns up to 40 µm, and V_{bubble}/V_{melt} is about 5.4%. Recrystallized MIs contain only Ox crystals or are completely recrystallized (**Fig. 11.e**), with the last ones displaying the biggest sizes, up to 75 µm.

In **Puyu18**, homogenous MIs have colorless to pale brown glass, sizes range from a few microns up to 60 µm, and V_{bubble}/V_{melt} is 5.2% on average. Recrystallized MIs containing daughter crystals are less abundant, although inclusions with Ox trapped crystals are found easily (**Fig. 11.c**), and reach sizes of 155 µm. Some crystals contain MIs along with FIs and some MIs are decrepitated (**Fig. 11.f**)

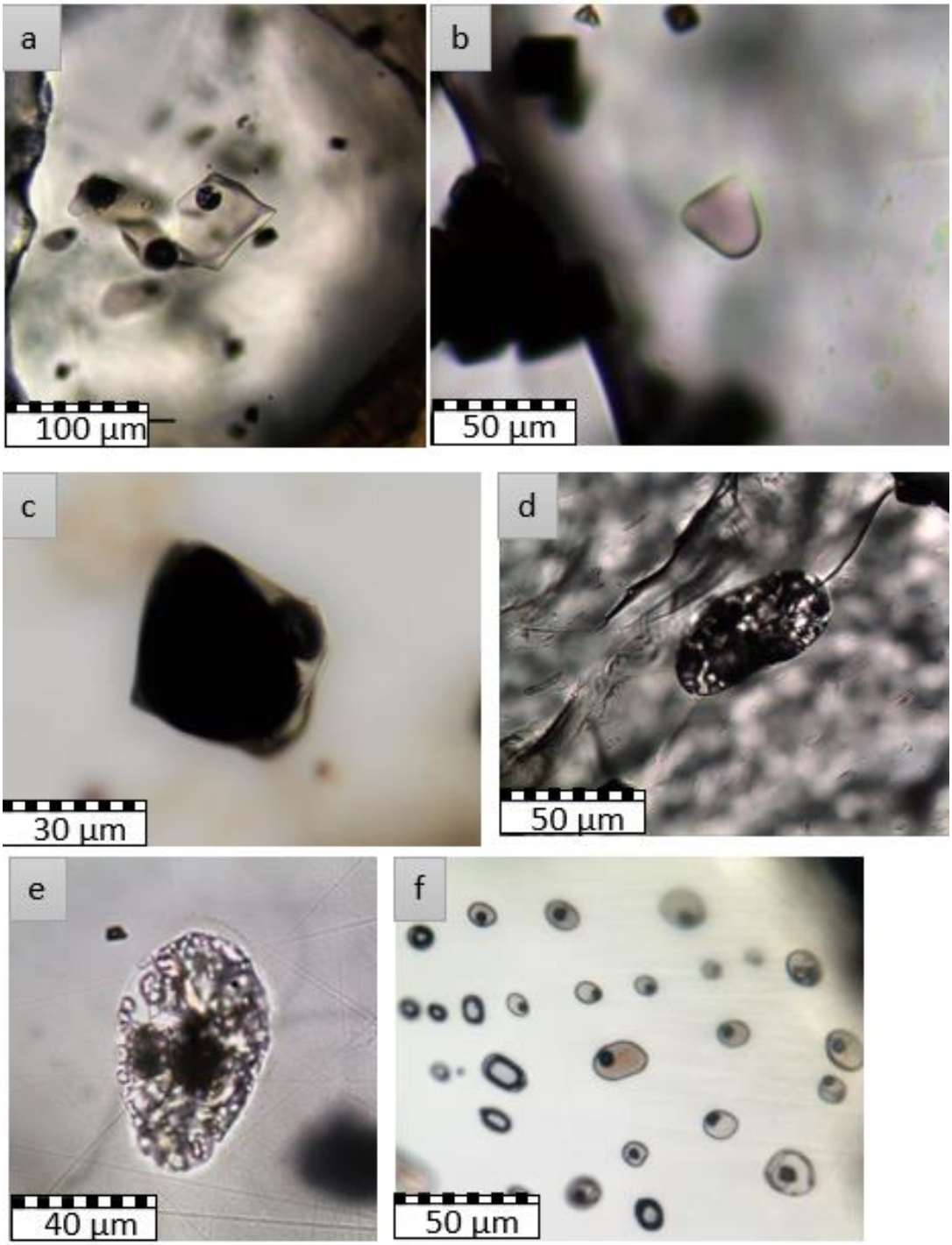

Fig. 11: thin section images taken by optic microscope. a) Puyu4: homogenous MI, b) Puyu9: homogenous MI, c) Puyu18: MI with a large trapped spinel crystal, d) Puyu3: recrystallized MI, e) Puyu9: recrystallized MI, f) Puyu18: melt inclusion assemblage together with FIs.

2.5.3 Melt inclusion post-entrapment modifications

In olivine, the crystallization of a wall around the inclusion that is more Mg-rich than the trapped MI, produces a compositional gradient that will deplete the trapped melt in Mg relative to Fe^{+2}, (Ford et al., 1983). The following crystallized olivine will be less Mg-rich, producing an area of Fe-

rich olivine surrounding the MI The ferrous iron in this olivine layer then diffuses into the surroundings (more Mg-rich host), resulting in Fe^{+2} loss from the trapped melt (Danyushevsky et al., 2000) and increases concentrations of ferric iron and olivine-incompatible elements. Corrections for PEC can be experimentally reversed by remelting these host wall and/or daughter phases; or by numerical corrections, by adding increasingly forsteritic olivine back into the MI until the olivine-liquid pair displays a Fe-Mg partition coefficient of K_D = 0.30±0.04.

Equilibrium conditions between olivine and MI were tested using the model of Roedder and Emslie (1970). The Fe –Mg exchange coefficient, K_D, calculated based on the composition of the MI and the adjacent host phase, suggests disequilibrium between the MI and its host. In order to correct for PEC, calculations were performed by using the software Petrolog (Danyushevsky and Plechov, 2011). The software allows the addition of minerals crystallized from the melt back to the melt composition, thus moving it up along a cotectic line (a liquid line of descent) towards more primitive compositions. The mineral with the lowest pseudo-liquidus temperature is added to the melt composition during the reverse of fractionation calculations.

Olivine was numerically added, in 1% crystallization increments, using the olivine – silicate melt model of Ford et al. (1983), and assuming a QFM+1.5 (quartz-fayalite-magnetite) buffer, calculated by the oxygen geobarometer model proposed by Ballhaus et al. (1991). In general, the selected host olivine crystals do not show a great compositional variety and the composition of the MI was modeled with the composition of the olivine in the area near the MI.

When using the MgO content of bulk rock analysis, the calculated olivine composition does not match the measured composition of the phenocrysts, indicating a possible early fractionation of a Mg-rich olivine.

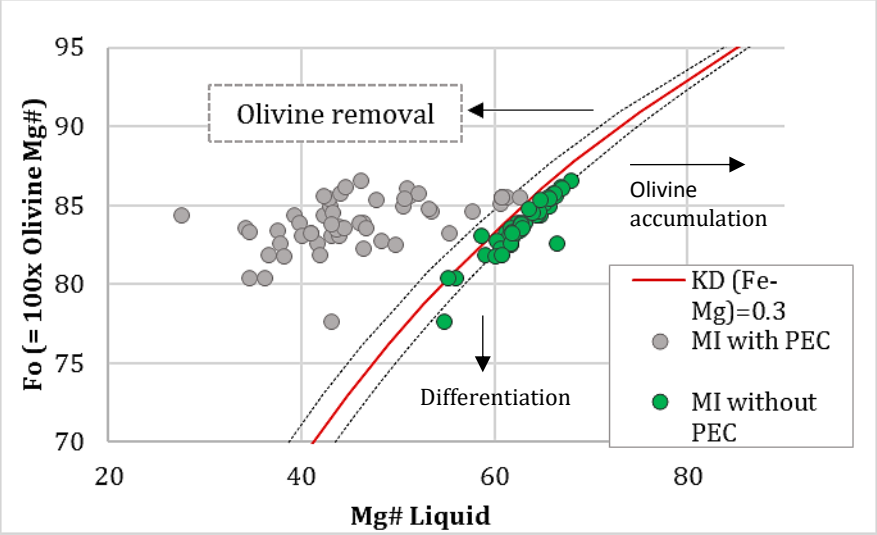

Fig. 12: Rhodes diagram. The solid line, within some established error bound, here given as K_D (Fe-Mg) ol-liq = 0.30±0.03.

We show in **Fig. 12** the plot of Mg number (#Mg= 100*Mg/ (Mg+Fe^{+2})) of MI versus the host Fo content, where the original measured MI compositions without correction (gray circles) are located in the Ol removal field expected by the crystallization of olivine in the inclusion-host interphase. The effect of adding olivine back to the composition of the inclusions (green circles) is displayed, locating the recalculated MI in the area of equilibrium with the host composition. The amount of olivine correction needed to achieve the goal ranged from 1.65 to 17.46 % (6.8% average), values that are expected for Ol-hosted MI from monogenetic lavas.

2.5.4 Melt inclusion and bulk rock compositions

In this section, we present MI and whole-rock compositions (Table 2), recalculated and uncorrected volatile-free MIs compositions (Table 3 and Appendix Table 8 respectively.

Table 2: Whole rock major element compositions (wt. %) of studied lava samples.

Sample	Puyu3	Puyu4	Puyu9	Puyu18
SiO_2	48.49	49.21	45.75	48.40
Al_2O_3	16.59	17.06	16.14	16.38
Fe_2O_3*	10.43	9.49	10.49	10.39
MgO	8.23	8.53	8.41	7.95
CaO	9.42	9.08	10.21	9.45
Na_2O	3.40	3.29	3.03	3.33
K_2O	1.30	1.30	1.70	1.26
TiO_2	1.66	1.31	2.04	1.67
P_2O_5	0.37	0.35	0.54	0.38
MnO	0.15	0.16	0.17	0.15
Cr_2O_3	0.04	0.05	0.04	0.04
LOI	-0.50	-0.20	1.00	0.20
Total	99.80	99.80	99.00	99.80

We analyzed a total of 120 MIs, and used 90 of them, which were considered further for data reduction. Thirty analyzed points were discarded because the oxides total was low (less than 95 wt %), or we observed that the system was open and a contamination of the host occurred. We considered MIs with a total oxide content ≥95% acceptable, although most data close around 98% (**Fig. 13**).

We analyzed homogeneous MIs (N=63) by electron microprobe, of these only 31 qualified for size to be analyzed by LAICPMS. Recrystallized MIs (N=27) were analyzed only by LAICPMS. For sample Puyu3, phenocryst phases only contained recrystallized inclusions, and therefore we did not obtain EMPA data for them.

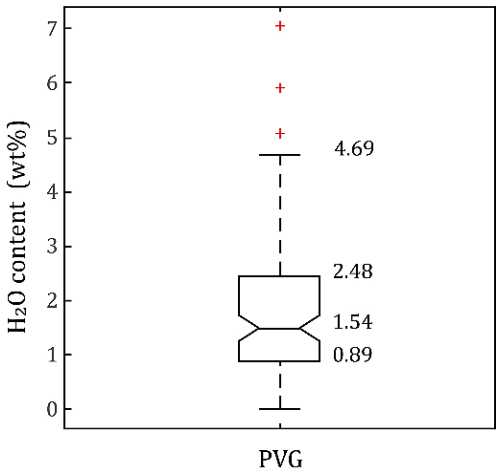

Fig. 13: Box plot of the grouping of water content data in the inclusions.

The low oxidation degree (Fe_2O_3/FeO<0.2) of Puyu 4 (0.22) and Puyu 9 (0.16) together with the low volatile content (LOI≤1); suggest that the samples are chemically representative of PVG's volcanic products. Samples Puyu 4 and Puyu 9 show whole rock Mg# of 68.05 and 64.51 respectively.

Table 3: recalculated type-I MI composition for Puyu4, 9, 18, measured by EMPA and type-II MI composition, measured by LAICMS (α) for Puyu3. Total =sum of all oxides plus Cl in original (uncorrected) electron microprobe analyses, %PEC= percentage post-entrapment olivine crystallization. Major element oxides reported are normalized to 100% on a volatile-free basis. H_2O= estimated by the difference method assuming all of the missing components in the analyses was H_2O. Shape= 1: ellipsoidal shape MIs, 2= irregular shape MIs, 1*= ellipsoidal shape on microlites.

Sample	**4-A14**	**4-A16**	**4-A34**	**4-B15**	**4-B16**	**4-B23**
Shape	1	1	1	2	1	1
SiO_2	50.538	49.966	49.763	50.072	49.67	49.218
TiO_2	1.48	1.456	1.644	1.444	1.572	1.525
Cr_2O_3	0.027	0	0.048	0	0	0.009
Al_2O_3	17.729	19.168	20.199	19.249	19.88	20.727
FeO*	8.575	7.827	6.77	7.007	7.09	6.589
MnO	0.117	0.146	0.124	0.102	0.084	0.074
MgO	6.25	5.635	4.524	5.857	4.762	4.819
CaO	9.943	10.253	10.983	10.476	10.68	11.03
Na_2O	3.6	3.748	4.104	3.887	4.212	4.003
K_2O	1.389	1.419	1.454	1.416	1.601	1.507
P_2O_5	0.352	0.382	0.39	0.49	0.449	0.499
H_2O	1.941	0.721	1.678	1.813	1.833	0.914
Total	98.059	99.279	98.322	98.187	98.167	99.086
% PEC	11.56	9.62	7.01	9.42	8.4	8.07
#Mg	64.838	64.469	62.914	67.957	63.174	64.914
Sample	**4-D31**	**4-D41**	**4-01-d**	**4-02-d**	**4-03-d**	**4-04-d**
Shape	2	2	2	2	2	2
SiO_2	50.06	49.76	49.9	50.16	50.15	50.1
TiO_2	1.56	1.53	1.43	1.31	1.5	1.43

Cr_2O_3	0.04	0	0.04	0.04	0.03	0.03
Al_2O_3	20.62	20.19	18.88	18.6	18.69	18.34
FeO*	5.99	6.53	7.76	7.69	7.63	8.01
MnO	0.08	0.13	0.11	0.11	0.1	0.06
MgO	4.6	5.18	5.69	5.75	5.71	6
CaO	10.69	10.51	10.04	9.94	9.95	9.78
Na_2O	4.36	4.12	4.35	4.6	4.51	4.45
K_2O	1.5	1.56	1.32	1.32	1.32	1.38
P_2O_5	0.52	0.48	0.48	0.47	0.42	0.42
H_2O	2.78	1.55	1.94	1.93	1.94	1.96
Total	97.22	98.45	98.06	98.07	98.06	98.04
% PEC	7.45	8.49	2.81	3.08	2.75	3.18
#Mg	66.12	66.94	65.2	65.81	65.79	65.84
Sample	**4-12-k**	**4-13-j**	**4-14-h**	**9-A21-a**	**9-A4-a**	**9-A4-b**
Shape	1	2	2	1	2	1
SiO_2	48.84	50.04	50.73	48.09	47.13	52.03
TiO_2	1.4	1.54	1.47	2.45	2.61	2.32
Cr_2O_3	0.06	0.03	0.03	0	0	0
Al_2O_3	18.4	19.8	19.69	18.62	15.93	19.94
FeO*	8.48	6.45	7.05	7.58	10.83	4.84
MnO	0.16	0.13	0.09	0.1	0.21	0.09
MgO	6.77	4.95	5.29	4.97	4.83	3.5
CaO	10.08	10.91	9.15	11.62	8.88	10.2
Na_2O	4.06	4.29	4.52	3.83	4.85	4.26
K2O	1.28	1.47	1.55	2.19	3.87	2.21
P_2O_5	0.5	0.41	0.43	0.55	0.84	0.6
H_2O	2.75	2.37	2.96	1.84	0.91	1.34
Total	97.25	97.63	97.04	98.16	99.09	98.66
% PEC	8.89	5.97	1.65	7.95	8.17	4.44
#Mg	67.08	66.3	65.53	64	56.07	65.66
Sample	**9-B42**	**9-C32**	**9-C46-23**	**9-C46-24**	**9-D12-43**	**9-D32**
Shape	2	1	1	1	2	2
SiO_2	47.32	46.84	47.88	48.21	47.58	47.86
TiO_2	2.57	2.25	2.57	2.39	2.31	2.85
Cr_2O_3	0.05	0.07	0	0	0	0
Al_2O_3	19.36	18.71	18.99	18.54	20.3	18.67
FeO*	6.64	8.29	7.16	7.03	6.65	6.95
MnO	0.11	0.1	0.12	0.12	0.06	0.13
MgO	4.18	4.93	4.3	4.06	4.53	4.26
CaO	11.61	11.91	12.42	12.36	11.26	12.05
Na_2O	4.48	3.8	3.74	4.26	4.27	4.12
K_2O	2.75	2.38	2.1	2.35	2.31	2.29
P_2O_5	0.94	0.74	0.72	0.68	0.74	0.82
H_2O	2.4	1.98	1.87	1.89	2.81	2.35
Total	97.6	98.02	98.13	98.11	97.19	97.65
% PEC	3.96	7.59	6.64	5.97	6.11	5.88
#Mg	63.59	61.84	61.95	61.6	64.78	62.77
Sample	**18-A34-28**	**18-B37-68**	**18-B38**	**18-B41-43**	**18-B41-45**	**18-B42**
Shape	2	1	1	1	1	1

SiO_2	53.13	48.72	49.01	49.91	50.36	50.04
TiO_2	2.99	1.83	2.08	2.15	2.17	2.23
Cr_2O_3	0.06	0.01	0	0	0.01	0.03
Al_2O_3	16.06	19.23	19.02	19.62	19.78	19.49
FeO*	7.6	8.42	8.12	6.66	6.15	6.88
MnO	0.11	0.08	0.13	0.1	0.07	0.08
MgO	3.39	4.8	5	4.17	3.84	4.36
CaO	10.15	11.32	10.38	10.49	10.58	10.35
Na_2O	4.74	4	3.55	4.43	4.53	4.42
K_2O	1.14	1.38	1.76	1.63	1.72	1.64
P_2O_5	0.63	0.23	0.95	0.83	0.78	0.49
H_2O	1.8	2.57	1.36	1.21	1.46	1.07
Total	98.2	97.44	98.64	98.79	98.54	98.93
% PEC	4.06	8.41	8.19	6.41	5.71	6.83
#Mg	54.79	60.16	61.75	62.55	62.54	62.79
Sample	**9-C37-15**	**9-C37-18**	**9-C38-14**	**18-A11**	**18-A13**	**18-B11-93**
Shape	*1	*1	*1	*1	*1	*1
SiO_2	49.04	48.66	50.26	51.53	53.18	52.76
TiO_2	2.47	2.55	2.88	2.32	2.83	2.82
Cr_2O_3	0	0	0	0.02	0.01	0
Al_2O_3	16.97	15.99	17.17	16.71	16.45	16.23
FeO*	9.06	9.62	8.04	8.88	7.19	7.46
MnO	0.12	0.05	0.19	0.09	0.1	0.07
MgO	4.87	5.27	4.21	4.14	3.4	3.6
CaO	8.9	10.71	6.52	11.02	9.85	10.18
Na_2O	4.66	4.15	4.6	2.56	4.2	4.08
K_2O	2.97	2.46	5.1	2.16	2.13	2.15
P_2O_5	0.95	0.55	1.04	0.57	0.67	0.66
H_2O	0.91	0.91	0.93	0.92	0.94	0.93
Total	99.09	99.09	99.07	99.08	99.06	99.07
% PEC	8.35	9.53	7.48	8.99	5.8	7.56
#Mg	53.29	53.89	52.77	49.13	49.84	50.41
Sample	**4-B25**	**4-B31**	**4-B34**	**4-B41**	**4-C31**	**4-11-I**
Shape	1	1	1	2	2	1
SiO_2	50.023	47.645	49.931	49.594	49.594	49.9
TiO_2	1.341	1.499	1.537	1.492	1.571	1.41
Cr_2O_3	0.046	0	0	0.037	0	0.03
Al_2O_3	17.568	17.419	19.969	19.926	19.477	18.83
FeO*	8.974	10.597	7.003	6.995	7.179	7.68
MnO	0.138	0.082	0.147	0.064	0.12	0.1
MgO	6.793	7.562	4.619	5.308	5.456	5.73
CaO	9.836	9.801	10.726	10.571	10.436	10.02
Na_2O	3.655	3.583	4.143	4.088	4.086	4.54
K_2O	1.267	1.342	1.501	1.464	1.59	1.33
P_2O_5	0.358	0.469	0.424	0.46	0.49	0.42
H_2O	0.907	1.056	0.91	1.18	1.811	1.96
Total	99.093	98.944	99.09	98.82	98.189	98.04
% PEC	8.94	17.46	8.73	9.02	9.34	2.7
#Mg	65.71	64.426	62.636	65.837	65.972	65.72

Sample	**4-05-d**	**4-07-i**	**4-08-a**	**4-09-a**	**9-B31-81**	**9-B31-79**
Shape	2	2	2	2	1	2
SiO_2	50.02	48.83	49.19	48.84	46.18	49.59
TiO_2	1.4	1.43	1.41	1.41	2.46	2.43
Cr_2O_3	0.01	0	0.02	0.02	0	0
Al_2O_3	18.18	16.22	18.65	19.48	19.32	18.55
FeO*	8.09	10.31	8.25	8.3	8.13	6.91
MnO	0.18	0.21	0.12	0.11	0.14	0.18
MgO	6.06	7.91	5.61	6.04	4.79	3.44
CaO	9.83	9.16	10.01	10.27	11.59	8.13
Na_2O	4.47	4.03	4.72	3.7	4.1	5.7
K_2O	1.38	1.5	1.61	1.44	2.5	4.1
P_2O_5	0.39	0.38	0.42	0.38	0.79	0.96
H_2O	1.94	1.34	2.42	2.87	2.74	0.95
Total	98.06	98.66	97.59	97.13	97.26	99.05
% PEC	3.28	10.22	3.52	6.21	9.29	5.13
#Mg	65.86	66.43	63.89	64.68	61.69	58.67
Sample	**9-A43**	**9-A45-107**	**9-B31-77**	**18-A24-9**	**18-A32**	**18-D24-114**
Shape	2	1	2	2	2	*1
SiO_2	45.95	46.16	49.66	48.44	52.03	58.28
TiO_2	2.39	2.4	2.51	2.04	2.14	2.18
Cr_2O_3	0.01	0.06	0	0.05	0	0.01
Al_2O_3	19.19	19.42	18.25	19.34	15.9	18.32
FeO*	8.3	8.02	7.17	8.71	8.56	4.7
MnO	0.13	0.14	0.14	0.1	0.06	0.08
MgO	5.02	4.63	3.1	6.09	5.3	1.45
CaO	11.83	11.82	8.5	9.28	9.27	2.56
Na_2O	3.98	4.1	5.44	4.34	2.38	5.28
K2O	2.44	2.48	4.1	1.04	3.38	6.12
P_2O_5	0.76	0.77	1.13	0.57	0.97	1.01
H_2O	2.8	1.85	1.78	1.06	1.79	1.96
Total	97.2	98.15	98.22	98.94	98.21	98.04
% PEC	6.63	7.41	5.31	11.37	9.96	1.7
#Mg	62.32	61.24	55.2	59.13	62.77	39.39
Sample	**18-A21**	**18-A24-7**	**18-A24-8**	**18-D22-116**	**18-D22-118**	**4-C26**
Shape	1	2	1	2	2	*1
SiO_2	50.36	48.73	49.15	49.89	52.97	53.93
TiO_2	2.31	1.83	2.03	2.17	2.28	2.22
Cr_2O_3	0	0.02	0.04	0.06	0	0
Al_2O_3	20.98	19.01	19.6	18.61	19.9	17.34
FeO*	5.95	8.74	8.43	7.24	5.01	5.39
MnO	0.07	0.14	0.1	0.1	0.12	0.09
MgO	3.3	5.21	4.79	4.58	3.07	2.49
CaO	9.42	10.85	9.75	10.84	9.44	8.27
Na_2O	5.07	3.86	4.61	4.15	4.7	5.65
K_2O	1.86	1.11	1.04	1.63	1.92	4.02
P_2O_5	0.67	0.5	0.46	0.74	0.59	0.58
H_2O	1.41	1.13	0.94	1.12	1.86	1.91
Total	98.59	98.87	99.06	98.88	98.14	98.09

% PEC	3.59	5.82	6.08	6.34	2.03	4.76
#Mg	60.28	61.71	60.59	62.92	61.84	49.98
Sample	**18-C11**	**18-C22**	**18-B43**	**3-C7$^{\alpha}$**	**3-C13$^{\alpha}$**	
Shape	1	1	*1	3	3	
SiO_2	49.01	49.59	53.87	48.08	46.63	
TiO_2	1.98	2.07	3.05	2.51	2.16	
Cr_2O_3	0.01	0.00	0.04	0.00	0.04	
Al_2O_3	18.88	19.05	16.1	12.10	13.05	
FeO*	8.55	7.6	6.64	9.51	9.49	
MnO	0.13	0.07	0.15	0.06	0.10	
MgO	5.06	4.65	2.79	9.65	8.68	
CaO	10.87	10.36	9.91	11.64	13.66	
Na_2O	3.44	4.29	4.28	2.47	2.42	
K_2O	1.56	1.73	2.41	1.69	1.23	
P_2O_5	0.51	0.59	0.76	0.43	0.48	
H_2O	0.92	1.28	0.95	1.7	1.92	
Total	99.08	98.72	99.05	98.3	98.08	
% PEC	8.15	7.73	4.82	12.05	0.4	
#Mg	60.81	62.07	47.05	68.25	66.04	

According to the TAS diagram (**Fig. 14**), 54 analyzed type-I MIs normalized 100% water-free can be classified as basanite and trachybasalt andesite (46.0 - 53.1 wt.% SiO2, 4.9-9.8 wt% alkali), with the majority falling in the trachybasalt field following an alkaline affinity.

The Composition of MIs from Puyu 4 and Puyu 18 follow a similar positive slope, while MIs from Puyu9 display similar amount of silica but higher contents of alkali, following a different chemical evolution. Groundmass glasses have higher alkalis (9.5-12.4 wt. %) and higher SiO_2 (47.3-61.5 wt. %) than MIs, suggesting that extensive crystallization occurred after melt inclusion entrapment. Bulk rocks in general contain less silica and alkali than MIs (**Fig. 14.b**), and are located on the most primitive extreme of the evolution trend. The greater difference between MIs and bulk rock composition can be observed in Puyu 9.

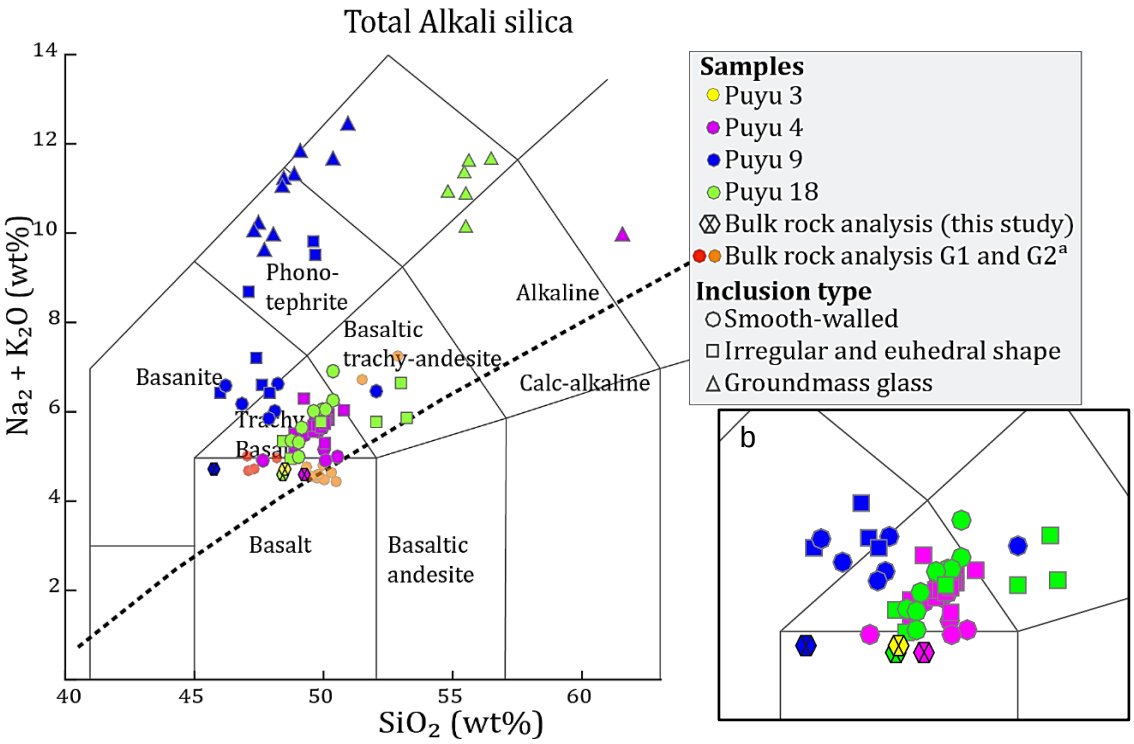

Fig. 14: TAS (Total alkalis v/s silica Le Bas et al., 1986) classification diagram. Dotted curve divides the alkaline and sub-alkaline fields (Irvine and Baragar, 1971).a) Bulk rock analysis from Gonzalez-Ferran et al. (1994). (b) Detail of the trachy basalt field.

According to the location of MEC, and considering the distinction in groups of cones made by Gonzalez-Ferran et al. (1994), Puyu 9, which belongs to the northern alignment, has a similar chemistry as Group 1 (but with less silica), while Puyu 3, 4 and 18, belonging to the southern lineament, show similarities with Group 2 (straddling more between the alkaline and calc-alkaline fields). In terms of silica, MIs have a greater range of variability than bulk rock, reflecting their trapping throughout the magmatic evolution.

Data from non-recalculated MIs show much lower MgO content than the bulk rock (1.05 - 4.71 wt. % and 7.95 - 8.53 wt.% respectively), which may indicate an important Ol crystallization at the host-inclusion interface, or a change in the magmatic conditions not reflected in the analyzed inclusions.

Concentrations of MgO in PEC corrected MIs range from 3.07 to 7.91 wt. %, showing an increase of 177.5% and #Mg of PEC-corrected MI range from 54.8 to 68. Despite this increase of MgO in MIs achieved by PEC correction, those contents are still lower than bulk rock ones, which could indicate a certain evolution in the composition of magma during the eruption of the monogenetic cones.

The grouping of MIs by shape is not very noticeable and most irregular inclusions have a composition similar to those with an oval shape.

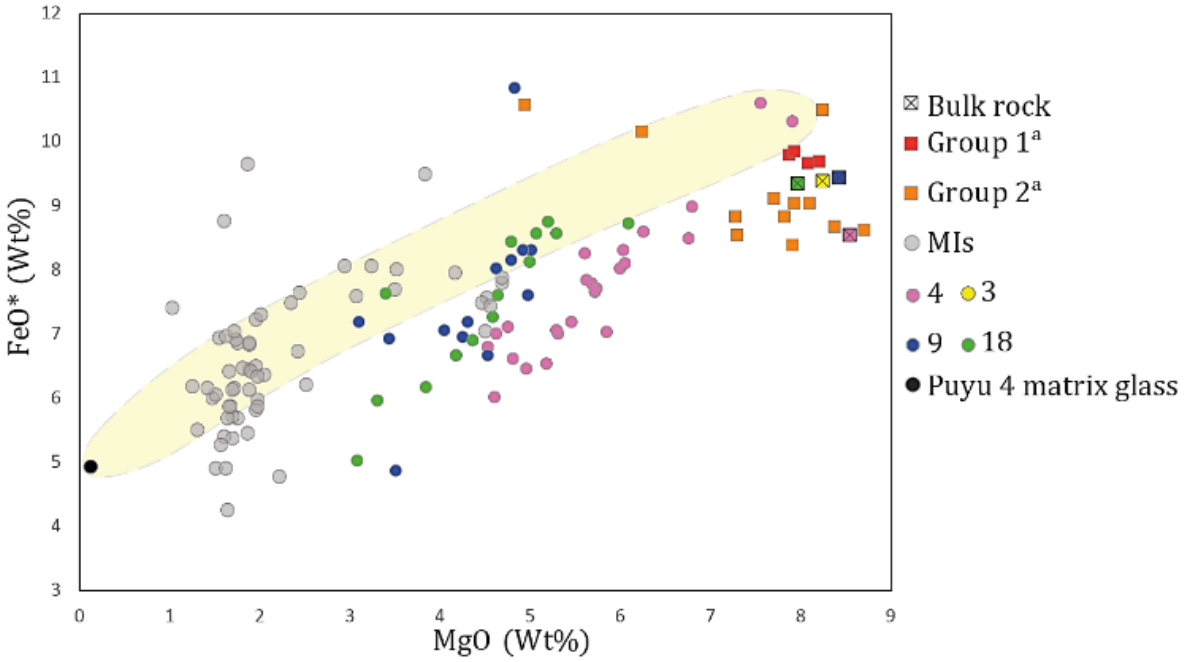

Fig. 15: Harker diagram of MgO v/s total FeO (calculated as FeO*=FeO+Fe_2O_3/1.11). a) Bulk rock analysis from Gonzalez-Ferran et al. (1994). *MIs: corresponds to data of MI without recalculation.* 4-9-18: correspond to the inclusions of each MEC modeled according to the host Fo %. The yellow area represents the compositional track from primitive MI and to groundmass glass.

In **Fig. 15**, we plotted bulk rock analysis from Gonzalez-Ferran et al. (1994) and we can observe that the distinction in north and south lineaments groups determined by the authors is not clear in terms of the bulk rock Fe content of our samples. Defining an evolution path from Puyu 4 MIs with higher FeO and MgO content to the groundmass glass composition (yellow field, Fig. 15), most MIs fall in the area of most differentiated composition, and although PEC corrected MIs display a similar slope, the majority falls below this area, suggesting a possible loss of FeO in inclusions. Data from Puyu 18 and 9 show some overlapping, and Puyu 4 MIs display higher MgO contents.

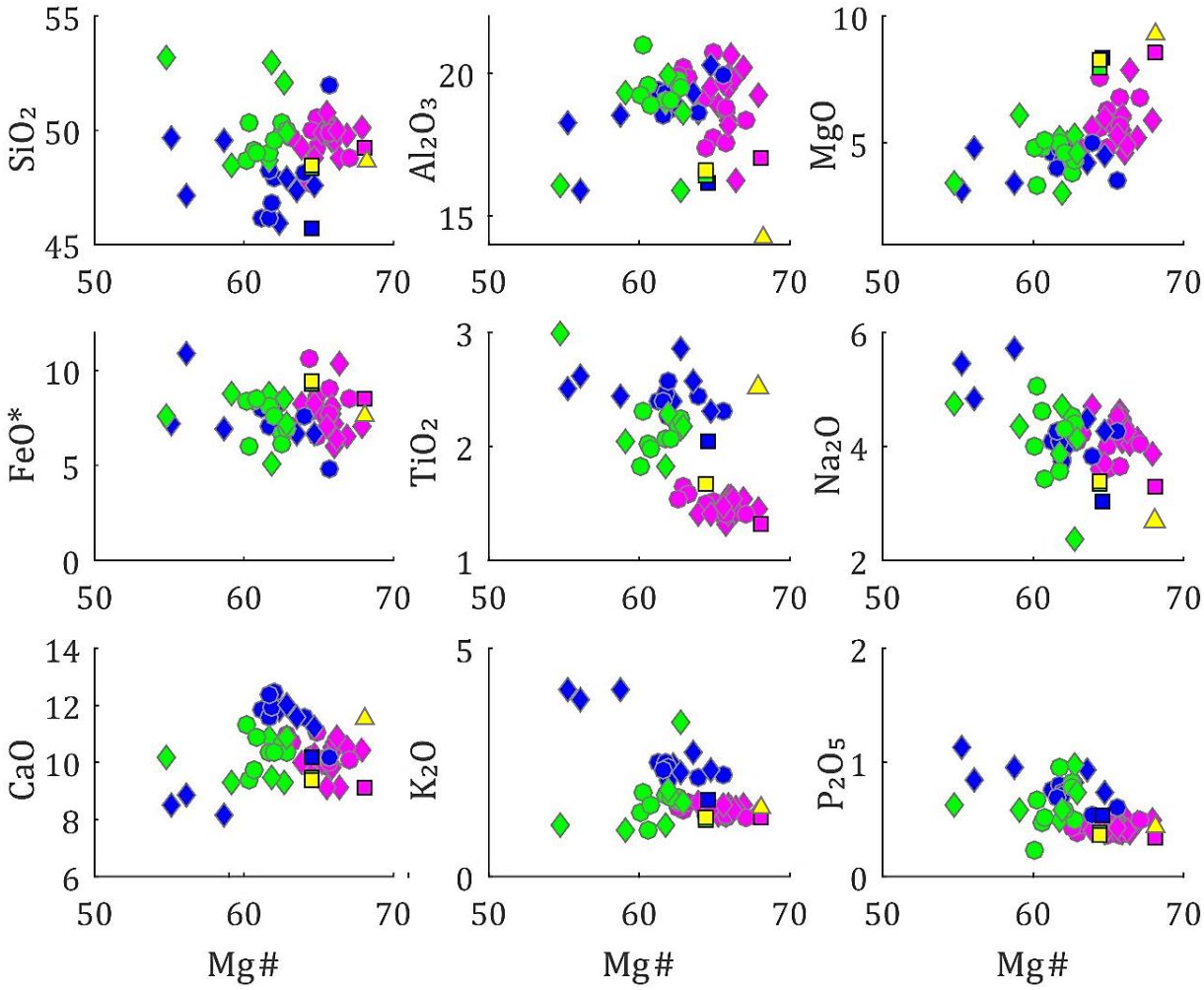

Fig. 16: Harker diagrams of major elements variation (wt. %) versus Mg#, Circles= oval shaped MI. Diamonds= irregular MI. Triangle= recrystallized MI. Square= Bulk rock data. Yellow= Puyu3, Green=Puyu18, Blue=Puyu9, Magenta= Puyu4.

To better visualize the trend of MI according to the crystallization path, we plotted major elements vs Mg# (**Fig. 16**). Puyu 4, in addition of containing Ol with the highest forsterite content, also contains MI with the highest Mg# values. The Al_2O_3 content follows a negative slope, from the bulk rock composition, with the aluminum content, higher in inclusions. In the MgO content a trend of differentiation of MIs can be observed, with the amount in Puyu 9 and Puyu 18 being very close, with respect to the FeO* content, in which the MIs follow a slight positive slope, i.e. the less the amount of #Mg the greater the amount of FeO*. In the SiO_2 diagram, we can observe clear groups of MIs according to each MEC, and although the #Mg in Puyu18 and Puyu9 is similar, Puyu9 is more silica unsaturated.

Puyu9 shows a particular composition, besides having a lower silica content; it has the highest levels of TiO_2, CaO and K_2O, a characteristic that is repeated in the bulk rock data.

Calcium and sodium values tend to increase as #Mg decreases, which occurs because the formation of plagioclase is late in the crystallization of magma, appearing more towards the end, forming part of the groundmass.

We can observe that MIs showing extreme values correspond to MIs of irregular shape. In these cases the crystallization of the host in the wall of the inclusion could be of greater proportion and would have modified in a more important way the composition of the MIs. Oval shaped MIs of Puyu 4 and the recrystallized MIs from Puyu 3 would be the most similar to the bulk rock composition.

2.5.5 Trace elements

Puyuhuapi magmas have elevated incompatible elements (i.e., LILE, HFSE and REE) relative to other SVZ calc-alkaline rocks (Hickey-Vargas et al., 2016; López-Escobar & Moreno, 1994) In general, the incompatible trace element concentrations increase with increasing SiO_2 content for each sample, but in general, Puyu 9 has a higher incompatible content and a lower silica content. Samples display similar primitive mantle-normalized patterns (**Fig. 17)**, with high LREE/HREE ratios, spider diagrams follow a typical trend for alkali magmas; they show enrichment in highly incompatible trace elements (Cs, Ba, Rb and Th). It is repeated as positive Pb and K anomaly and as a negative Nb anomaly, although to a lesser extent in Puyu 9. A slight negative Eu anomaly can be observed that may have been in equilibrium with a plagioclase-bearing mantle source. The relatively low concentrations of heavy REE suggests the presence of residual garnet in the source. Ca rich clinopyroxene, generally have $D < 1$, with values for the light REE being slightly lower than for the heavier REE, which may lead to light REE enrichment in the melt (Wilson, 1997).

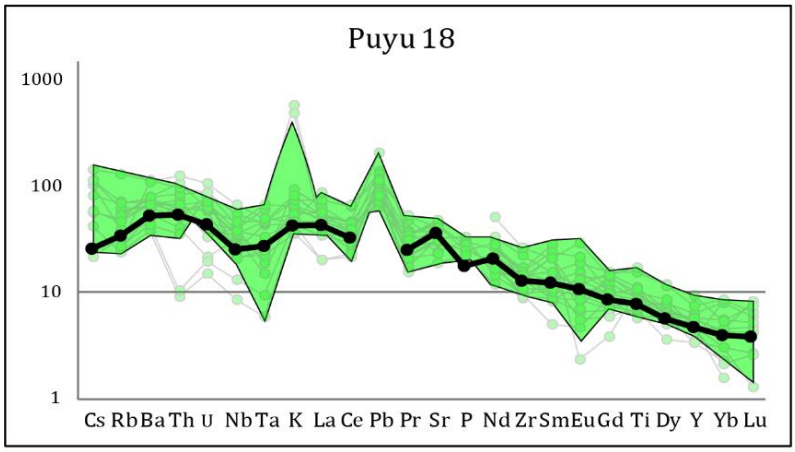

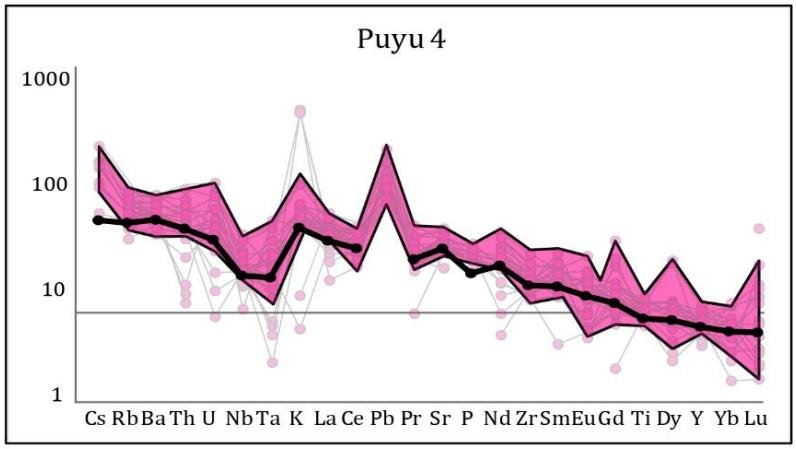

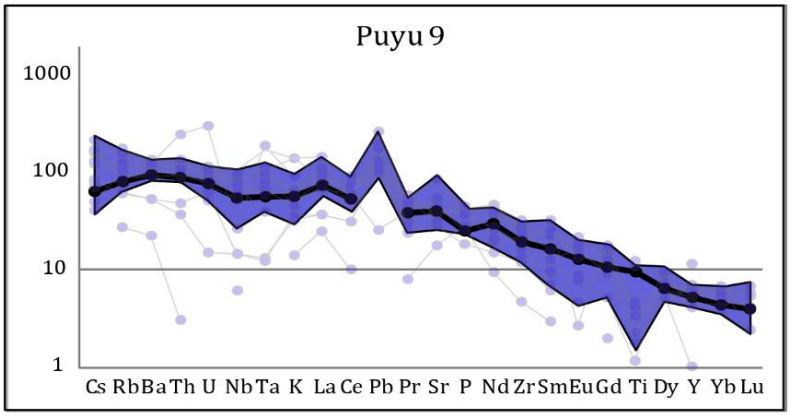

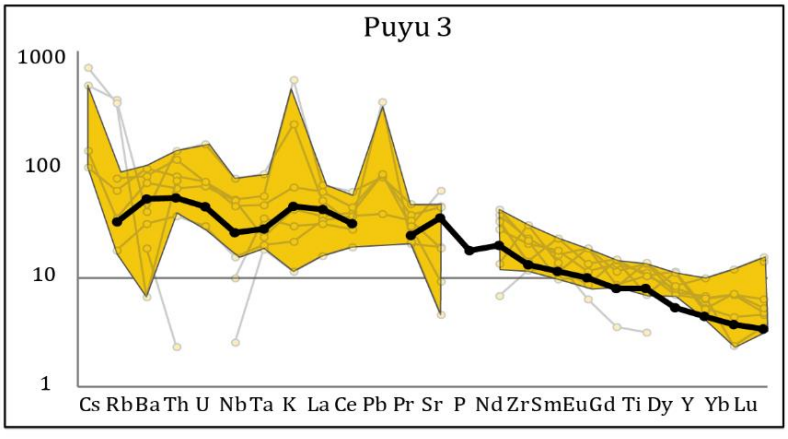

REE pattern of bulk rock composition

Fig. 17: Primitive mantle normalized trace elements patterns for each sample; normalization factors were taken from Sun and McDonough (1989).

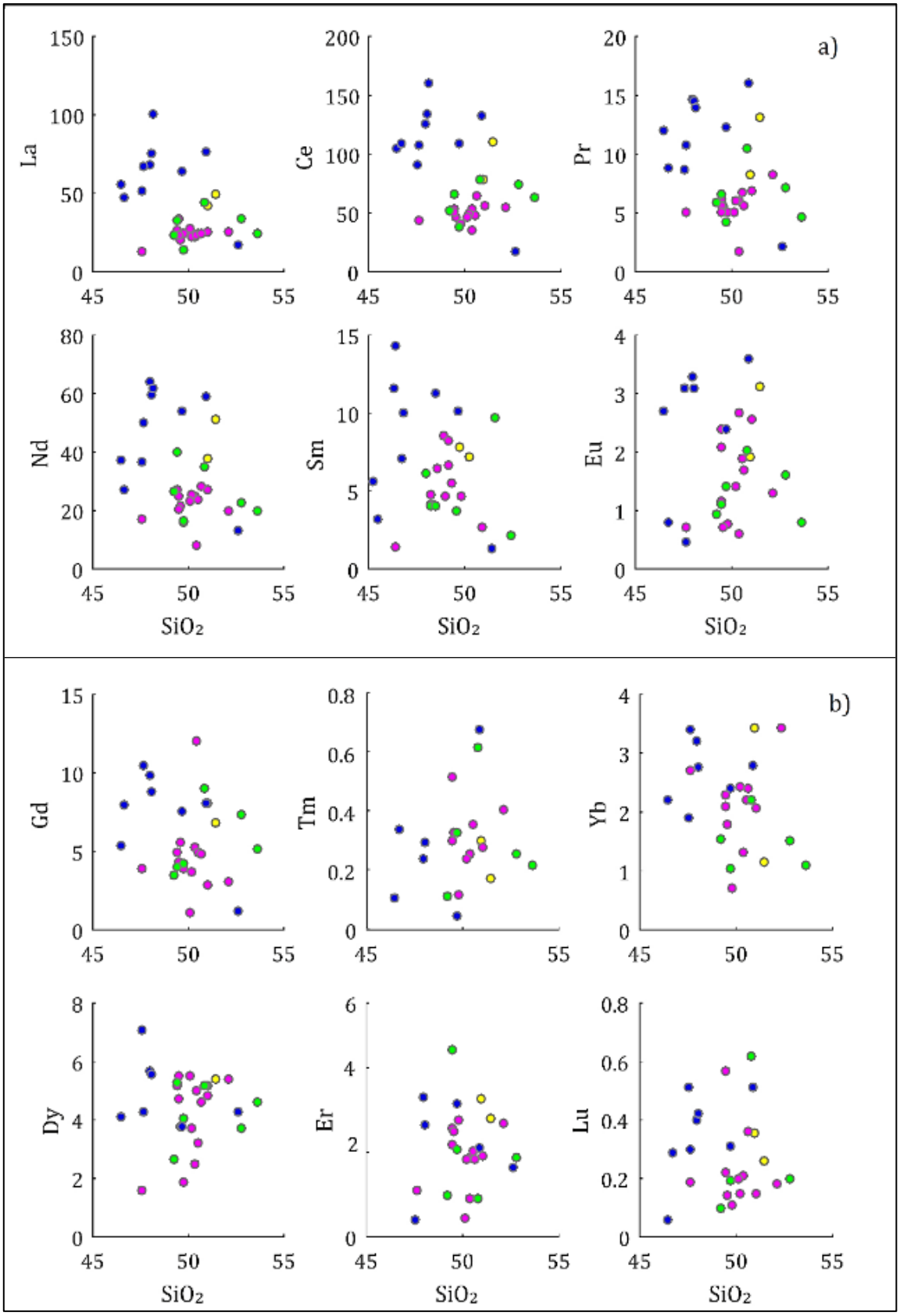

Fig. 18: REE content on melt inclusion, measured by LAICPMS. (a) LREE (ppm) versus SiO_2 wt. %, (b) HREE (ppm) versus SiO_2 wt. %.

Considering the variation of REE in contrast to the amount of silica (**Fig. 18**) the sample suit as a whole and within units display trends with SiO_2. Puyu 9 has a higher content of LREE, and the points show a positive slope when increasing SiO_2, although the samples Puyu 4 and Puyu 18 have a higher content of SiO_2, they are less enriched in LREE. A positive trend is also observed with the increase in silica.

Although we measured a limited amount of MIs in Puyu 3, their composition is similar to the Puyu9 MI. As for the HREE, the data are less clearly grouped, although the distinction between cone Puyu 9 and cones Puyu 3, Puyu 4 and Puyu 18 is observable.

#Mg values close to 70, Cr between 500 and 600 ppm and Ni between 250 and 300 ppm indicate that the magma is primitive (Wilson, 1989). Our data show #Mg values close to 70, but Cr and Ni indicate that the magma has undergone some fractionation of olivine. This first crystallization event occurred that in the magma chamber would have retained part of the Ni and Cr (**Fig. 19**), although it can also indicate that the magma does not come from a normal mantle but from a metasomatized source region.

A clear difference between the composition of MIs and bulk rock analysis can be observed, although in general the values of Cr do not exceed 350 ppm, i.e. below the threshold of a primitive magma. Among the MIs data, Puyu 4 MIs are grouped in the upper range while Puyu9 and 18 show some split of the data. The Cr and Ni could be lower in the inclusions since they are compatible with olivine and there could be diffusion within the host crystal.

Puyu 9 and Puyu 3 MIs contain high values of incompatible elements. Zr has a very similar content between inclusions and the bulk rock, being an immobile element in fluids of subduction zones. The amount of Zr in Puyu 4 and Puyu 18 does not vary according to the amount of MgO, while Puyu 9 shows the greatest variability. Values from 100 to 200 ppm of Zr are common in other MEC from the SVZ (e. g. Caburgua, Huelemolle, Huililco, La Barda, McGee et al., 2017), but Puyu 9 almost double these values.

Something similar happens with the distribution of strontium. Sr, which behaves like a mobile element in slab-fluxing processes related to subduction, increases a lot in inclusions with respect to the bulk rock content. Puyu 4 and Puyu 18 MIs contain amounts of those elements that do not exceed 200 ppm, the minimum value represented for most of the Puyu 9 MIs. For both elements, Puyu 3 MIs show a more chemical affinity with the Puyu 9 MIs. Differences between samples suggest a difference in the magmatic source.

The greater accumulation of these elements in Puyu 9 and Puyu 3 could be due to the longer interaction time of MIs with their hosts (olivine) before the eruption. The incompatible nature of these elements with olivine makes the melt enriched. The long residence time of magmas from

Puyu 3 and Puyu 9 is assessed by petrographic observations, as many of the Puyu 9 MIs and great part of the Puyu 3 MI are recrystallized, indicating a relatively slow cooling process.

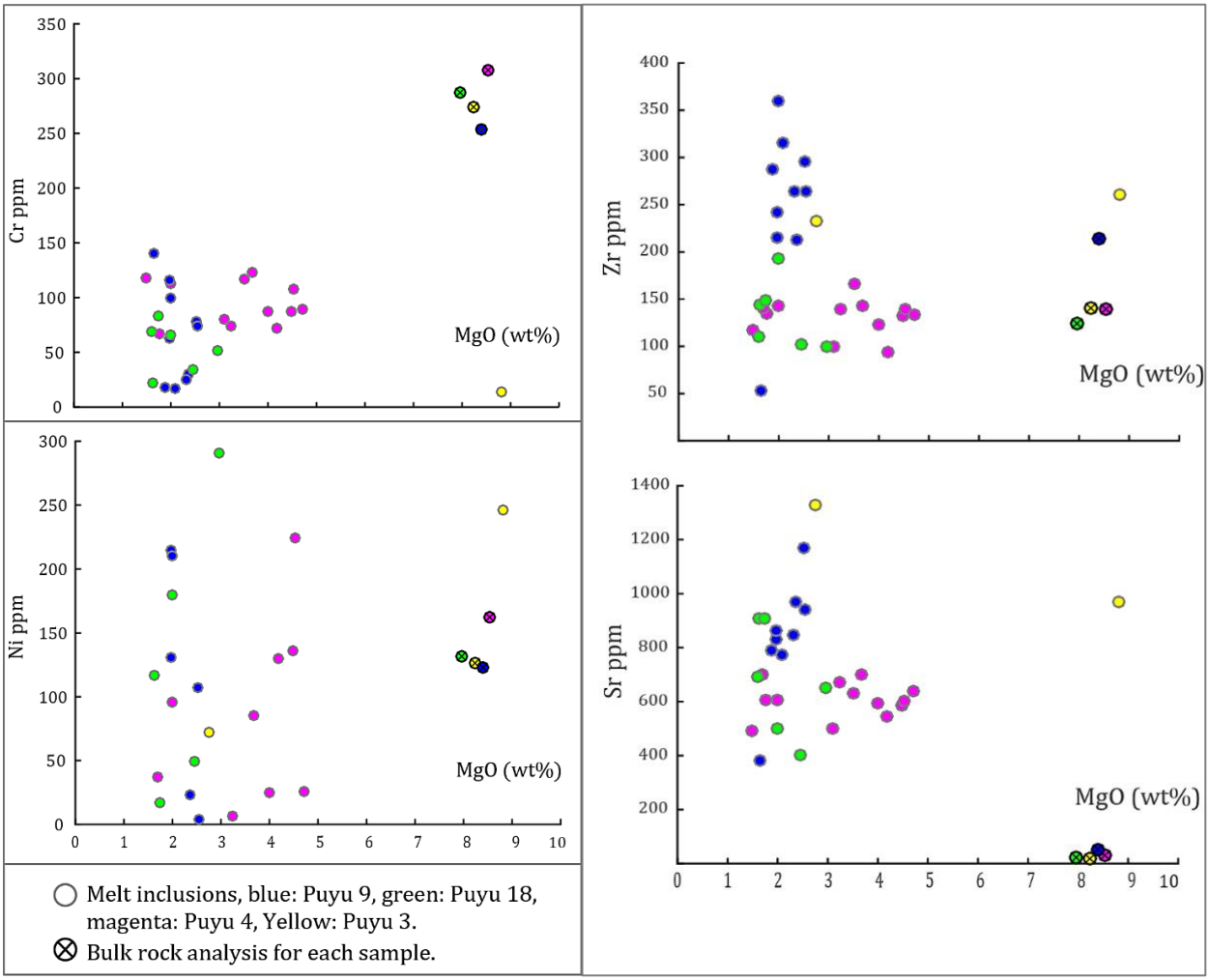

Fig. 19: trace elements versus MgO content.

Trace elements like Ni, Ca and Cr in olivine show large variations in concentration, mainly controlled by equilibration temperatures of the olivines, these elements are grouped according to the each MEC and they are either main components or strongly concentrated in co-existing mantle minerals (Cr in garnet and Ca in Cpx).

Ni content tends to be slightly higher in spinel-facies than in garnet-facies olivines with the same Fo content . In typical mantle peridotite, olivine hosts ca. 90% of all Ni, and is the only element besides MgO and Co that has higher concentrations in Ol than primitive mantle and therefore must be compatible during mantle melting (De Hoog et al., 2010)

Ni contents range from 42.4 to 2895 ppm (1253 ppm avg.), and concentrations decrease with lower Fo, creating a high slope (**Fig. 20**).

The highest Ni levels were measured at the center of Ol and the lowets at the rim of Puyu9 and Puyu18, Puyu3 displays a a continuous decrease, between rim and center points.

Chrome contents range from 1.37 to 1050 ppm (238.9 ppm avg.) discarding data out of range. There is no clear difference between points analyzed at the center of the crystals and those at the edge. In Puyu9 and Puyu18, we can distinguish two families of data showing an increase of Cr in more fayalitic rims.

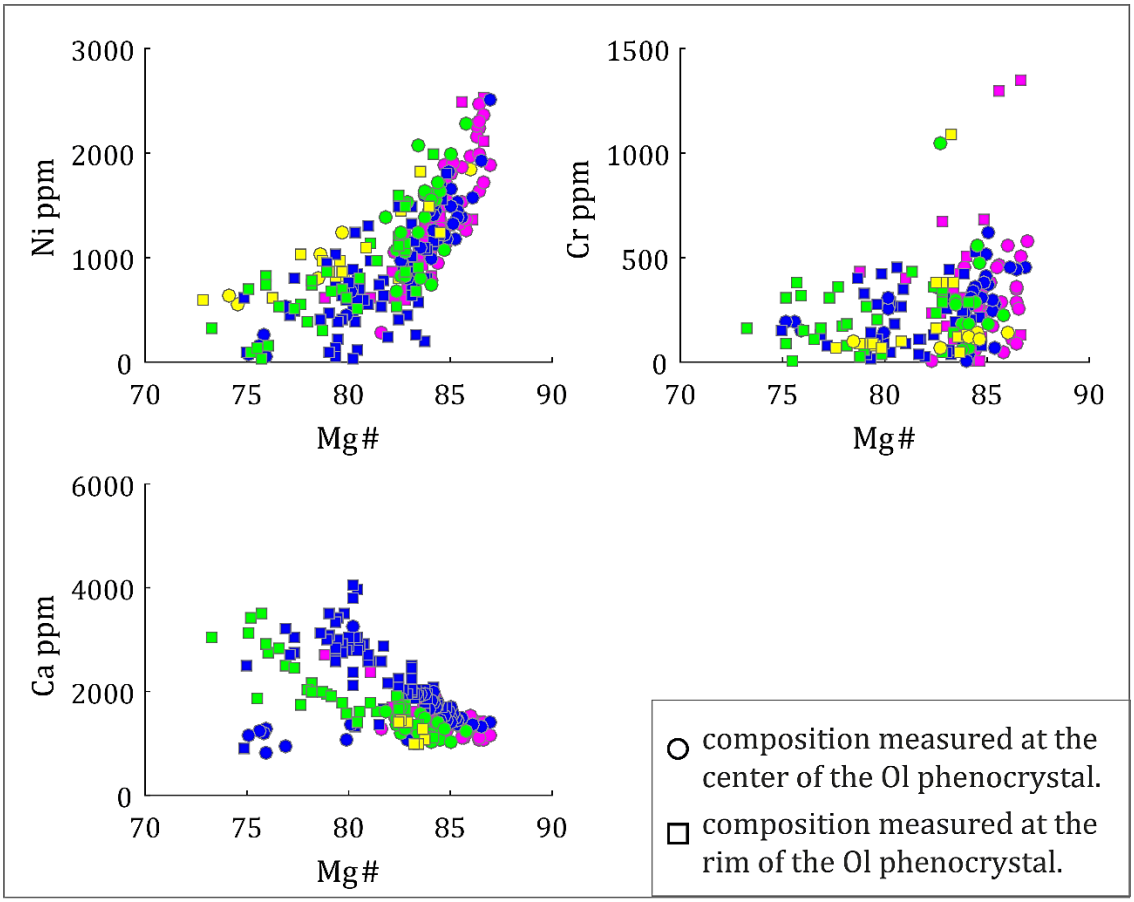

Fig. 20: Trace elemennts contents on Ol phenocrysts. Measured by Electro micro-probe analizer.

Calcium values range from 809.8 to 4044 ppm (1854.1 ppm avg) and are the opposite of what is expected, as the amounts of calcium at the rim are greater than those measured at the cores. Puyu9 has the highest levels, as in the MIs. In Puyu 4 olivines followig this trend are also observed but limited to the Mg#, suggesting that the magma had a shorter residence time in the crust, and the growth of the crystals was limited by the triggering of the eruption.

2.5.6 Raman CO_2 densities

Fifty bubbles were analyzed by Raman spectroscopy, of which 23 have detectable CO_2 (i.e., a Fermi diad is present in the Raman spectrum). Thirteen from Puyu 4, four from Puyu 18 and six

from Puyu 9. First, the percentage of volume occupied by the bubbles with respect to each MI was measured to determine the range in which there is a linear relationship between MI and bubble volume. This procedure is applied to get a range in which MIs contain the same volume proportion as vapor, suggesting that MIs trapped only melt and that the bubbles were generated in the MIs after trapping (Moore et al., 2015).

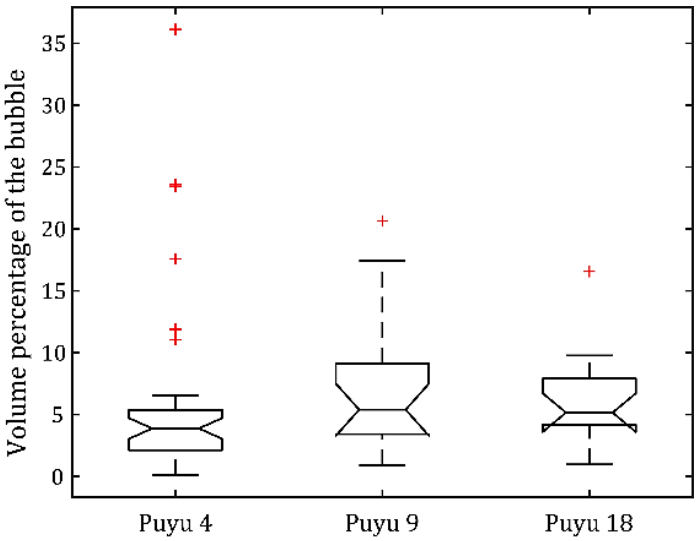

Fig. 21: Boxplot diagrams for bubble volume/ MI volume percentage.

Fig. 21 shows the volume percentage data distribution for each MEC. The outlier data were discarded, since these phenocrysts may have trapped a mixture of melt and vapor, and the proportion of those volatiles would not represent those that were originally dissolved in the magma. It is possible to notice that the values are similar for the different cones, with Puyu 9 being the one with slightly higher values.

To reconstruct the original dissolved CO_2 concentrations of the melt inclusions at the time of trapping, the amount of CO_2 in the melt inclusion glass and the bubble must be known. Calculated CO_2 densities are converted to mass using the melt inclusion volume that is occupied by the vapor bubble. In this case, the CO_2 content of the glass is not known. If we assume that the glass contains 0 ppm CO_2, a minimum CO_2 content for the MI can be determined by adding the CO_2 in the bubble into the glass, using the relative volume proportions of bubble and glass determined previously and the magma density.

In several previous studies (e.g. Moore et al., 2015; Shaw et al., 2008; Wallace et al., 2015) bubbles typically contain 40 to 90% of the total CO_2 in the MI. The reconstructed CO_2 content based on some finite amount of CO_2 in the glass is equal to the CO_2 content estimated by assuming that the glass contains no CO_2, plus the finite amount of CO_2 that is assumed for the glass because of the simplifying assumption that the mass of the bubble is negligible compared to the mass of the glass.

If we consider that, the glass has a standard amount of CO_2 of 500 ppm, then the total value of CO_2 contained in the magma range from 998 to 6903 ppm and the percentages of CO_2 retained in the bubble range from 47.6 to 92.7% (79% avg.) Another way to obtain the amount of CO_2 in the magma is to consider two possible scenarios, one in which most of the CO_2 (90%) was retained by the bubble and another in which only half of the CO_2 (50%) was retained. Considering the CO_2 values found in the bubbles and that the amount of water determined by the difference method is rather low (many data are close to 1%), the most likely scenario is that volatiles are concentrated in the bubbles. On Table 4, we show values for both scenarios and the corresponding calculated trap pressure. Calculated pressures range from 1.5 to 6.4 Kbar; this implies that olivine crystallization took place over a range of pressures, and by using a nominal gradient of 3.65 km/Kbar, the maximum depth of entrapment of the inclusions is 23 Km.

Degassing processes in basaltic magmas can be modeled using the solubilities of the end member system based on measured CO_2 and H_2O concentration of volcanic glasses can be used to determine the total pressure at which a basaltic liquid would be vapor saturated and the composition (i.e. CO_2/H_2O ratio) of vapor coexisting with such liquid at equilibrium (Dixon & Stolper, 1995). Pressures were calculated using VolatileCalc (Newman and Lowenstern 2002).

MEC	Inclusion	Mass of CO_2 in glass* (ppm)	Mass of CO_2 total* (ppm)	P* (Kbar)	Depth* (km)	Mass of CO_2 in glass** (ppm)	Mass of CO_2 total** (ppm)	P** (Kbar)	Depth** (km)
4	Puyu4-b	498	996	2.4	9	55	553	1.6	6
4	Puyu4-c-1	2306	4612	7.6	28	256	2562	4.9	18
4	Puyu4-c-2	1375	2751	5.2	19	153	1528	3.3	12
4	Puyu4-e	2947	5893	8.9	33	327	3274	5.9	22
4	Puyu4-f-3	4374	8748	7.6	28	486	4860	5.1	19
4	Puyu4-a-1	1731	3463	4.7	17	192	1924	3.1	11
4	Puyu4-l-1	2629	5257	7.8	29	292	2921	5.1	19
4	Puyu4-l-2	3155	6309	8.8	32	351	3505	5.9	21
4	Puyu4-l-3	1005	2011	3.9	14	112	1117	2.5	9
4	Puyu4-k	1086	2172	3.2	12	121	1207	2.0	7
4	Puyu4-i-1	3348	6696	9.0	33	372	3720	5.9	22
4	Puyu4-i-2	2105	4209	6.5	24	234	2338	4.2	15
18	C7-1	454	908	2.2	8	50	505	1.5	5
18	C2	3567	7134	8.9	32	396	3963	5.9	22
18	C8-1	2025	4050	6.9	25	225	2250	4.5	16
18	C8-2	1750	3501	6.2	23	194	1945	4.0	15
9	B31	2629	5258	8.3	30	292	2921	5.1	19
9	C11	4222	8444	8.9	32	469	4691	5.9	22
9	C34	2765	5530	6.6	24	307	3072	4.3	16
9	C41	1386	2772	4.0	15	154	1540	2.5	9
9	D33	3988	7975	9.6	35	443	4431	6.4	23
9	C43-1	6403	-	-	-	711	7115	5.2	19

Table 4: Reconstructed CO_2 concentrations of MI and calculated trapping pressures. ** Calculated pressures considering that the bubble retains 50% of the CO_2, ** Calculated pressures considering that the bubble retains 90% of the CO_2. In both cases, pressures were calculated using VolatileCalc (Newman and Lowenstern 2002). Depths were calculated using a nominal gradient of 3.65 km/Kbar.

2.5.7 Volatiles

We do not observe a clear pattern when CO_2 content of MIs is plotted against the Fo content of the host (**Fig. 22**) When comparing chlorine levels with host forsteritic content (**Fig. 24**), we can observe that Puyu 9 and Puyu 4 have a relatively more degassed magma. The chemistry of microlite hosted MIs, shows a slight increase in chlorine content, suggesting that the predominant effect is magma crystallization and although the entrapment of glass in more Fe-rich microlites is late, no important degassing is observed.

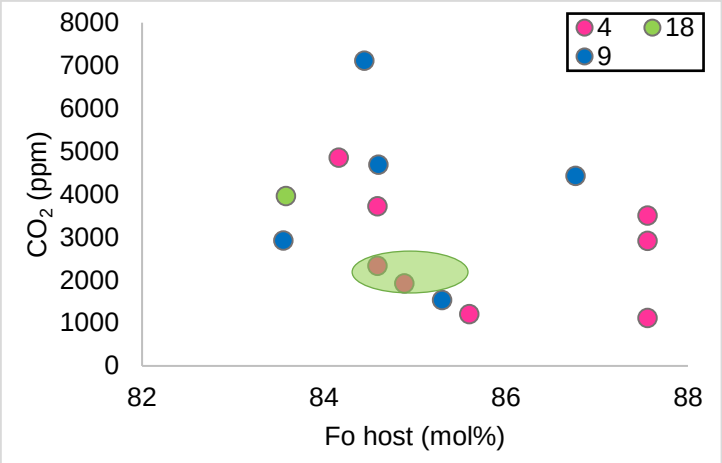

Fig. 22: model restored CO_2 content in relation with the forsterite content of the olivine host.

From **Fig. 23** it can be seen that the volatile content was slightly modified by PEC, being more visible in Puyu9. In spite of this and giving a range of reliability for the water content of the inclusions, it is possible to approximate the system as a closed degassing system in which the loss of CO_2 would be more important than the loss of water.

As for the water content (**Fig. 25**) we observe a similar trend, Puyu 4 and 9 have a similar volatile content, with water contents decreasing successively, until the composition of the groundmass glass, although chlorine levels on Puyu 18 increase, up to 0.7 wt. %.

Plots of the chlorine content versus K_2O content (**Fig. 26**) show that there is a clear grouping of data, where Puyu 9, as noted before has higher levels of K_2O, along with the groundmass composition of Puyu 18, which increases its K_2O content, in a linear relationship with chlorine.

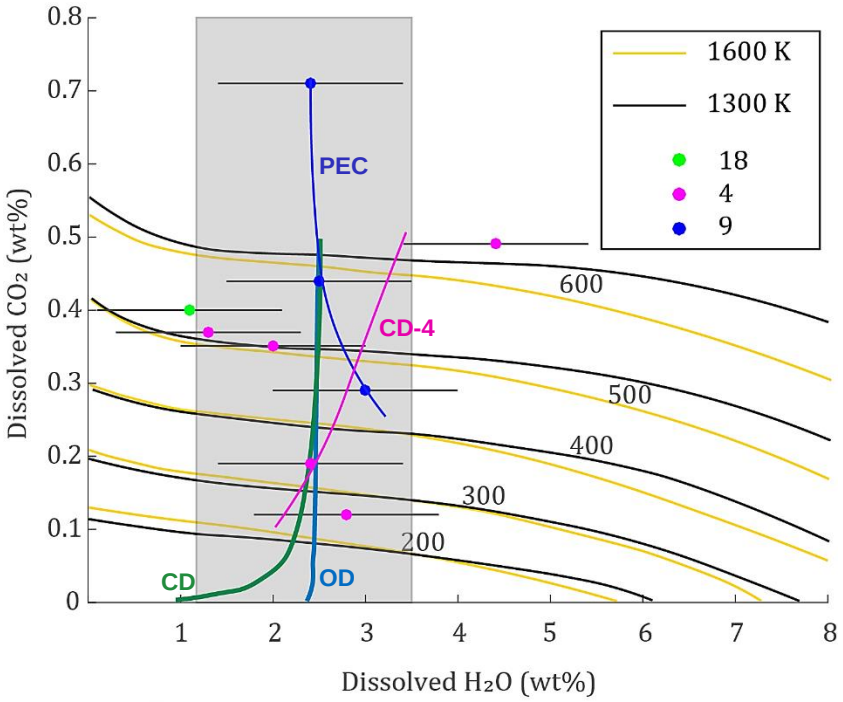

Fig. 23: H_2O versus CO_2 content in melt inclusions. OD: open degassing system, CD: closed degassing system; both curves calculated with VolatileCalc using a starting composition of 2.5wt.% H_2O, 5000 ppm CO_2, 48 wt.% SiO_2 and T of 13002°C. CD-4: a possible degassing path for Puyu4. Calculated equilibrium isobaric H_2O–CO_2 dissolved pairs in liquids basaltic compositions, each at two different temperatures. Numbers are pressure in MPa. Curves obtained from Papale et al., 2006. Error bars: H_2O of standard deviation of 1wt. %. Grey area represents the most reliable water content.

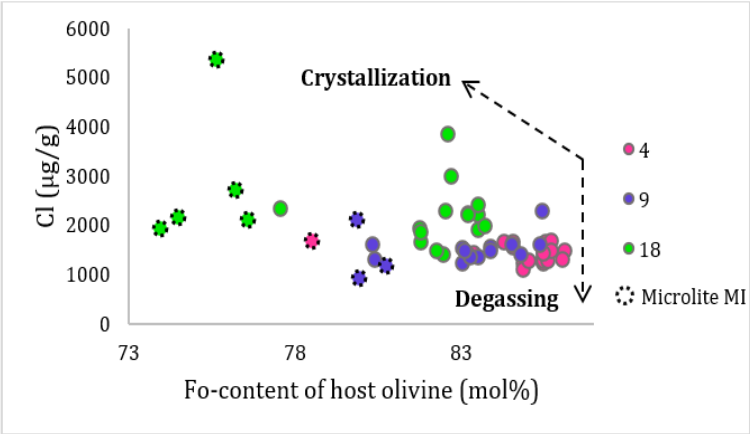

Fig. 24: melt inclusion chlorine content in relation to the Fo content of their host olivines.

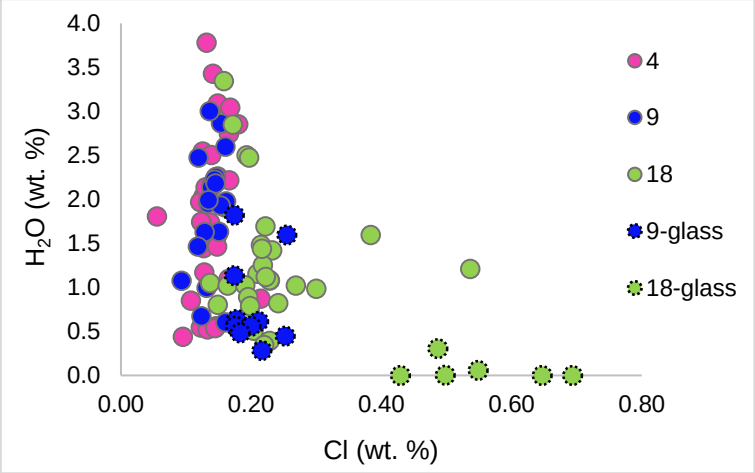

Fig. 25: Melt inclusion (4, 9, and 18) and matrix glass (Puyu 9 and Puyu 18) Cl concentration in comparison with the H_2O content.

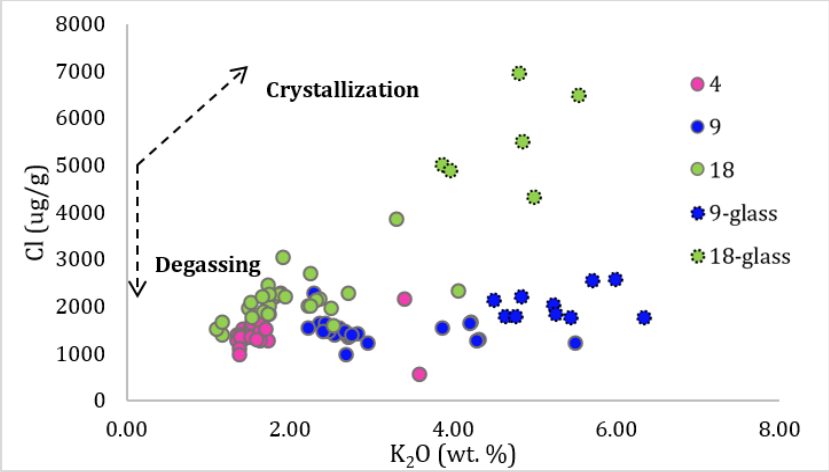

Fig. 26: chlorine versus K_2O melt inclusion content.

2.6 Discussion

In the following discussion, we integrate the whole rock and melt inclusion data with previously published data of volcanoes with similar characteristics in the SVZ, to develop a consistent model for the compositional evolution of PVG. We explore the link between MIs and their host lava composition, and how this relate to processes of the magma plumbing system.

As shown by the geochemistry, the magmatic composition of MIs analyzed in this study varies according to each minor eruptive center, besides being more differentiated than bulk rock. These differences could be the result of local-scale mantle source heterogeneities, crustal assimilation, different melting degrees, crystal settling, mixing of two magmas, or simply due to differentiation processes.

To determine which process acts preferably on the chemical and mineral trends we use key major and trace elements ratios. In some cases, trace elements are a more powerful tool for identifying

processes like crustal contamination particularly when subducted materials, the crust of the overriding plate and erupted products have identical isotopes signature. Such is the case of the SVZ, where the recycling is considered quit intense, as the marine sediments are largely of volcanic origin from the active arc and the continental crust consist to a great extent, of plutonic rocks derived from the same source as the volcanic rocks (Wehrmann et al., 2014)

2.6.1 Storage and pre-eruptive conditions

According to seismicity studies by Estay et al. 2018, the existence of an active duplex system was determined by detecting 95 events with magnitudes up to Mw = 4.1. It was also possible to determine that the brittle-ductile limit of the crust is about 12 km deep, an area in which the existence of a magma chamber was not evident.

The origin of Puyuhuapi basalts can be explained by partial melting processes at the base of the sub-continental lithosphere, as a response to a local extensional tectonic stress along the LOFZ (Gonzalez Ferran et al., 1995). Results from Raman spectroscopy, suggest that depths less than 12 Km should be discarded as possible magmatic storage areas.

From mineral chemistry, according to the MgO content we can determine that the olivines analyzed in this study correspond to cortical olivine. Using the forsteritic content of Puyu 9 olivine D33 (Fo 87) and by considering that 90% of the CO_2 is retained in the bubble of our MI, we can obtain a crystallization depth of 23 km. Using the composition of a recrystallized MI also located at the center of the crystal, we can determine a temperature of 1233.4 °C and an oxygen fugacity QFM + 1.06.

Our data indicate that the average crystallization pressure for Puyu 9 is 5 Kbar and for Puyu 4 and Puyu 18 is 4 Kbar, which corresponds to a depth of 18 and 15 km respectively and it is considered the minimum depth at which magmatic storage occurs. Textural evidence, sizes and rims reactions of the olivine minerals with the groundmass, plus the petrology of MI, indicate that there was a period of magma residence in the crust.

2.6.1.1 Temperatures

The temperature at which MIS are in equilibrium with the host were calculated by the Petrolog software, ranging from 1100 to 1280°C (1172°C avg.), with temperature obtained by the Reverse Crystallization setting and corresponding to MI entrapment temperatures. Puyu4 MIs would have formed at higher temperature during the evolution of crystallization (**Fig. 27**)

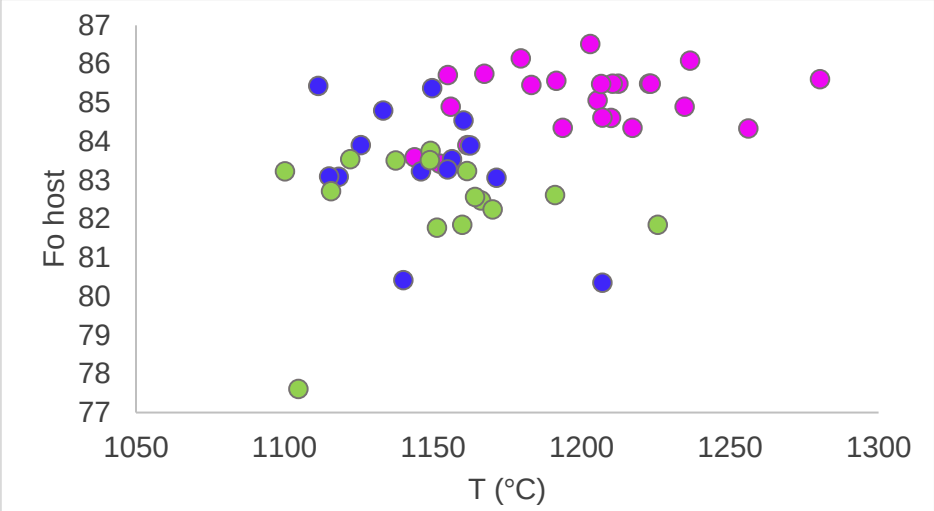

Fig. 27: Fo host content (mol %) versus entrapment temperature of MIs.

Table 5: results of the average entrapment temperature of MIs per sample, olivine %= average percentage of olivine that was returned to the composition of the MI.

MEC	T (°C)	Olivine Fo %	Olivine %
Puyu 4	1200	85.10	7.11
Puyu 9	1147	83.43	6.46
Puyu 18	1151	83.76	6.70

To obtain syn-eruptive temperatures we use olivine and glass-based thermometers from Putirka (2008) in MIs found in microlites, assuming that these are formed during the eruption. We use an empirical equation P-independent that has an R^2=0.92 and standard error estimate of 51 °C.

$$T(°C)= 754+ 109.6[Mg\#] + 25.52[MgO^{liq}] + 9.585[FeO^{liq}] + 14.87[(Na_2O+K_2O)^{liq}] -9.176\ [H_2O^{liq}] \quad (3)$$

Where $Mg\#^{liq}$ is a molar ratio and the remaining terms are weight percent oxides in a liquid or glass, Eq. (3) is applicable to any volcanic rock saturated with olivine and any other collection of phases, over the following compositional and P-T range: P = 0.0001-14.4 GPa; T = 729-2000 °C; SiO_2 = 31.5-73.64 wt. %; Na_2O+K_2O = 0-14.3 wt. %; H_2O = 0-18.6 wt. %.

Table 6: Results of geothermometer (3) applied on glass from MI hosted on olivine microlites.

Sample	T (°C)	Liquid 100*Mg#	Olivine Fo	Measured KD(Fe-Mg)
PUYU4-C26	1072	45.2	78.8	0.25
PUYU9-C37-15	1162	48.9	80.2	0.26
PUYU9-C37-18	1157	49.4	79.7	0.28
PUYU9-C38-14	1156	48.3	81.0	0.24
PUYU18-A11	1083	45.4	74.9	0.31
PUYU18-A13	1076	45.7	76.6	0.29
PUYU18-B11-93	1082	46.2	76.9	0.29
PUYU18-B43	1054	42.8	74.2	0.29

The Puyu 9 temperature it is by far greater than the other eruptive centers, which is consistent with the high content of FeO in the composition of the groundmass glass. This could be due to a thermal and / or chemical disequilibrium in the magma chamber that increased the temperature and melted parts of the minerals, raising the #Mg in the melt.

2.6.1.2 Oxybarometry

By applying the oxybarometer of olivine - spinel from Ballhaus et al. (1991), through the following equation, the oxygen fugacity was calculated based on spinel - olivine crystalline pairs.

$$\triangle \log(f_{O^2})^{FQM} = 0.27 + \frac{2505}{T} - \frac{400P}{T} - 6\log\left(X_{Fe}^{ol}\right) - \frac{3200\left(1-X_{Fe}^{ol}\right)^2}{T} + 2log(X_{Fe^{+2}}^{sp}) + 4log(X_{Fe^{+3}}^{sp}) + 2630(X_{Al}^{sp})^2/T. \quad (4)$$

Ballhaus et al. (1991) provide an empirical calibration of the O'Neill and Wall (1987) olivine-pyroxene-spinel oxybarometer, using synthetic spinel harzburgite and lherzolite assemblages between 1040 and 1300 °C and 0.3 to 2.7 Gpa Precision of this method was reported by Ballhaus et al. (1991) at $\pm$0.41 log units at oxygen fugacities above FMQ and $\pm$1.2-1.5 log units ~2 log units below FMQ.

The formulation is simplified by suppressing orthopyroxene against the ideal part of the fayalite activity in olivine. This simplification cannot be expected to be valid at XFe Ol > 0.15. As such, its application is limited to Mg-rich upper mantle-derived rocks.

Table 7: Estimated oxygen temperature and fugacity for olivine spinel pairs, a pressure of 1 GPa is assumed for the calculations

Crystalline pair	T (°C)	X Fe+2 Ol	%Fo	X Fe+2Sp	ΔFMQ
PUYU18-A44-34	957	0.14	85.63	0.67	1.60
PUYU18-C23-97	1005	0.15	84.66	0.65	1.47
PUYU18-C39-50	1089	0.15	84.85	0.57	2.23
PUYU18-C39-51	964	0.15	84.85	0.61	1.91
PUYU4C-B13-37	855	0.13	86.27	0.66	1.82
PUYU4C-B26-51	945	0.14	85.85	0.61	2.04
PUYU4C-B39-87	1028	0.15	84.52	0.57	2.03
PUYU4C-B-58	922	0.14	85.43	0.67	1.40
PUYU4C-B-59	930	0.13	86.47	0.8	0.42
PUYU4C-D31-102	900	0.14	85.82	0.63	1.84
PUYU4C-D32-111	870	0.14	85.56	0.7	1.25
PUYU4C-D41-96	861	0.14	86.19	0.65	1.83
PUYU9-A22-13	971	0.15	84.79	0.59	2.08
PUYU9-A22-14	1033	0.15	84.79	0.58	2.55
PUYU9-B34-89	931	0.14	85.95	0.64	1.89
PUYU9-D11-50	931	0.13	86.80	0.63	1.98
PUYU9-D11-46	985	0.15	85.18	0.61	1.86
PUYU9-D11-52	943	0.14	86.33	0.61	2.06

PUYU9-D13-40	976	0.15	84.80	0.58	2.03

Table 7, specifies the calculated values for the different crystalline pairs, the composition of spinel inclusions in olivine was used to determine the oxygen fugacity, the calculated fO_2 of PVG basalts is 1.8 average log units above the QFM buffer (**Fig. 28**)

Fig. 28: oxygen fugacity according to the fayalite-quartz-magnetite buffer, calculated by equation (4)

The value found for the PVG from this study is one of the highest calculated for the SVZ. At the SVZ, fO_2 values were determined at several TSVZ and CSVZ volcanoes. Ruprecht et al. (2012) estimate NNO + 0.24 to NNO + 0.53 for mafic melts at Quizapu, Rodríguez et al. (2007) show highly oxidizing conditions of NNO + 1.5 to NNO + 2 for Longaví, while Witter et al. (2004) indicate a range from QFM to NNO + 1 at Villarrica. Bouvet de Maisonneuve et al. (2012) determine QFM to NNO for Llaima, and Watt et al. (2013) estimate QFM + 1 for Apagado and Minchinmávida.

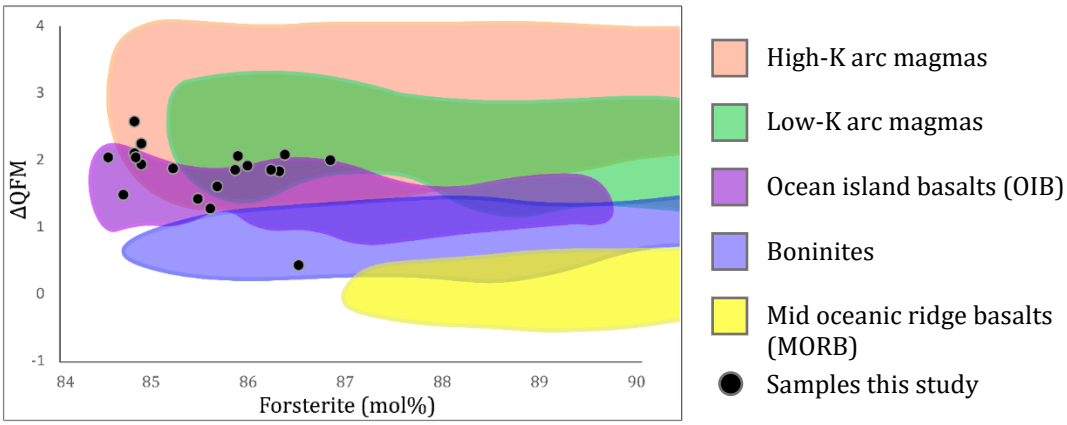

Fig. 29: Oxidation state of olivine-spinel pairs versus forsterite content of olivine from contrasting basalts. Calculations performed following Ballhaus et al. (1991). Modified image from Evans et al., 2012.

Mid-ocean ridges and subduction related volcanic arcs are the two major contributors to the global magma budget, and previous work has suggested that arc lavas have a significantly higher oxidation state than mid-oceanic ridge basalt (MORB, e.g., Eggins, 1993; Kelley and Cottrell, 2009). Potential oxidants include water, oxidized iron, sulfur, and carbon (Kelley and Cottrell, 2009) from the subducting slab, sediments, and mantle lithosphere. As seen on **Fig. 29** oxygen fugacity calculated for the PVG is in the range found for arc magmas.

Re-equilibration between the olivine and spinel inclusions may have occurred naturally as a result of slower cooling at the time of entrapment from temperatures slightly above the estimated liquidus. Considering that, the PVG is located in one of the main alignments of the LOFZ. This structure could facilitate a direct transport to the surface of their magmas ponded at the base of the crust and explain the observed differences with the chemical signature of larger systems in the rest of the volcanic products of the Andean arc. The high fugacity of oxygen could be a local disequilibrium registered in minerals of a restricted stage of crystallization that ascended quickly through the crust.

2.6.2 Different magma sources

The geochemical composition of the PVG alkaline lavas allows us to classify them as type 2 basalts (López-Escobar et al., 1995a), K-rich and generally enriched in incompatible elements. However, differences of trace element abundances reveals systematic differences between each MEC. Although all samples exhibit enrichment, Puyu 9 MIs are most enriched in all of the incompatible elements (**Fig. 18**). Lava samples belonging to the south lineament tend to have a similar composition and differ from the lava sample of Puyu9 located along the north lineament, allowing us to conclude that the magmas that originated from the MEC from the northern lineament differs from the south lineament, which could be due to different sources or different melting degrees.

Ratios of highly-mobile fluid over less mobile or fluid-immobile elements that should be unaffected by early differentiation like Ba/Nb and Pb/Ce display a clear distinction between samples. From **Fig. 30.d** it can be observed that MIs have a weak fluid signal, not exceeding 0.2 in Pb/Ce and 50 in Ba/b, i.e. the input of slab fluids it is a minor factor in the formation of the PVG lavas. This is also consistent with what is observed in **Fig. 30.a**, where elevated Nb/Y and La/Sm can be used to trace low degrees of melting and-or the presence of enriched components in the mantle wedge. When slab fluids have a small influence, a lower degree of melting is expected, with or without assimilation of crustal material. The low Ba/La ratio (14.9 ppm in avg.) can indicate as well a low degree of aqueous influx from the subducted oceanic crust.

Plotting Nb/Y and La/Sm versus MgO content (**Fig. 30. b, c**), the data show no much trend for differentiation, as different MECs display bounded ranges of Nb/Y, for variable contents of MgO. Conversely, data from Puyu9, show higher levels of Nb, similar to what is observed in primitive mantle normalized trace elements patterns (**Fig. 17**).

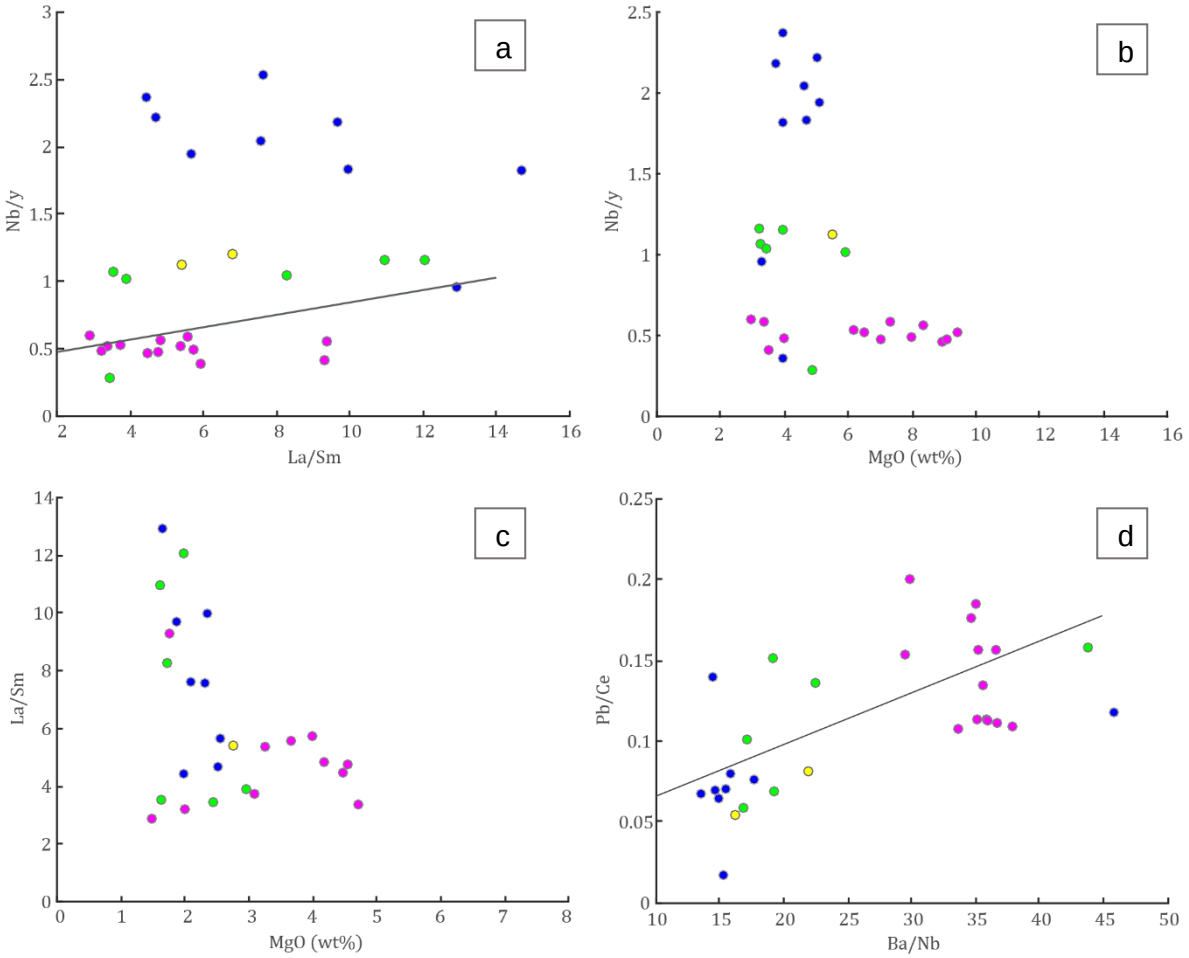

Fig. 30: melt inclusions (a) MI Nb/Y versus La/Sm with the respective trend line. (b) MI Nb/Y versus MgO (wt. %). (c) La/Sm versus MgO (wt. %). (d) Pb/Ce versus Ba/Nb, with the respective trend line. Yellow= Puyu 3, Green= Puyu 18, Blue= Puyu 9, Magenta= Puyu 4.

Considering that these are lavas the final product of monogenetic volcanism, it is very likely that they could be produced with a low degree of partial melting, since volumes of magma are very small. LREE/HREE ratios like La/Yb (17.2 avg.) in Puyuhuapi lavas represents the highest values of the SSVZ, being as high as those presented by andesites from NSVZ (Hickey-Vargas et al., 2016).

The sub-arc mantle is expected to be enriched in large ion lithophile (LIL) elements such as Cs, Rb, Ba, U, Sr and Pb (relative to the MORB mantle), and when considering that this group of elements consists of water soluble elements (Zheng, 2019). Mafic arc volcanics are also enriched in LREE and Th (Kelemen et al., 2007), which are insoluble in water but soluble in hydrous silicate melts and enriched in oceanic sediments.

HFSE such as Nb, Ta, Ti, Zr and HREE tend to be immobile in subduction zone fluids. Therefore fluid mobile element ratio (Ba/Th) versus melt mobile elements (La/Sm) diagram can be used to test the influence of slab fluids and sediment melt in magma (**Fig. 31**). Most MIs follow a low

degree of slope, emphasizing the importance of sediment-melt contributions, and do not seem to cluster into groups. It is important to note that as a volcanic group, the incompatible element enrichment is due to sediment melting.

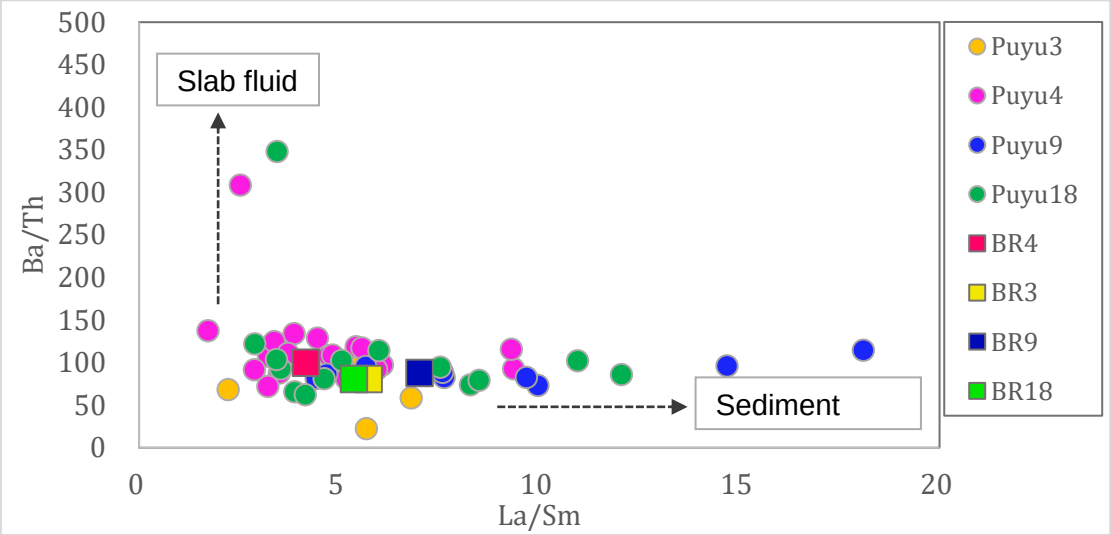

Fig. 31: MI fluid mobile element ratios, Ba/Th versus La/Sm. Circle: Melt inclusions, Square: bulk rock.

As seen in **Fig. 30.a** the one of the differences of Puyu 9 is the greater amount of Nb/Y and La/Sm, which can indicate lower degrees of melting and-or the presence of enriched components in the mantle wedge. To better clarify which factor is the most important, in **Fig. 32**, we plot K/Rb versus Rb. It is expected that sub crustal-magmas decrease their K/Rb ratio and increase K/Ba, K/La, Rb/Ba and Rb/La ratios when they are contaminated with crustal material enriched in K and Rb with respect to Ba and La (López-Escobar et al. 1995a) Rb content in our MI of Puyu 9 is as high as back arc basalts from MEC between 38° and 39°S (Muñoz and Stern, 1989).

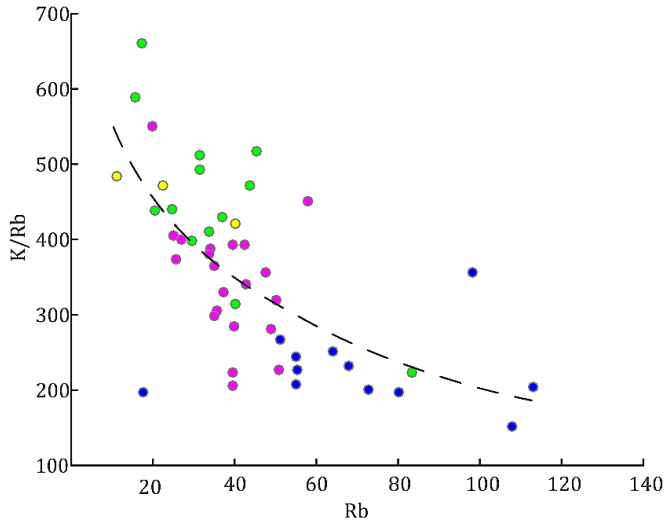

Fig. 32: incompatible element ratio versus Rb diagram. Symbols are the same from Fig. 30.

Magma erupted early in a sequence typically is relatively evolved in terms of chemical composition (lower MgO, higher total alkalis and higher incompatible element abundances) compared with magma erupted toward the end of an eruption sequence (McGee and Smith, 2016, and references therein), whereas the magmas ascending through the mantle become enriched due to reactions with the local basement, which becomes progressively depleted over time and thus leads to the eruption of magmas more similar to the original input composition over the course of the eruption. As seen in (**Fig. 33**), there is a progression in the abundance of incompatible elements from Puyu 9 to Puyu 4, which shows a great similarity with ratios found in Paleozoic metasedeimentary rocks (S-Type), suggesting that the lavas that form Puyu 9 would early in the sequence.

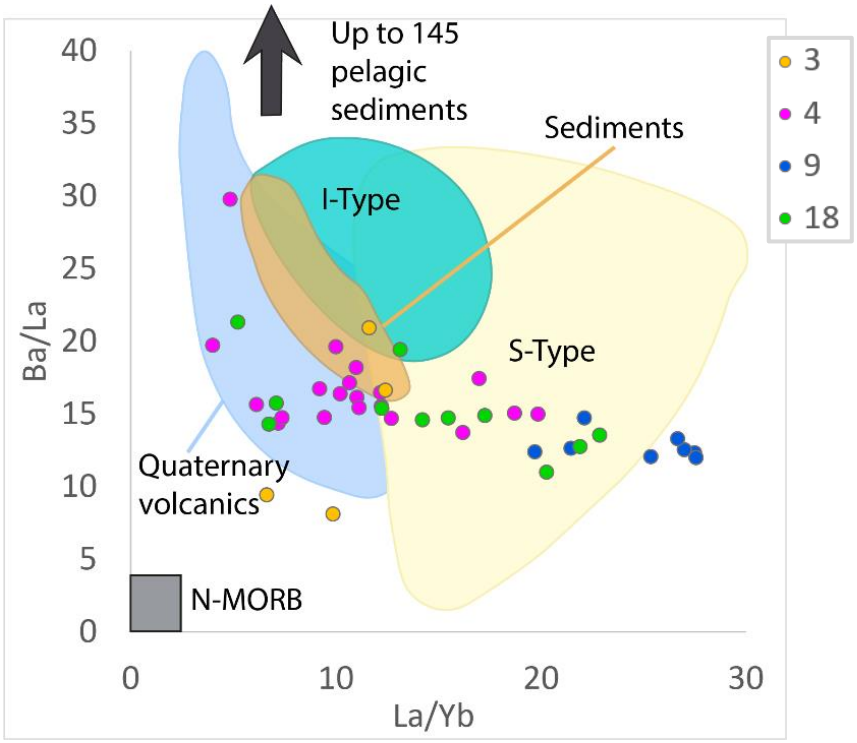

Fig. 33: Ba/La versus La/Yb, S-type= Paleozoic metasedimentary rocks, I-type= plutonic rocks of the Patagonian batholith, sediments= southern Chile trench sediments. Data from Kilian and Behrman 2003.

Rocks generated from the mantle with residual garnet, have a greater Th/Yb ratio, where Th is incompatible and Yb is compatible in garnet, so the Th would be enriched in the melt. As seen in **Fig. 34,** Puyu 9 has the greatest garnet component in the source, with Th/Yb= 3.7 on average for Puyu 9 and Th/Yb= 2.42 on average for the rest of the samples. It is likely that all melts originated in the presence of the residual garnet. As garnet is stable at depths of ~80 km in peridotite (e.g. McKenzie and O'Nions, 1991) this indicates the variable importance of an asthenospheric source (McGee et al., 2013).

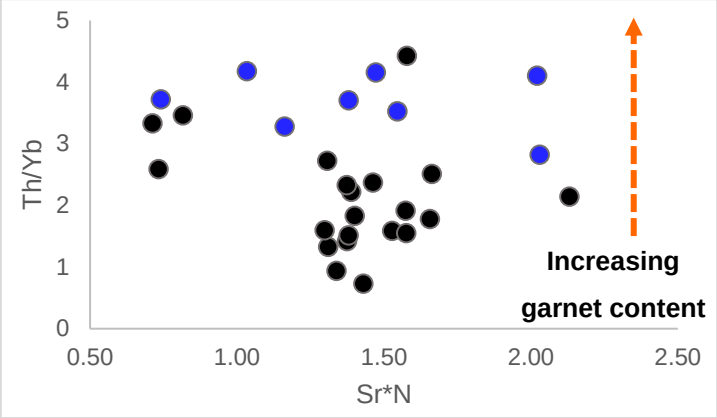

Fig. 34: Sr*$_N$ is calculated as $Sr_N/\sqrt{(Pr_N * Nd_N)}$, where each element is normalized to primitive mantle after McDonough and Sun (1995). Blue circles= Puyu 9, black circles= Puyu3, Puyu4 and Puyu 18 altogether.

2.6.2.1 Magmatic differentiation

Despite the fact that the bulk rock data show a very primitive geochemical signature for the PVG, this is not reflected in the chemistry of the MIs, with the vast majority of these more evolved. This compositional variation is a consequence of the crystal – liquid fractionation process. Although small-scale basalt eruptions are generally fed by rapidly ascending melts, which does not form in magma chambers, none of the known volcanic fields produce basalt that are truly primitive; so, differentiation has occurred to some degree in all cases. (McGee and Smith, 2016). More differentiated compositions can be explained by deep-seated crystallization of mineral phases, which are not present as phenocrysts in the erupted magma.

Differentiation processes with or without assimilation explain increasing alkali contents positively correlated with SiO_2 with higher silica contents. The complexity of geochemical characteristics may be enhanced by contamination with crustal materials during the ascent of magma to the surface.

To understand the processes involved in the differentiation of the primary magma, the composition of MIs and the average composition of the minerals found in the lava of the PVG were plotted (**Fig. 35**). We can observe that MIs follow the track of a liquid that is depleted in major elements forming spinel, olivine and clinopyroxene. The dotted line represents data interpolation, in the sense of differentiation.

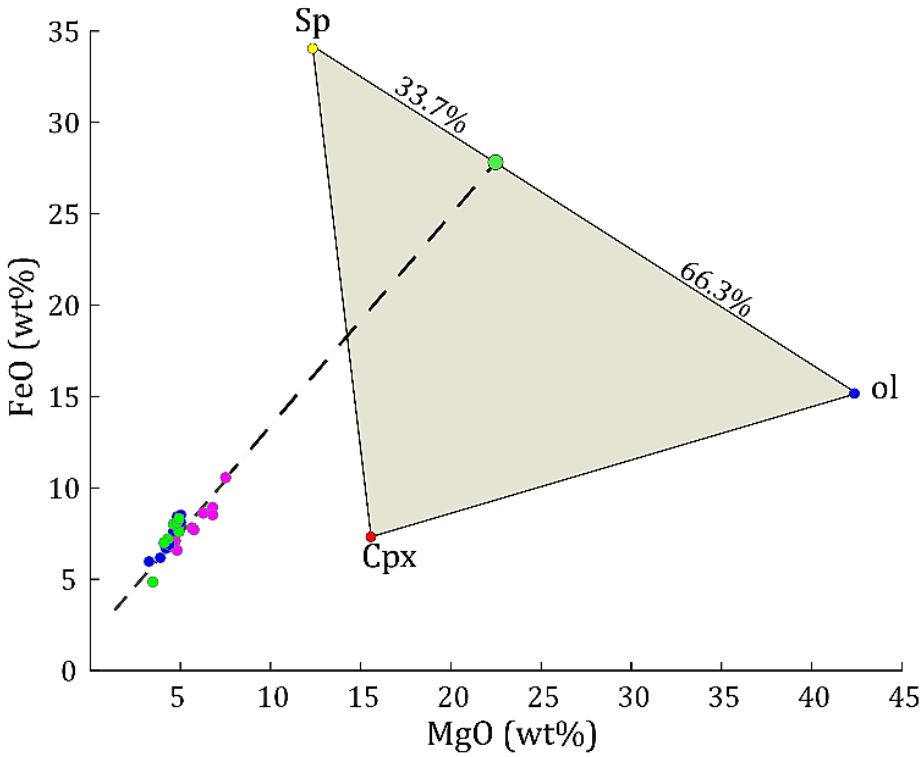

Fig. 35: MI FeO versus MgO content, dotted line represent the compositional path followed by the extraction of a solid phase (green circle).

Taking into account that Cpx is not an abundant phase in our paragenesis, the probable fractioned solid corresponds to 66 % of spinel and 34 % of Ol. Another feature to be considered is the systematic evolution in the composition of magma during eruption.

Trace elements data show enrichment of Rb, Ba, Y, Zr, Nb, REE in MIs, consistent with a model dominated by fractional crystallization of olivine + spinel ± clinopyroxene.

2.6.2.2 Disequilibrium conditions recorded in the PVG lavas

Textual evidence in Ol and Cpx crystals, such as resorptions and zoning, allow us to determine a change in the magmatic conditions. Trace element distribution in the olivine crystals, with a higher level of Ca towards the rims, and the increases of iron content in the groundmass glass on Puyu 18 and Puyu 9 (**Fig. 36**), indicate a possible heating of the magmatic system. The heating, melted part of the minerals and increased the amount of iron in the glass (**Fig. 36)**

It is unlikely that the heating can be due to an input of primitive magma because MIs do not register a notable variability in their composition. Such heating input occurs at a late stage of crystallization since it affects crystals with a border of Fo_{76}. This same increase in FeO content allows crystallization of magnetite in Puyu9 and magnetite high in chromium in Puyu 3

Puyu 4 is the cone with the most primitive MIs and does not show greater disequilibrium conditions, suggesting that it could be responsible for the heating that affected the other CEM.

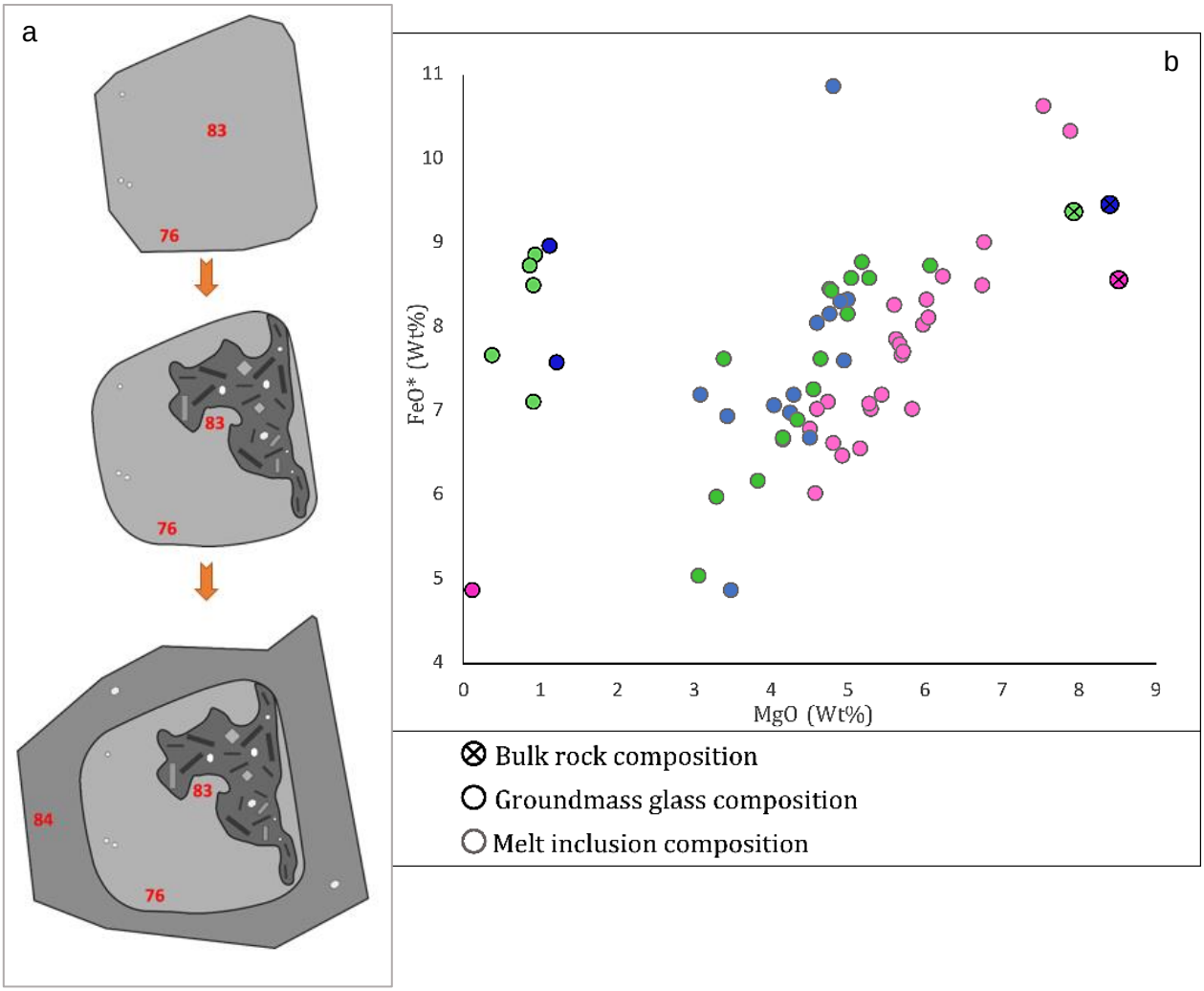

Fig. 36: a) Schematic representation of the succession of mineral disequilibrium and subsequent crystallization. b) MgO and FeO (wt. %) content in melt inclusion and groundmass.

2.6.3 Chemical modeling

To determine the chemical evolution of the system and how the chemistry of the inclusions was produced, we used the rhyolite-MELTS v.1.0.2. Algorithm (Ghiorso and Gualda, 2015; Gualda et al., 2012). Inclusions with higher #Mg were considered to represent the major element composition closest to a primary magma and bulk rocks, were used as the starting composition. We established initial conditions of 6 Kbar and 1300°C, oxygen fugacity of QFM+1 (quartz-fayalite-magnetite) and absent = calculated by the software from the initial composition of the rock., water content of 2.0 wt% and a CO_2 content of 0.2 wt%. Polybaric (6 Kbar-1 Kbar), isobaric (6 Kbar) at equilibrium, and perfect fractional crystallization models have been generated.

We can observe that the composition of MIs can be obtained with crystallization at equilibrium from an initial “parental” bulk rock composition of Puyu 4 for the MEC in the southern lineament. The composition of Puyu 9 MIs can be obtained with the initial “parental” bulk rock composition of

Puyu 9 (**Fig. 37, 38**).For Puyu 4, the system calculates an oxygen fugacity of 0.37 above FQM, and for Puyu 9 -0.41. In the case of Puyu4, we calculated that MIs are trapped at a temperature of 1237°C, and that the liquidus temperature is 1256°C in an isobaric system.

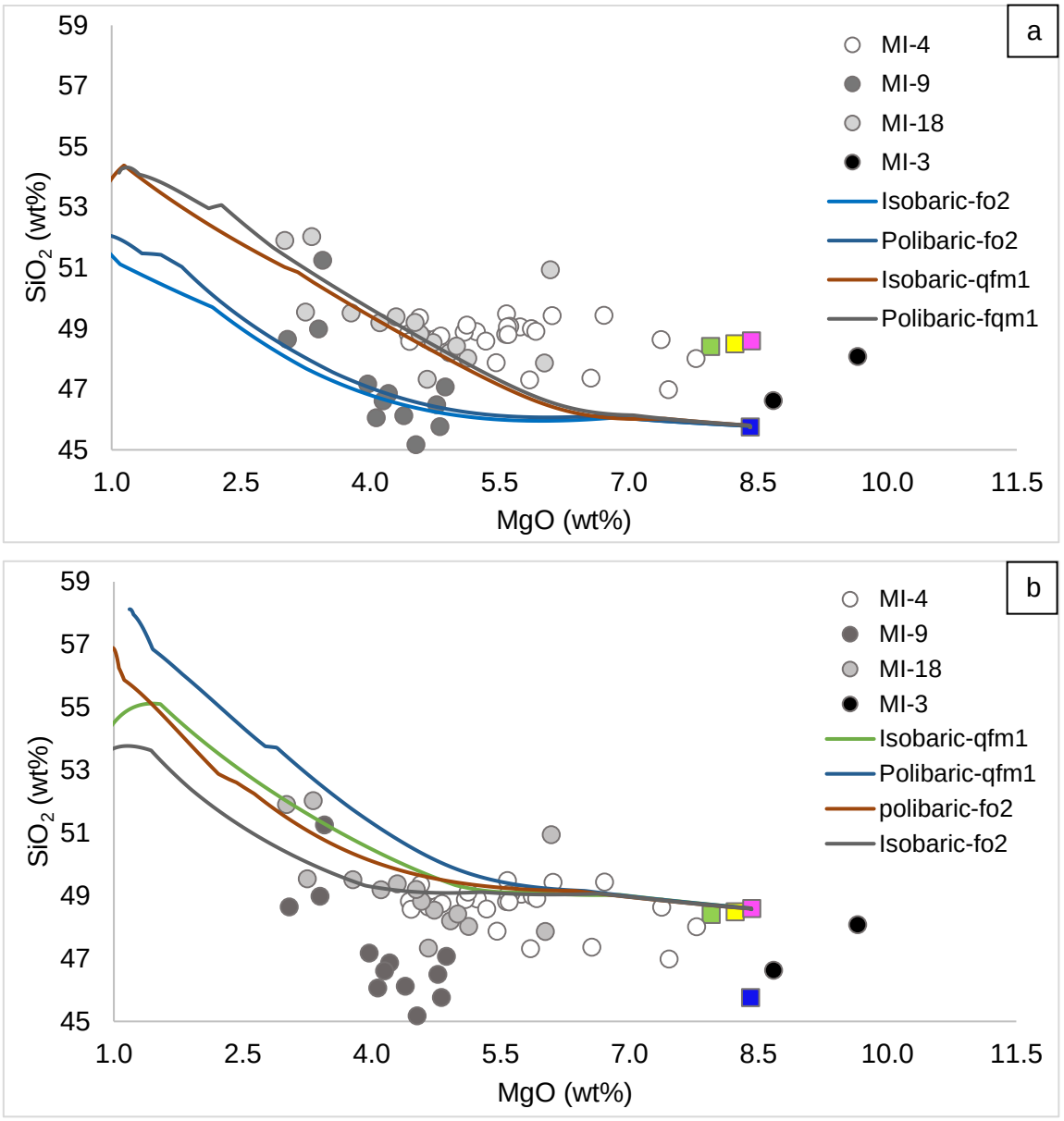

Fig. 37: SiO_2 versus MgO content for the Puyuhuapi lavas and melt inclusions. Curves represent the evolution paths of residual melts modeled using Rhyolite-MELTS (Gualdaet al., 2012; Ghiorso and Gualda, 2015). a) Initial composition Puyu9 bulk rock. b) Initial composition Puyu4 bulk rock. The fo2 curves they have been modeled with the oxygen fugacity that calculates the algorithm and the fqm1 have been modeled by imposing a fugacity of FQM + 1.

It should be noted that when Puyu 4 bulk rock is used as an initial composition, the modelling does not agree with Puyu 9 MI compositions. Conversely, by varying the oxygen fugacity, the composition of Puyu 9 is able to generate the composition of some inclusions from the southern lineament cones.

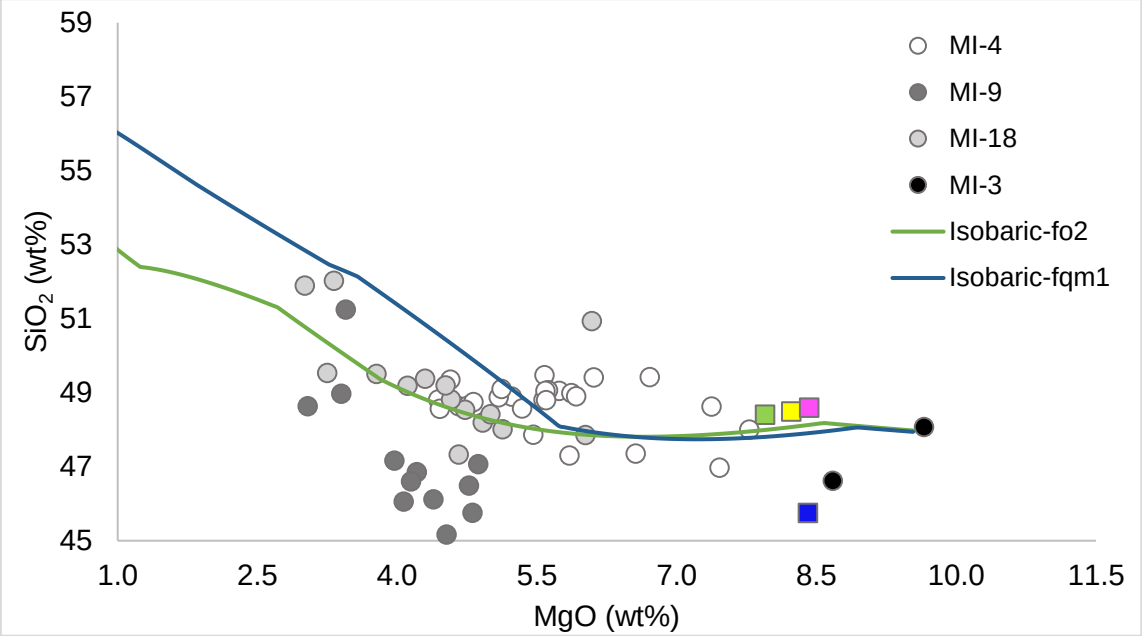

Fig. 38: SiO_2 versus MgO content for the Puyuhuapi lavas and melt inclusions. Curves represent the evolution paths of residual melts modeled using Rhyolite-MELTS (Gualdaet al., 2012; Ghiorso and Gualda, 2015). Initial composition C7 Melt inclusion from Puyu3. The fo2 curves they have been modeled with the oxygen fugacity that calculates the algorithm and the fqm1 have been modeled by imposing a fugacity of FQM + 1.

Using the composition of a recrystallized melt inclusion (C-7) of Puyu3 as the initial composition, we can also generate the composition of the majority of the inclusions of the southern lineament and the composition of the bulk rock. With an oxygen fugacity of QFM + 0.05, we can generate the composition of Puyu 18 and Puyu 4. In addition, an oxygen fugacity of QFM +1 can generate compositions close to Puyu 4 MI. Puyu 9 follows an independent compositional evolution.

2.6.4 Petrogenetic model

Considering the depth and temperature at which melt inclusions formed the following magmatic model of multi transient reservoirs, considering that the chemistry of melt inclusions evolves independently (**Fig. 39**). Low volumes of magma are generated at the base of the asthenosphere in the garnet stability field.

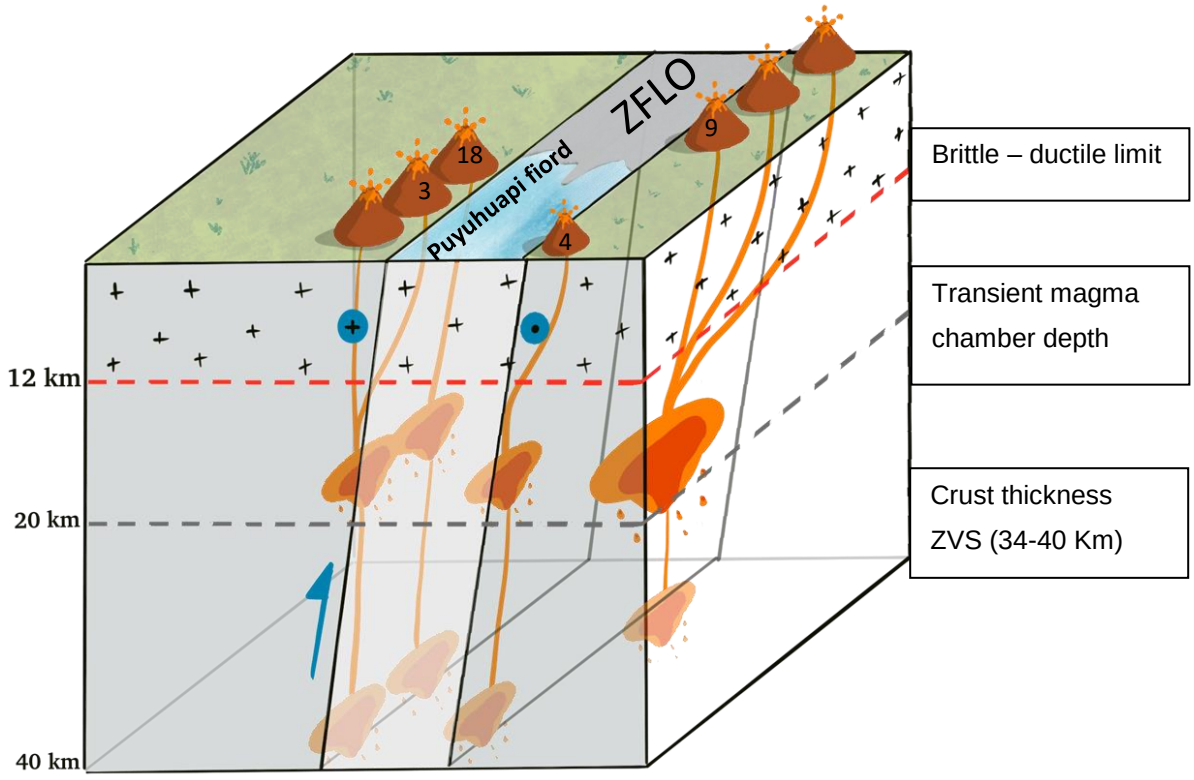

Fig. 39: Schematic representation of the depths of the reservoirs associated to the Puyuhuapi cones.

The crystallization begins with an early fractionation of olivine. Even the most primitive basalts show evidence of having undergone fractional crystallization, as their MgO contents are <11%, and their Ni and Cr abundances are both lower than those expected in mantle-derived primary magmas.

The magma would then ascend from its source to a depth of about 20 km, where a geothermal gradient of 45°◦C/kmin is assessed for the Chilean Plio-Quaternary volcanic belt (Aravena et al., 2016). At this stage, a temporary stagnation of magma occurs, along with a heat input that increases the temperature of the system and generates disequilibrium in mineral textures and a increase of FeO and MgO on the groundmass. This same heat input could be the trigger for the cone Puyu 9 eruption, which in turn initiated hydraulic fracturing of the overlying rock lavas and consequent enrichment in incompatible elements of the magma.

2.7 Conclusions

The Puyuhuapi volcanic group is an example of how complex a monogenetic volcanic system can be, as has been verified in different studies. Mantle source regions are almost never homogenous or simple and very few volcanoes involve the melting of a compositionally discrete source. Although in this type of magmatism the residence time in the crust is shorter compared to larger volcanic systems, the magma would not ascend directly from the mantle, new magma recharges can generate imbalance in the minerals that have already crystallized in different the transient reservoirs. The biggest difference in terms of a major volcanic system is the plumbing system. When the fracture of the wall rock and the exit of the magma take place, the different conducts would be closed, becoming extinct.

This opening of new conducts for the magma extrusion through each minor eruptive center allows the magma to be quite enriched (equivalent even with some values found in the SVZN) despite being in an area where the crust is thinned.

The analysis of geochemical data from MIs helped determine that the magma that forms the PVG lavas is generated from two different mantle sources, and is probably localized in the garnet stability field as suggested for high LILE/HFSE ratios. Puyu 9 lavas would have a deeper magmatic source with a high content of garnet.

Characteristics such as the lower amount of MgO and higher amount of alkalis of Puyu 9, in addition to the greater enrichment of incompatible elements (Sr, Zr, Rb), allowed us to determine that Puyu 9 not only has a deeper source of magma but was probably one of the first MEC to erupt, experiencing greater wall-rock contamination that most likely would have generated a more enriched composition.

The particular geochemical signature of the PVG alkaline lavas would be influenced largely by the melting of slab sediments rather than fluid input, which would be consistent with low degrees of melting (elevated Nb/Y and La/Sm), and the location of the system (farther west than most volcanic features in the southern volcanic zone) makes the slab more dehydrated.

The LOFZ curves in the area of Puyuhuapi, causing a local extension in that area of the crust, the extensional-shear fractures oriented subparallel to the maximum horizontal stress favored a direct transport to the surface of a low magma input rate ponded deeper in the crust.

Olivine hosted-MIs allow us to constrain the P-T conditions of the deep reservoirs, with minimum pressures of 4 K bar (south lineament) and 5 Kbar (north lineament) and a maximum temperature of 1280°C, with 1.8 average log units above the QFM buffer.

The large amount of recrystallized MIs and disequilibrium features recorded in minerals and the groundmass are evidence of a magma reservoir in both lineaments. On the other hand, we

determined that although olivine-hosted MIs are formed at an early stage of the magmatic evolution, most of them suffered some degree of fractionation of a solid phase, formed mostly by olivine and spinel.

When using mostly homogeneous inclusions there is a part of the information recorded in the recrystallized inclusions that are lost, the latter being recrystallized had a longer residence time in the cortex, prior to the eruption and could catch less differentiated magma.

BIBLIOGRAPHY

Abràmoff, M. D., Magalhães, P. J., & Ram, S. J. (2004). Image Processing with ImageJ. *Biophotonics International*, *11 (7)*, 36–42.

Aravenaa, D, Muñoz, Morataa, D, Lahsena, Paradaa, M.A., Dobson, P. (2016) Assessment of high enthalpy geothermal resources and promising areas of Chile. Geothermics; 59; 1-13

Aster, E. M., Wallace, P. J., Moore, L. R., Watkins, J., Gazel, E., & Bodnar, R. J. (2016). Reconstructing CO2 concentrations in basaltic melt inclusions using Raman analysis of vapor bubbles. *Journal of Volcanology and Geothermal Research*, *323*, 148–162. https://doi.org/10.1016/j.jvolgeores.2016.04.028

Audétat, A., & Lowenstern, J. B. B. (2014). *Melt Inclusions*. *Treatise on Geochemistry* (Vol. 13). https://doi.org/10.1016/B978-0-08-095975-7.01106-2

Bouvet de Maisonneuve, C., Dungan, M. A., Bachmann, O., & Burgisser, A. (2012). Insights into shallow magma storage and crystallization at Volcán Llaima (Andean Southern Volcanic Zone, Chile). *Journal of Volcanology and Geothermal Research*, *211–212*, 76–91. https://doi.org/10.1016/j.jvolgeores.2011.09.010

Burgisser, A., & Scaillet, B. (2007). Redox evolution of a degassing magma rising to the surface. *Nature*, *445*(7124), 194–197. https://doi.org/10.1038/nature05509

Cannatelli, C., Doherty, A. L., Esposito, R., Lima, A., & De Vivo, B. (2016). Understanding a volcano through a droplet: A melt inclusion approach. *Journal of Geochemical Exploration*, *171*, 4–19. https://doi.org/10.1016/j.gexplo.2015.10.003

Cañón-Tapia, E., & Walker, G. P. L. (2004). Global aspects of volcanism: The perspectives of “plate tectonics” and “volcanic systems.” *Earth-Science Reviews*, *66*(1–2), 163–182. https://doi.org/10.1016/j.earscirev.2003.11.001

Carmichael ISE, Ghiorso MS (1990) Controls on oxidation-reduction relations in magmas. Rev Mineral Geochem 24:191-212

Carmichael, I. S. E. (1991). The redox states of basic and silicic magmas: a reflection of their source regions? *Contributions to Mineralogy and Petrology*, *106*(2), 129–141. https://doi.org/10.1007/BF00306429

Cembrano, J., & Hervé, F. (1993). The Liquiñe–Ofqui fault zone: a major Cenozoic strike slip duplex in the Southern Andes. Second International Symposium of Andean Geodynamics, Oxford, extended abstracts, pp. 175–178.

Cembrano, J., Hervé, F., & Lavenu, A. (1996). The Liquine Ofqui fault zone: a long-lived intra-arc fault system in southern Chile. Tectonophysics, 259(1), 55-66.

Cembrano, J., & Lara, L. (2009). The link between volcanism and tectonics in the southern volcanic zone of the Chilean Andes: A review. *Tectonophysics*, *471*(1–2), 96–113. https://doi.org/10.1016/j.tecto.2009.02.038

Cembrano, J., Lavenu, A., Reynolds, P., Arancibia, G., López, G., & Sanhueza, A. (2002). Late Cenozoic transpressional ductile deformation north of the Nazca–South America–Antarctica triple junction. Tectonophysics, 354(3), 289-314.

Danyushevsky, L. V., & Plechov, P. (2011). Petrolog3: Integrated software for modeling crystallization processes. *Geochemistry, Geophysics, Geosystems*, *12*(7). https://doi.org/10.1029/2011GC003516

Deer WA, Howie, RA, Zussman J (1992). An introduction to the rock-forming minerals. Harlow, UK: Longman Scientific and Technical.

Demant, A., Hervé, F., Pankhurst, R., & Magnette, B. (1994). Alkaline and calc-alkaline Holocene basalts Irom minor volcanic centres in the Andes 01 Aysén, Southem Chile. In Congreso Geológico Chileno (No. 7, pp. 1326-1330).

Dixon J & Stolper E (1995) An experimental study of water and carbon dioxide solubilities in mid-ocean ridge basaltic liquids. Part II: Applications to degassing. J Petrol 36:1633-1646

Eggins, S. M. (1993). Origin and differentiation of picritic arc magmas, Ambae (Aoba), Vanuatu. *Contributions to Mineralogy and Petrology*, *114*(1), 79–100. https://doi.org/10.1007/BF00307867

Espinoza, W. & Fuenzalida, R., (1971). Geología de las Hojas Isla Riveros, Puerto Aisén y Balmaceda, entre los paralelos 45 y 46° Lat- Sur (Inédito), Instituto de Investigaciones Geológicas-Corporación de Fomento de la Producción, 54p. Santiago.

Fine GJ, Stolper EM (1986) Carbon dioxide in basaltic glasses: concentrations and speciation. Earth Planet Sci Lett 76:263-278

Ford, C. E., Russell, D. G., Craven, J. A., & Fisk, M. R. (1983). Olivine-Liquid Equilibria : Temperature , Pressure and Composition Dependence of the Crystal / Liquid Cation Partition Coefficients for Mg , Fe 2 + , Ca and Mn, *24*, 256–265.

Frezzotti, M.-L. (2001). Silicate-melt inclusions in magmatic rocks: applications to petrology. *Lithos*, *55*(1–4), 273–299. https://doi.org/10.1016/S0024-4937(00)00048-7

Fuenzalida, R., & Etchart, H. (1974) Evidencias de migración volcánica reciente desde la línea de volcanes de la Patagonia chilena. Symposium Internacional de Volcanología, 9-14 septiembre 1974. pp.1-5.

Fuenzalida, R., & Etchart, H. (1975). Geología del territorio de Aysén comprendido entre los 43°45' y los 45 latitud Sur. Inst. Invest. Geol., Santiago, Chile, 99.

Gaetani, G. A., O'Leary, J. A., Shimizu, N., Bucholz, C. E., & Newville, M. (2012). Rapid reequilibration of H 2O and oxygen fugacity in olivine-hosted melt inclusions. *Geology*, *40*(10), 915–918. https://doi.org/10.1130/G32992.1

Ghiorso, M.S. & Gualda, G.A.R. Contrib Mineral Petrol (2015) 169: 53. https://doi.org/10.1007/s00410-015-1141-8

Ghiorso, M. S., & Sack, R. O. (1991). Mineralogy and F e - Ti oxide geothermometry : thermodynamic formulation and the estimation of intensive variables in silicic magmas, (108), 485–510.

Gualda G.A.R., Ghiorso M.S., Lemons R.V., Carley T.L. (2012) Rhyolite-MELTS: A modified calibration of MELTS optimized for silica-rich, fluid-bearing magmatic systems. Journal of Petrology, 53, 875-890.

Haggerty S.E. 1991. Oxide textures a mini-atlas. In: Lindsley D.H. (Ed.). Oxide Minerals: Petrologic and Magnetic Significance. Mineralogical Society of America. Reviews in Mineralogy, 25:129-219.

Haggerty SE, Lindsley DH (editors) (1991). Oxide mineralogy of the upper mantle. Spinel mineral group: Reviews in Mineralogy, Oxide minerals: Petrologic and magnetic significance 25. Mineralogical Society of America.

Hauri, E. (2002). SIMS analysis of volatiles in silicate glasses, 2: Isotopes and abundances in Hawaiian melt inclusions. *Chemical Geology*, *183*(1–4), 115–141. https://doi.org/10.1016/S0009-2541(01)00374-6

Hauser, A. (1989). Fuentes termales y minerales en torno a la carretera austral, Regiones X-XI, Chile. Andean Geology, 16(2), 229-239.

Herd, C. D. K. (2008). Basalts as Probes of Planetary Interior Redox State. *Reviews in Mineralogy and Geochemistry*, *68*(1), 527–553. https://doi.org/10.2138/rmg.2008.68.19

Hervé, F. (1994). The Southern Andes between 39° and 44° S latitude: the geological signature of a transpressive tectonic regime related to a magmatic arc. In Tectonics of the Southern Central Andes (pp. 243-248). Springer Berlin Heidelberg

Hervé, F., Pankhurst, R. J., Drake, R., & Beck, M. E. (1995). Pillow metabasalts in a mid-tertiary extensional basin adjacent to the Liquiñe-Ofqui fault zone: the Isla Magdalena area, Aysén, Chile. Journal of South American Earth Sciences, 8(1), 33-46.

Hickey-Vargas, R., Holbik, S., Tormey, D., Frey, F. A., & Moreno Roa, H. (2016). Basaltic rocks from the Andean Southern Volcanic Zone: Insights from the comparison of along-strike and

small-scale geochemical variations and their sources. *Lithos*, *258–259*, 115–132. https://doi.org/10.1016/j.lithos.2016.04.014

Kelley, K. A., & Cottrell, E. (2009). Water and the oxidation state of subduction zone magmas. *Science*, *325*(5940), 605–607. https://doi.org/10.1126/science.1174156

Kent, A. J. R. (2008). Melt Inclusions in Basaltic and Related Volcanic Rocks. *Reviews in Mineralogy and Geochemistry*, *69*(1), 273–331. https://doi.org/10.2138/rmg.2008.69.8

Lahsen, A., López-Escobar, L., & Vergara, M. (1994). The Puyuhuapi volcanic group, Southern Andes (44 20'S): geological and geochemical antecedents. In Congreso Geológico Chileno (No. 7, pp. 1076-1079).

Lamadrid, H. M., Moore, L. R., Moncada, D., Rimstidt, J. D., Burruss, R. C., & Bodnar, R. J. (2017). Reassessment of the Raman CO2 densimeter. *Chemical Geology*, *450*, 210–222. https://doi.org/10.1016/j.chemgeo.2016.12.034

Lattard, D., Sauerzapf, U., & Käsemann, M. (2005). New calibration data for the Fe-Ti oxide thermo-oxybarometers from experiments in the Fe-Ti-O system at 1 bar, 1,000-1,300°C and a large range of oxygen fugacities. *Contributions to Mineralogy and Petrology*, *149*(6), 735–754. https://doi.org/10.1007/s00410-005-0679-2

Lindsley, D., & Frost, B. (1992). Equilibria among Fe-Ti oxides, pyroxenes, olivine and Quartz: Part I. Theory. American Mineralogist, 77, 987-1003.

Lopez-Escobar, L., Cembrano, J., & Moreno, H. (1995). Geochemistry and tectonics of the Chilean southern Andes basaltic Quaternary volcanism (37-46°S). *Revista Geologica de Chile*, *22*(2), 219–234. https://doi.org/10.5027/andgeoV22n2-a06

López-Escobar, L. & Moreno, H. 1994. Geochemical characteristics of the Southern Andes basaltic volcanism associated with the Liquiñe–Ofqui fault zone between 39° and 46°S. Congreso Geológico Chileno, No. 7, Actas, 2, 1388–1393.

Lowenstern, J. B. (1995). Applications of silicate-melt inclusions to the study of magmatic volatiles. *Magmas, Fluids and Ore Deposits. Mineralogical Association of Canada Short Course*, *23*(June), 71–99.

Massare, D., Métrich, N., & Clocchiatti, R. (2002). High-temperature experiments on silicate melt inclusions in olivine at 1 atm: Inference on temperatures of homogenization and H2O concentrations. *Chemical Geology*, *183*(1–4), 87–98. https://doi.org/10.1016/S0009-2541(01)00373-4

McGee, L. E., Brahm, R., Rowe, M. C., Handley, H. K., Morgado, E., Lara, L. E., … Valdivia, P. (2017). A geochemical approach to distinguishing competing tectono-magmatic processes preserved in small eruptive centres. *Contributions to Mineralogy and Petrology*, *172*(6), 1–26. https://doi.org/10.1007/s00410-017-1360-2

McGee, L. E., Millet, M. A., Beier, C., Smith, I. E. M., & Lindsay, J. M. (2015). Mantle heterogeneity controls on small-volume basaltic volcanism. *Geology*, *43*(6), 551–554. https://doi.org/10.1130/G36590.1

McGee, L. E., Millet, M. A., Smith, I. E. M., Németh, K., & Lindsay, J. M. (2012). The inception and progression of melting in a monogenetic eruption: Motukorea Volcano, the Auckland Volcanic Field, New Zealand. *Lithos*, *155*, 360–374. https://doi.org/10.1016/j.lithos.2012.09.012

Mcgee, L. E., & Smith, I. E. M. (2016). Interpreting chemical compositions of small scale basaltic systems : A review. *Journal of Volcanology and Geothermal Research*, *325*, 45–60. https://doi.org/10.1016/j.jvolgeores.2016.06.007

McGee, L. E., & Smith, I. E. M. (2016). Interpreting chemical compositions of small scale basaltic systems: A review. *Journal of Volcanology and Geothermal Research*, *325*, 45–60. https://doi.org/10.1016/j.jvolgeores.2016.06.007

McGee, L. E., Smith, I. E. M., Millet, M. A., Handley, H. K., & Lindsay, J. M. (2013). Asthenospheric control of melting processes in a monogenetic basaltic system: A case study of the Auckland volcanic field, New Zealand. *Journal of Petrology*, *54*(10), 2125–2153.

https://doi.org/10.1093/petrology/egt043

Metrich, N., & Wallace, P. J. (2008). Volatile Abundances in Basaltic Magmas and Their Degassing Paths Tracked by Melt Inclusions. *Reviews in Mineralogy and Geochemistry*, *69*(1), 363–402. https://doi.org/10.2138/rmg.2008.69.10

Moore, L. R., Gazel, E., Tuohy, R. M., Lloyd, A., Esposito, R., Steele-macinnis, M., … Bodnar, R. J. (2015). Bubbles matter: An assessment of the contribution of vapor bubbles to melt inclusion volatile budgets. *American Mineralogist*, *100 (4)*(Mi), 806–823.

Mutchler, S.R. & Fedele, L. & Bodnar, R.J.. (2008). Analysis Management System (AMS) for reduction of laser ablation ICPMS data. Laser-Ablation-ICPMS in the Earth Sciences: Current Practices and Outstanding Issues. 40. 318-327.

Németh, K., & Kereszturi, G. (2015). Monogenetic volcanism: personal views and discussion. *International Journal of Earth Sciences*, *104*(8), 2131–2146. https://doi.org/10.1007/s00531-015-1243-6

Németh, K., White, J. D. L., Reay, A., & Martin, U. (2003). Compositional variation during monogenetic volcano growth and its implications for magma supply to continental volcanic fields. *Journal of the Geological Society*, *160*(4), 523–530. https://doi.org/10.1144/0016-764902-131

O'Neill HStC, Wall VJ (1987) The olivine-orthopyroxene-spinel oxygen geobarometer, the nickel precipitation curve, and the oxygen fugacity of the Earth's upper mantle. J Petrol 28:1169-1191

Pankhurst, R. J., Weaver, S. D., Hervé, F., & Larrondo, P. (1999). Mesozoic – Cenozoic evolution of the North Patagonian Batholith in Aysén , southern Chile. *Journal of the Geological Society, London*, *156*, 673–694.

Papale, P., Moretti, R., & Barbato, D. (2006). The compositional dependence of the saturation surface of H 2O + CO 2 fluids in silicate melts. *Chemical Geology*, *229*(1–3), 78–95. https://doi.org/10.1016/j.chemgeo.2006.01.013

Pardo, M., Comte, D., & Monfret, T. (2002). Seismotectonic and stress distribution in the central Chile subduction zone. Journal of South American Earth Sciences, 15(1), 11–22. doi:10.1016/s0895-9811(02)00003-2

Pardo-Casas, F., Molnar, P., 1997. Relative motion of the Nazca (Farallón) and South American plates since late Cretaceous times. Tectonics 6, 233–248. Sigurdsson, H. 1999. Encyclopedia of volcanoes, academic press, pp. 683-694.

Paton, C., Hellstrom, J., Paul, B., & Hergt, J. (2011). Iolite : Freeware for the visualisation and processing of mass spectrometric, 2508–2518. https://doi.org/10.1039/c1ja10172b

Putirka, K. D. (2008). Thermometers and Barometers for Volcanic Systems. *Reviews in Mineralogy and Geochemistry*, *69*(1), 61–120. https://doi.org/10.2138/rmg.2008.69.3

Rodríguez, C., Sellés, D., Dungan, M., Langmuir, C., & Leeman, W. (2007). Adakitic dacites formed by intracrustal crystal fractionation of water-rich parent magmas at Nevado de Longaví volcano (36.2°S; Andean Southern Volcanic Zone, Central Chile). *Journal of Petrology*, *48*(11), 2033–2061. https://doi.org/10.1093/petrology/egm049

Roedder, E. (1979). Origin and significance of magmatic inclusions. *Bulletin de Minéralogie*, *102*(5), 487–510. https://doi.org/10.3406/bulmi.1979.7299

Roeder, P. L., & Emslie, R. F. (1970). Olivine-liquid equilibrium. *Contributions to Mineralogy and Petrology*, *29*(4), 275–289. https://doi.org/10.1007/BF00371276

Ruprecht, P., Bergantz, G. W., Cooper, K. M., & Hildreth, W. (2012). The crustal magma storage system of volcán quizapu, chile, and the effects of magma mixing on magma diversity. *Journal of Petrology*, *53*(4), 801–840. https://doi.org/10.1093/petrology/egs002

Severs, M. J., Azbej, T., Thomas, J. B., Mandeville, C. W., & Bodnar, R. J. (2007). Experimental determination of H 2 O loss from melt inclusions during laboratory heating: Evidence from

Raman spectroscopy. *Chemical Geology*, *237*(3–4), 358–371. https://doi.org/10.1016/j.chemgeo.2006.07.008

Shaw, A. M., Hauri, E. H., Fischer, T. P., Hilton, D. R., & Kelley, K. A. (2008). Hydrogen isotopes in Mariana arc melt inclusions: Implications for subduction dehydration and the deep-Earth water cycle. *Earth and Planetary Science Letters*, *275*(1–2), 138–145. https://doi.org/10.1016/j.epsl.2008.08.015

Silver LA, Ihinger PD, Stolper E (1990) The influence of bulk composition on the speciation of water in silicate glasses. Contrib Mineral Petrol 104:142-162

Smith, I. E. M., Blake, S., Wilson, C. J. N., & Houghton, B. F. (2008). Deep-seated fractionation during the rise of a small-volume basalt magma batch: Crater Hill, Auckland, New Zealand. *Contributions to Mineralogy and Petrology*, *155*(4), 511–527. https://doi.org/10.1007/s00410-007-0255-z

Sorby, H.C., 1858. On the microscopic structure of crystals, indicating the origin of minerals and rocks. Geol. Soc. London Q. J. 14, 453–500.

Stern, C. R. (2004). Active Anean volcanism: its geologic and tectonic setting. *Revista Geologica de Chile*. https://doi.org/10.5027/andgeoV31n2-a01

Thomson, S. N. (2002). Late Cenozoic geomorphic and tectonic evolution of the Patagonian Andes between latitudes 42°S and 46°S: An appraisal based on fission-track results from the transpressional intra-arc Liquiñe-Ofqui fault zone. *Bulletin of the Geological Society of America*, *114*(9), 1159–1173.

Tebbens, S.F., Cande, S.C., Kovacs, L., Parra, J.C., LaBrecque, J.L., Vergara, H., 1997. The Chile ridge: a tectonic framework. Journal of Geophysical Research 102, 12035–12059.

Völker, D., Geersen, J., Contreras-Reyes, E., Sellanes, J., Pantoja, S., Rabbel, W., Thorwart, M., Reichert, C., Block, M., Weinrebe, W. R. (2012). Morphology and geology of the continental shelf and upper slope of southern Central Chile (33°S–43°S). International Journal of Earth Sciences, 103(7), 1765–1787. doi:10.1007/s00531-012-0795-y

Wallace, P. J., Kamenetsky, V. S. V., & Cervantes, P. (2015). Melt inclusion CO2 contents, pressures of olivine crystallization, and the problem of shrinkage bubbles. *American Mineralogist*, *100*(4), 787–794. https://doi.org/doi:10.2138/am--2015--5029

Watt, S. F. L., Pyle, D. M., Mather, T. A., & Naranjo, J. A. (2013). Arc magma compositions controlled by linked thermal and chemical gradients above the subducting slab. *Geophysical Research Letters*, *40*(11), 2550–2556. https://doi.org/10.1002/grl.50513

Wehrmann, H., Hoernle, K., Jacques, G., Garbe-Schönberg, D., Schumann, K., Mahlke, J., & Lara, L. E. (2014). Volatile (sulphur and chlorine), major, and trace element geochemistry of mafic to intermediate tephras from the Chilean Southern Volcanic Zone (33–43°S). *International Journal of Earth Sciences*, *103*(7), 1945–1962. https://doi.org/10.1007/s00531-014-1006-9

Weller, D. J., & Stern, C. R. (2018). Along-strike variability of primitive magmas (major and volatile elements) inferred from olivine-hosted melt inclusions, southernmost Andean Southern Volcanic Zone, Chile. *Lithos*, *296–299*, 233–244. https://doi.org/10.1016/j.lithos.2017.11.009

Wilson, M. (1997). *Igneous petrogenesis*. *Geochimica et Cosmochimica Acta* (Vol. 61). https://doi.org/10.1180/minmag.1989.053.372.15

Witter, J. B., Kress, V. C., Delmelle, P., & Stix, J. (2004). Volatile degassing, petrology, and magma dynamics of the Villarrica Lava Lake, Southern Chile. *Journal of Volcanology and Geothermal Research*, *134*(4), 303–337. https://doi.org/10.1016/j.jvolgeores.2004.03.002

Wood, B. J., Taras, B. L., & Johnson, K. E. (1990). Mantle oxidation state and its relationship to tectonic environment and fluid speciation. *Science*, *248*(1973), 337.

Appendix

Table 8: major elements composition (wt. %) of MI without recalculation, measured with electron microprobe analyzer. MI type=1: homogenous oval shaped MI, 1*: homogenous oval shaped microlite hosted MI, 2: homogenous irregular shaped MI, 3: oval shaped recrystallized MI, 4: irregular shaped recrystallized MI. α: correspond to inclusions measured with LAICPMS.

Sample	MI type	SiO_2	TiO_2	Cr_2O_3	Al_2O_3	FeO*	MnO	MgO	CaO	Na_2O	K_2O	P_2O_5	Total	H_2O
Puyu3-C13$^{\alpha}$	3	48.78	2.25	0.04	13.62	4.63	0.10	12.18	14.25	2.52	1.28	-	99.7	-
Puyu3-C7$^{\alpha}$	3	51.42	2.95	0.00	14.23	3.47	0.07	8.81	13.69	2.99	1.99	-	99.6	-
PUYU4-01-d	2	50.20	1.47	0.04	19.44	7.53	0.11	4.54	10.33	4.48	1.36	0.49	97.8	2.2
PUYU4-02-d	2	50.53	1.35	0.00	19.22	7.45	0.10	4.47	10.27	4.75	1.37	0.49	98.1	1.9
PUYU4-03-d	2	50.44	1.54	0.03	19.23	7.41	0.10	4.58	10.23	4.64	1.36	0.43	97.9	2.1
PUYU4-04-d	2	50.43	1.47	0.05	18.95	7.76	0.06	4.69	10.11	4.60	1.43	0.44	96.8	3.2
PUYU4-05-d	2	50.37	1.45	0.01	18.81	7.84	0.18	4.71	10.17	4.62	1.43	0.40	97.3	2.7
PUYU4-06-f	4	49.43	1.47	0.00	19.49	8.42	0.11	3.67	11.01	4.52	1.42	0.47	95.2	4.8
PUYU4-07-i	2	49.93	1.60	0.00	18.10	9.47	0.23	3.84	10.22	4.50	1.68	0.43	98.4	1.6
PUYU4-08-a	2	49.55	1.46	0.02	19.35	7.94	0.13	4.17	10.38	4.89	1.67	0.43	97.1	2.9
PUYU4-09-a	2	49.48	1.51	0.02	20.82	7.66	0.12	3.51	10.97	3.96	1.54	0.41	94.8	5.2
PUYU4-11-l	1	50.11	1.75	0.00	22.35	5.96	0.13	1.99	11.38	4.18	1.54	0.61	97.4	2.6
PUYU4-12-k	1	49.79	1.54	0.06	20.25	7.58	0.17	3.09	11.09	4.46	1.40	0.55	96.1	3.9
PUYU4-13-j	2	50.21	1.62	0.03	20.87	6.70	0.13	2.43	11.51	4.52	1.55	0.43	97.6	2.4
PUYU4-14-h	2	50.90	1.49	0.05	20.02	7.01	0.10	4.52	9.30	4.59	1.58	0.43	96.4	3.6
PUYU4-15-h	4	47.60	1.11	0.05	14.95	9.30	0.15	14.56	7.53	3.45	1.13	0.17	99.0	1.0
PUYU4-A12	4	49.47	1.71	0.02	22.02	6.62	0.17	1.85	11.76	4.30	1.57	0.51	97.3	2.7
PUYU4-A14	1	52.13	1.68	0.03	20.11	6.82	0.14	1.76	11.28	4.08	1.58	0.40	97.7	2.3
PUYU4-A16	1	51.17	1.61	0.00	21.23	6.43	0.16	1.89	11.36	4.15	1.57	0.43	99.2	0.8
PUYU4-A34	1	50.86	1.76	0.05	21.64	5.65	0.13	1.76	11.77	4.40	1.56	0.42	98.2	1.8
PUYU4-B12	3	58.26	1.93	0.00	18.62	4.52	0.10	1.10	6.15	5.38	3.60	0.34	98.1	1.9
PUYU4-B15	2	51.21	1.60	0.03	21.29	5.79	0.12	1.98	11.59	4.30	1.57	0.54	97.7	2.3
PUYU4-B16	1	50.54	1.71	0.05	21.67	5.97	0.09	1.49	11.64	4.59	1.74	0.49	98.0	2.0
PUYU4-B23	1	50.25	1.66	0.01	22.39	5.38	0.08	1.62	12.04	4.37	1.64	0.55	99.1	0.9
PUYU4-B25	1	51.09	1.47	0.05	19.32	8.04	0.15	3.25	10.81	4.02	1.39	0.39	99.0	1.0

Sample	MI type	SiO_2	TiO_2	Cr_2O_3	Al_2O_3	FeO*	MnO	MgO	CaO	Na_2O	K_2O	P_2O_5	Total	H_2O
PUYU4-B31	1	50.32	1.84	0.00	21.47	6.03	0.11	1.53	12.06	4.41	1.65	0.57	98.7	1.3
PUYU4-B33	3	50.44	1.63	0.00	21.96	6.29	0.07	1.42	11.48	4.59	1.64	0.48	99.1	0.9
PUYU4-B34	1	51.03	1.68	0.00	21.90	5.47	0.16	1.31	11.76	4.54	1.65	0.50	99.1	0.9
PUYU4-B41	2	50.66	1.64	0.04	21.93	5.70	0.07	1.70	11.63	4.50	1.61	0.51	98.7	1.3
PUYU4-C26	*1	54.76	2.34	0.00	18.22	4.29	0.09	0.81	8.70	5.94	4.23	0.61	97.6	2.4
PUYU4-C31	2	50.72	1.74	0.00	21.53	5.83	0.14	1.69	11.54	4.52	1.76	0.54	97.9	2.1
PUYU4-D31	2	50.97	1.69	0.05	22.33	4.87	0.09	1.53	11.58	4.72	1.62	0.55	96.7	3.3
PUYU4-D41	2	50.76	1.67	0.02	22.10	5.35	0.14	1.71	11.51	4.51	1.71	0.52	98.3	1.7
PUYU9-A21-a	1	48.91	2.66	0.00	20.26	6.44	0.11	1.81	12.65	4.17	2.39	0.59	97.6	2.4
PUYU9-A21-b	4	46.66	3.25	0.00	18.13	8.86	0.20	1.44	9.83	6.00	4.52	1.11	96.7	3.3
PUYU9-A4-a	2	47.94	2.84	0.00	17.37	9.62	0.23	1.88	9.68	5.29	4.22	0.91	99.2	0.8
PUYU9-A4-b	1	52.63	2.43	0.00	20.88	4.22	0.09	1.66	10.69	4.46	2.31	0.63	98.5	1.5
PUYU9-A43	2	46.45	2.56	0.01	20.60	7.45	0.15	2.35	12.70	4.27	2.62	0.82	96.8	3.2
PUYU9-A44	4	50.91	3.06	0.00	17.36	8.52	0.11	2.09	8.15	5.03	3.89	0.87	98.1	1.9
PUYU9-A45-105	4	48.04	2.77	0.00	17.53	9.76	0.18	2.32	9.81	5.03	3.68	0.88	98.4	1.6
PUYU9-A45-107	1	46.78	2.59	0.06	21.01	6.90	0.15	1.75	12.79	4.44	2.69	0.83	97.6	2.4
PUYU9-B21	4	48.02	2.74	0.02	18.29	8.35	0.14	2.25	11.62	4.68	3.06	0.83	97.8	2.2
PUYU9-B31-77	2	50.27	2.65	0.00	19.27	6.16	0.14	1.26	8.98	5.75	4.33	1.19	98.1	1.9
PUYU9-B31-79	2	50.19	2.56	0.00	19.57	6.13	0.19	1.43	8.58	6.02	4.32	1.01	99.1	0.9
PUYU9-B31-81	1	46.67	2.70	0.00	21.21	6.47	0.15	1.98	12.72	4.50	2.74	0.86	96.7	3.3
PUYU9-B32	4	47.73	2.75	0.00	17.26	9.68	0.17	1.96	10.46	5.59	3.77	0.64	97.7	2.3
PUYU9-B42	2	47.65	2.68	0.05	20.18	6.19	0.11	2.52	12.10	4.67	2.86	0.99	97.5	2.5
PUYU9-C32	1	47.52	2.44	0.07	20.29	7.19	0.12	1.97	12.91	4.12	2.58	0.80	97.8	2.2
PUYU9-C33	3	43.30	1.41	0.02	12.71	11.43	0.21	18.99	7.04	2.73	1.66	0.49	99.8	0.2
PUYU9-C37-15	*1	50.05	2.70	0.00	18.53	7.64	0.13	1.86	9.72	5.09	3.24	1.04	99.3	0.7
PUYU9-C37-18	*1	49.64	2.81	0.00	17.64	7.96	0.05	1.88	12.12	4.58	2.72	0.61	98.6	1.4
PUYU9-C38-14	*1	51.24	3.11	0.00	18.57	6.73	0.21	1.47	7.06	4.97	5.51	1.13	98.3	1.7
PUYU9-C43	4	46.51	2.71	0.00	20.10	7.07	0.16	2.14	13.11	4.46	2.80	0.96	97.6	2.4
PUYU9-C46-22	3	47.47	2.80	0.00	19.03	8.25	0.12	2.57	12.87	3.87	2.21	0.80	97.9	2.1
PUYU9-C46-23	1	48.55	2.75	0.00	20.37	6.12	0.13	1.72	13.32	4.01	2.25	0.77	97.7	2.3
PUYU9-C46-24	1	48.83	2.55	0.00	19.74	6.11	0.12	1.71	13.16	4.54	2.51	0.72	97.4	2.6

Sample	MI type	SiO_2	TiO_2	Cr_2O_3	Al_2O_3	FeO*	MnO	MgO	CaO	Na_2O	K_2O	P_2O_5	Total	H_2O
PUYU9-D12-41	3	32.52	3.21	0.06	29.32	6.83	0.11	3.34	14.89	5.58	3.60	0.52	62.8	37.2
PUYU9-D12-43	2	48.14	2.46	0.00	21.66	5.85	0.06	1.99	12.02	4.56	2.46	0.80	97.0	3.0
PUYU9-D13	4	47.77	3.19	0.00	19.17	8.13	0.11	1.35	9.70	5.24	4.50	0.85	98.1	1.9
PUYU9-D21	4	44.93	2.28	0.06	15.86	11.67	0.21	8.90	6.47	4.90	3.82	0.89	98.3	1.7
PUYU9-D32	2	48.43	3.04	0.00	19.87	6.11	0.13	1.90	12.83	4.38	2.44	0.88	97.5	2.5
PUYU9-D33-09	4	49.68	2.58	0.00	17.36	8.65	0.16	2.55	11.23	4.44	2.79	0.56	97.6	2.4
PUYU9-D33-66	4	47.71	2.61	0.00	18.35	8.70	0.20	2.51	11.34	4.79	2.98	0.80	97.3	2.7
PUYU9-D31-59	3	46.75	2.87	0.00	20.78	6.42	0.09	1.71	13.08	3.80	2.70	1.80	97.6	2.4
PUYU18-A11	*1	52.98	2.56	0.02	18.38	6.72	0.11	1.30	12.12	2.82	2.37	0.63	98.2	1.8
PUYU18-A13	*1	54.15	3.01	0.01	17.47	5.93	0.11	1.43	10.46	4.46	2.26	0.71	98.7	1.3
PUYU18-A21	1	50.80	2.40	0.00	21.78	5.42	0.07	1.87	9.77	5.27	1.93	0.70	98.5	1.5
PUYU18-A24-7	2	49.34	1.94	0.02	20.20	8.03	0.14	2.96	11.53	4.10	1.18	0.54	98.8	1.2
PUYU18-A24-8	1	49.83	2.16	0.04	20.88	7.62	0.11	2.45	10.38	4.91	1.11	0.50	99.0	1.0
PUYU18-A24-9	2	49.75	2.31	0.07	21.86	6.80	0.11	1.90	10.49	4.90	1.17	0.65	98.8	1.2
PUYU18-A32	2	53.82	2.40	0.00	17.78	6.92	0.07	1.56	10.37	2.66	3.34	1.08	98.0	2.0
PUYU18-A34-28	2	53.64	3.11	0.03	16.71	7.38	0.13	1.05	8.95	4.04	4.09	0.89	98.1	1.9
PUYU18-B11-93	*1	54.04	3.06	0.00	17.57	5.69	0.07	1.10	11.03	4.42	2.32	0.72	98.5	1.5
PUYU18-B21	3	52.69	1.97	0.05	19.96	6.08	0.12	1.81	11.20	3.47	1.96	0.69	98.2	1.8
PUYU18-B33	4	49.88	2.20	0.00	20.19	6.72	0.16	2.29	12.20	4.18	1.65	0.53	98.2	1.8
PUYU18-B37-66	4	50.37	2.87	0.04	16.07	8.31	0.15	1.47	10.17	7.49	2.47	0.58	99.4	0.6
PUYU18-B37-68	1	49.91	2.00	0.01	20.98	6.94	0.08	1.64	12.35	4.36	1.50	0.25	97.2	2.8
PUYU18-B38	1	49.96	2.26	0.00	20.75	6.84	0.14	1.89	11.32	3.88	1.92	1.04	98.5	1.5
PUYU18-B41-43	1	50.69	2.30	0.00	20.98	5.66	0.11	1.66	11.22	4.74	1.74	0.89	98.7	1.3
PUYU18-B41-45	1	51.07	2.31	0.01	21.00	5.25	0.07	1.59	11.23	4.81	1.83	0.83	98.5	1.5
PUYU18-B42	1	50.88	2.40	0.03	20.94	5.84	0.09	1.67	11.12	4.74	1.76	0.52	98.9	1.1
PUYU18-B43	*1	54.73	3.21	0.04	16.93	5.48	0.16	1.21	10.42	4.50	2.54	0.80	98.5	1.5
PUYU18-C11	1	49.97	2.16	0.01	20.58	7.28	0.14	2.02	11.85	3.75	1.70	0.55	99.0	1.0
PUYU18-C22	1	50.53	2.25	0.00	20.68	6.39	0.07	1.67	11.25	4.65	1.88	0.64	98.6	1.4
PUYU18-D22-116	2	50.65	2.32	0.06	19.89	6.35	0.11	2.07	11.59	4.43	1.74	0.79	98.8	1.2
PUYU18-D22-118	2	53.26	2.32	0.00	20.32	4.74	0.12	2.23	9.64	4.80	1.96	0.60	98.1	1.9
PUYU18-D24-114	*1	58.64	2.22	0.00	18.65	4.32	0.08	0.84	2.61	5.37	6.23	1.03	98.1	1.9

Sample	MI type	SiO_2	TiO_2	Cr_2O_3	Al_2O_3	FeO*	MnO	MgO	CaO	Na_2O	K_2O	P_2O_5	Total	H_2O
PUYU18-M-vtr1	2	52.91	2.07	0.00	22.27	4.88	0.09	1.64	10.58	3.22	1.73	0.61	99.2	0.8
PUYU18-M-vtr2	2	48.97	2.10	0.00	19.98	7.98	0.09	3.54	11.42	3.81	1.55	0.56	98.9	1.1
PUYU18-M-vtr3	1	49.77	2.16	0.00	21.60	6.39	0.07	1.91	10.79	4.90	1.77	0.65	98.0	2.0
PUYU18-M-vtr4	2	53.79	3.28	0.00	16.29	8.74	0.21	1.61	10.05	2.56	2.73	0.74	99.3	0.7
PUYU18-M-vtr5	1	51.04	2.12	0.02	20.80	6.32	0.06	2.00	10.83	4.48	1.68	0.67	99.2	0.8
PUYU18-M-vtr6	1	49.53	2.14	0.00	20.24	7.03	0.12	1.73	12.70	4.43	1.56	0.54	96.9	3.1

Table 9: melt inclusion trace element composition (ppm).

Sample	V	Cr	Ni	Cu	Rb	Sr	Y	Zr	Nb	Cs	Ba	La	Ce	Nd	Sm
PUYU3-A22_mi	238	-	72.4	-	40.3	1328	28.7	232.2	32.2	0.8	706	42.5	79.2	37.6	7.9
Puyu3-C7-MI	326	14.0	246.5	12.0	51.7	970	31.0	260.7	37.3	-	606	49.0	110.7	51.3	7.2
PUYU4_C1_M1	230	89.0	25.5	45.0	33.6	637	21.0	134.0	11.0	0.8	394	22.6	53.1	25.1	6.7
PUYU4_C1_M2	226	87.0	136.0	42.6	35.7	584	22.1	132.0	10.3	1.3	378	24.5	48.6	23.9	5.5
PUYU4_C1_M3	216	108.0	224.0	41.4	34.9	601	21.4	138.9	10.2	0.8	373	22.3	48.7	25.7	4.7
PUYU4_C2_M1	242	123.0	85.0	49.0	39.8	700	22.6	143.3	13.3	1.2	392	26.7	54.1	27.4	4.8
PUYU4_C5_MI	242	80.0	580.0	188.0	24.9	502	21.6	100.0	11.5		343	24.2	41.0	16.0	6.5
PUYU4_C11_MI_1	217	113.0	96.0	9.6	37.3	606	20.9	143.0	10.1	1.3	354	27.3	46.0	23.0	8.5
PUYU4_C7_MI_2	190	76.0	970.0	26.0	31.5	510	18.6	96.0	10.3		390	13.1	44.0	16.9	1.4
Secuencia4_C4_MI1	206	72.0	130.0	36.0	29.4	545	18.4	94.0	10.4	0.4	360	19.8	46.6	21.8	4.1
Secuencia4_C4_MI2	224	117.0	530.0	150.0	55.0	630	18.0	166.0	8.6		350	34.0	53.2	25.0	0.0
Secuencia4_C8_MI2	220	87.0	25.0	54.4	29.9	592	21.6	123.1	10.7	0.8	385	23.5	50.5	20.4	4.1
secuencia7_A14_Mi	235	67.0	0.0	4.9	39.5	605	25.3	135.0	10.5	0.3	370	25.1	55.0	20.1	2.7
secuencia7_A21_Mi	249	130.0	5.6	3.1	39.4	670	27.1	153.0	10.6	0.7	376	25.5	55.7	28.7	4.3
b25mi_0	226	74.0	6.6	39.3	42.7	670	21.6	138.9	11.2	1.2	393	25.3	56.5	27.2	4.7
b16mi_0	192	118.0	410.0	24.0	35.0	491	18.7	117.0	11.2	0.0	275	23.6	35.3	8.2	8.2
c31Mi_0	317	4.0	37.0	19.9	47.7	699	23.9	141.0	14.0		471	24.0	64.0	28.4	0.0
Secuencia5_A43_Mi	295	30.0	23.0	5.0	55.2	970	20.7	213.0	38.0	0.6	673	55.8	105.0	37.0	5.6
Secuencia5_A4_Mi1	299	18.0	0.3	113.0	72.7	790	27.2	287.0	59.4	1.0	868	68.7	125.0	63.8	7.1
Secuencia5_A4_Mi2	82	140.0	1500.0	14.0	17.7	380	4.6	53.0	4.4		157	16.8	17.9	13.0	1.3
Secuencia5_A44_Mi	298	16.5	0.0	80.0	108.0	773	27.7	315.0	70.2	1.3	949	77.0	132.0	59.0	10.1
Secuencia5_A45_Mi2	323	25.2	3.1	115.2	80.1	845	28.7	264.0	58.7	1.0	909	75.8	134.2	59.5	10.0
secuencia6MI_B31	272	116.0	131.0	15.0	55.0	830	28.0	242.0	51.0	1.7	760	47.0	109.0	27.0	3.2
secuencia6MI_B42	309	78.0	107.0	7.0	64.0	1170	24.4	296.0	54.1	0.4	830	67.0	107.0	50.0	14.3
secuencia6MI_C32	265	63.0	215.0	280.0	55.0	863	18.7	215.0	44.3	1.3	643	51.3	91.0	36.6	11.6

Sample	V	Cr	Ni	Cu	Rb	Sr	Y	Zr	Nb	Cs	Ba	La	Ce	Nd	Sm
secuencia7_D33_Mi	315	74.0	3.7	51.0	68.0	940	27.6	264.0	53.7	1.3	850	64.0	109.0	54.2	11.3
secuencia7_D12_Mi	460	100.0	210.0	0.0	113.0	1820	53.0	360.0	19.0	1.0	870	101.0	161.0	62.0	0.0
C4_MI	176	69.0	920.0	2.6	24.8	690	15.4	110.0	17.9	0.8	307	24.1	63.0	20.0	2.2
C5_MI	290	66.0	180.0	0.0	45.2	500	25.1	193.0	29.0	0.9	490	44.6	78.0	35.0	3.7
C1_MI	270	22.0	117.0	16.4	31.5	910	22.5	144.0	24.1	0.5	464	34.3	74.0	22.8	9.7
C6	305	83.0	17.0	15.0	36.8	910	23.7	149.0	24.7		473	33.1	66.0	40.0	4.0
PUYU18-A24-7	190	51.1	291.0	2.4	20.5	650	15.2	100.0	15.5	0.2	349	23.7	51.6	26.5	6.1
PUYU18-A24-8	234	34.0	49.0	3.1	15.5	404	21.3	101.9	6.1	0.3	268	13.8	38.7	16.3	4.0
Sample	**Pb**	**Th**	**Ta**	**Hf**	**Eu**	**Gd**	**Tb**	**Tm**	**Yb**	**Lu**	**Pr**	**Dy**	**Ho**	**Er**	**U**
PUYU3-A22_mi	6.4	7.3	1.9	6.6	1.9	8.1	1.1	0.3	3.4	0.4	8.3	5.2	1.1	3.5	1.6
Puyu3-C7-MI	6.0	10.4	2.3	5.3	3.1	6.8	1.1	0.2	1.2	0.3	13.1	5.4	0.9	3.0	1.6
PUYU4_C1_M1	6.0	3.2	0.6	2.8	2.7	5.3	0.6	0.3	1.3	0.2	6.1	2.5	1.2	2.0	0.7
PUYU4_C1_M2	5.4	2.9	0.8	2.4	1.9	4.9	0.8	0.4	2.2	0.0	6.7	3.2	0.7	2.2	0.6
PUYU4_C1_M3	7.6	3.5	0.5	3.3	1.4	3.7	0.9	0.2	2.4	0.2	6.0	3.7	1.0	2.0	0.9
PUYU4_C2_M1	8.3	3.3	0.7	3.5	2.1	4.9	0.6	0.3	2.1	0.6	6.2	5.2	0.8	2.8	1.0
PUYU4_C5_MI	8.2	3.1	0.0	0.9	0.8	3.9	0.2	0.1	0.7	0.1	5.1	1.9	0.0	3.0	0.1
PUYU4_C11_MI_1	8.5	4.9	0.2	2.6	0.0	1.1	0.2	0.0	0.0	0.2	5.1	5.5	0.3	0.5	1.2
PUYU4_C7_MI_2	4.8	4.2	0.2	3.3	0.7	3.9	0.4	0.0	2.7	0.2	5.0	1.6	0.2	1.2	0.2
Secuencia4_C4_MI1	8.2	3.3	0.6	3.5	0.7	5.6	0.7	0.3	1.8	0.1	5.6	3.8	0.5	2.7	0.9
Secuencia4_C4_MI2	15.8	5.5	0.0	0.0	2.4	0.0	1.4	0.0	0.0	0.0	5.6	5.5	1.4	0.0	0.9
Secuencia4_C8_MI2	5.7	4.1	0.6	2.8	1.2	4.3	0.6	0.5	2.3	0.2	5.1	4.7	0.8	2.4	1.0
secuencia7_A14_Mi	8.6	3.2	0.5	4.0	1.3	3.1	1.1	0.4	3.4	0.2	8.2	5.4	1.2	2.9	0.3
secuencia7_A21_Mi	7.5	4.1	0.5	3.5	1.5	6.1	0.7	0.4	2.7	0.3	6.6	4.4	1.3	3.4	1.3
b25mi_0	6.4	4.6	0.7	4.2	2.6	2.9	0.9	0.3	2.1	0.2	6.9	4.9	0.7	2.1	1.3
b16mi_0	0.0	3.0	0.9	0.0	0.6	12.0	0.9	0.0	0.0	0.0	1.7	5.0	0.4	1.0	0.9
c31Mi_0	6.9	4.6	0.2	2.0	1.7	4.8	0.6	0.0	2.4	0.4	5.6	4.6	0.6	2.0	0.0
Secuencia5_A43_Mi	8.0	9.2	3.3	7.8	2.7	5.4	0.4	0.1	2.2	0.1	12.0	4.1	0.9	0.0	1.6
Secuencia5_A4_Mi1	8.7	10.5	3.9	5.7	3.3	9.8	1.3	0.2	3.2	0.4	14.7	5.7	0.8	3.6	2.4
Secuencia5_A4_Mi2	0.0	0.3	0.0	0.0	0.0	1.2	0.0	0.0	0.0	0.0	2.2	4.3	0.0	1.8	0.0
Secuencia5_A44_Mi	8.9	11.5	4.4	7.6	3.6	8.1	1.5	0.7	2.8	0.5	16.1	5.2	0.6	2.3	1.9
Secuencia5_A45_Mi2	9.4	10.2	4.0	5.7	3.1	8.8	1.3	0.3	2.8	0.4	14.6	5.6	1.1	2.9	2.1
secuencia6MI_B31	7.0	7.9	1.6	4.0	0.8	8.0	0.4	0.3	0.0	0.3	8.8	0.0	2.2	0.0	2.1
secuencia6MI_B42	1.8	9.6	2.4	2.8	0.5	10.5	0.2	0.0	3.4	0.3	10.8	4.3	1.8	0.0	1.8
secuencia6MI_C32	12.7	7.9	2.8	8.4	3.1	0.0	0.4	0.0	1.9	0.5	8.7	7.1	0.0	0.5	1.7
secuencia7_D33_Mi	8.7	8.9	2.4	7.2	2.4	7.5	0.6	0.0	2.4	0.3	12.3	3.8	0.9	3.4	2.4
secuencia7_D12_Mi	19.0	21.0	7.8	17.0	0.0	0.0	0.0	0.0	0.0	0.0	14.0	0.0	2.8	0.0	6.4
C4_MI	6.3	3.0	1.8	1.7	0.8	5.2	0.3	0.2	1.1	0.0	4.7	4.6	0.3	0.0	1.7

Sample	Pb	Th	Ta	Hf	Eu	Gd	Tb	Tm	Yb	Lu	Pr	Dy	Ho	Er	U
C5_MI	4.6	5.7	0.8	6.3	2.0	9.0	0.1	0.6	2.2	0.6	10.5	5.2	0.4	1.0	0.7
C1_MI	5.1	5.0	0.6	3.3	1.6	7.3	0.7	0.3	1.5	0.2	7.1	3.7	0.6	2.0	1.4
C6	10.0	6.4	0.9	5.6	1.1	4.0	0.7	0.0	0.0	0.0	6.6	5.3	0.4	4.8	0.8
PUYU18-A24-7	7.0	5.3	0.9	2.7	0.9	3.5	0.5	0.1	1.5	0.1	5.9	2.6	0.7	1.1	1.2
PUYU18-A24-8	6.1	0.8	0.2	2.6	1.4	4.2	0.7	0.3	1.1	0.2	4.2	4.0	0.8	2.2	0.3

Table 10: Representative chemical analyses of olivine phenocrysts.

Sample	SiO_2	TiO_2	Al_2O_3	Cr_2O_3	FeO	MnO	MgO	NiO	CaO	Total
3-A 21 -107	41.00	0.02	0.06	0.00	21.97	0.47	36.15	0.08	0.00	99.75
3-A25-113	42.28	0.01	0.03	0.02	14.24	0.26	42.94	0.14	0.00	99.92
3-A31-120	41.33	0.01	0.03	0.01	15.54	0.28	42.48	0.11	0.00	99.79
3-B21-54	45.95	0.01	0.03	0.02	11.82	0.22	41.55	0.24	0.00	99.84
3-B42-26	42.34	0.01	0.03	0.00	17.58	0.28	39.30	0.16	0.00	99.70
PUYU18-A24-13	39.56	0.00	0.04	0.05	16.70	0.25	44.38	0.12	0.17	101.27
PUYU18-A32-21	39.91	0.00	0.06	0.03	15.81	0.26	45.66	0.20	0.18	102.10
PUYU18-B21-89	40.06	0.01	0.04	0.00	15.84	0.19	44.97	0.12	0.22	101.45
PUYU18-B26-85	39.84	0.00	0.05	0.00	15.59	0.21	45.03	0.24	0.21	101.17
PUYU18-B37-70	39.82	0.05	0.06	0.00	16.80	0.24	43.92	0.10	0.21	101.20
PUYU18-B41-44	40.11	0.02	0.05	0.03	15.79	0.28	45.65	0.17	0.23	102.33
PUYU18-B42-41	39.84	0.04	0.03	0.00	16.48	0.23	44.81	0.22	0.19	101.83
PUYU18-C22-123	39.88	0.01	0.01	0.00	15.43	0.28	45.33	0.24	0.17	101.34
PUYU18-C39-53	39.99	0.00	0.03	0.03	14.49	0.25	46.31	0.29	0.15	101.52
PUYU18-D16-112	39.95	0.03	0.05	0.01	15.35	0.24	45.37	0.11	0.16	101.26
PUYU18-M-01	39.77	0.00	0.00	0.04	16.05	0.24	45.25	0.18	0.19	101.72
PUYU18-M-03	39.94	0.05	0.00	0.01	15.67	0.20	45.33	0.24	0.21	101.65
PUYU18-M-05	39.75	0.03	0.00	0.03	15.39	0.24	45.66	0.23	0.14	101.47
PUYU18-M-07	39.68	0.00	0.00	0.04	15.98	0.28	45.22	0.30	0.17	101.67
PUYU18-M-11	39.69	0.00	0.00	0.04	16.81	0.24	44.50	0.18	0.24	101.70
Puyu3-A21-1	41.00	0.02	0.06	0.00	21.97	0.47	36.15	0.08	0.00	99.75
PUYU3-C7	46.82	0.00	0.04	0.03	8.42	0.16	43.91	0.33	0.00	99.71
Puyu3-D42-4	39.62	0.00	0.04	0.00	15.64	0.26	45.08	0.16	0.15	100.95

Sample	SiO_2	TiO_2	Al_2O_3	Cr_2O_3	FeO	MnO	MgO	NiO	CaO	Total
PUYU4-20	38.83	0.05	0.06	0.01	15.32	0.27	46.48	0.14	0.24	101.40
PUYU4-26	39.72	0.00	0.07	0.00	14.30	0.19	45.63	0.26	0.20	100.38
PUYU4-32	40.03	0.00	0.05	0.00	13.16	0.23	46.65	0.33	0.17	100.62
PUYU4-A14-7	39.89	0.03	0.03	0.06	14.23	0.23	45.80	0.28	0.19	100.74
PUYU4-A16-3	39.71	0.07	0.06	0.03	14.17	0.22	46.16	0.22	0.19	100.83
PUYU4-A34-21	39.56	0.00	0.02	0.00	16.95	0.26	44.04	0.16	0.21	101.19
PUYU4-B12b-27	39.35	0.05	0.05	0.00	17.50	0.34	43.64	0.04	0.18	101.15
PUYU4-B16-35	39.72	0.02	0.04	0.00	15.13	0.25	45.26	0.18	0.21	100.80
PUYU4-B18-41	39.86	0.00	0.02	0.00	15.01	0.27	45.04	0.19	0.26	100.65
PUYU4-B26-49	40.29	0.02	0.05	0.08	13.71	0.14	47.16	0.29	0.21	101.96
PUYU4-B33-83	40.01	0.00	0.03	0.07	15.62	0.24	45.45	0.18	0.23	101.82
PUYU4-B34-67	39.55	0.02	0.04	0.00	15.45	0.24	45.55	0.11	0.23	101.19
PUYU4-B39-85	40.23	0.00	0.02	0.02	13.12	0.20	46.24	0.32	0.17	100.31
PUYU4-B41-77	40.12	0.02	0.04	0.05	13.18	0.23	46.97	0.24	0.18	101.03
PUYU4-C11	39.15	0.01	0.03	0.02	18.36	0.23	41.61	0.27	0.00	99.68
PUYU4-C23-117	40.14	0.05	0.05	0.00	13.33	0.23	47.03	0.33	0.17	101.33
PUYU4-D32-108	40.33	0.00	0.12	0.09	12.55	0.20	46.81	0.28	0.16	100.53
PUYU9-A21-7	40.07	0.05	0.05	0.00	14.16	0.19	45.67	0.19	0.22	100.59
PUYU9-A43-98	39.60	0.06	0.04	0.02	15.17	0.19	45.29	0.22	0.26	100.85
PUYU9-A44-113	39.41	0.04	0.06	0.04	14.14	0.22	45.85	0.17	0.21	100.14
PUYU9-B21-19	38.01	0.02	0.06	0.00	22.47	0.40	39.46	0.04	0.17	100.63
PUYU9-B34-90	39.57	0.00	0.04	0.07	13.39	0.15	46.46	0.23	0.19	100.09
PUYU9-B41-115	40.00	0.04	0.03	0.04	14.23	0.19	46.30	0.20	0.21	101.23
PUYU9-C31-135	39.81	0.02	0.04	0.01	15.33	0.23	45.62	0.21	0.28	101.54
PUYU9-C32-72	39.18	0.09	0.07	0.00	15.64	0.22	44.41	0.16	0.28	100.05
PUYU9-C33-75	38.68	0.01	0.04	0.05	16.50	0.28	43.70	0.14	0.26	99.67
PUYU9-C42-139	39.52	0.02	0.05	0.05	15.17	0.21	45.22	0.22	0.25	100.70
PUYU9-C46-126	39.41	0.00	0.01	0.04	15.82	0.25	44.29	0.11	0.27	100.21
PUYU9-D12-45	38.91	0.07	0.06	0.04	14.08	0.22	45.90	0.21	0.19	99.68
PUYU9-D15	39.14	0.03	0.07	0.05	15.14	0.22	45.65	0.21	0.24	100.75
PUYU9-D33-68	39.29	0.03	0.05	0.07	12.75	0.15	47.44	0.37	0.20	100.34

Table 11: Representative chemical analyses of pyroxenes, whit the compositional classification calculated based on 6 oxygen.

Sample	SiO_2	TiO_2	Al_2O_3	Cr_2O_3	Fe_2O_3	FeO	MnO	MgO	CaO	Na_2O	TOTAL	Wo	En	Fs
PUYU-18-60	51.0	1.1	2.9	0.4	2.3	5.3	0.2	15.6	21.1	0.4	100.1	43.5	44.6	11.9
PUYU-18-61	51.7	0.9	2.3	0.3	1.8	5.4	0.2	15.9	21.2	0.3	100.0	43.3	45.3	11.4
PUYU9-A13 - Px 3	45.8	2.9	7.3	0.5	3.7	3.9	0.2	12.8	22.7	0.3	100.0	49.1	38.5	12.4
PUYU9-A31-92	46.1	2.7	7.7	0.4	3.2	4.2	0.2	12.6	22.6	0.4	100.2	49.4	38.3	12.3
PUYU9-A48-101	45.3	2.4	7.9	0.4	6.6	1.1	0.1	13.3	22.8	0.5	100.4	48.8	39.4	11.8
PUYU9-A49-104	48.6	1.8	4.6	0.1	4.2	4.3	0.2	14.2	22.0	0.4	100.3	45.6	41.1	13.2
PUYU9-B45-123	50.0	1.5	4.1	0.3	2.4	4.4	0.1	15.2	22.0	0.3	100.2	45.5	43.8	10.8
PUYU9-B45-124	44.5	3.1	9.1	0.6	4.2	3.8	0.1	12.2	22.5	0.4	100.4	49.6	37.4	13.1
PUYU9-C14-33	46.2	2.1	7.2	0.4	5.7	2.1	0.1	13.4	22.7	0.4	100.2	48.3	39.6	12.1
PUYU9-C14-34	49.5	1.5	4.0	0.2	4.2	2.9	0.1	15.3	22.4	0.3	100.3	45.8	43.6	10.7
PUYU9-C21-21	49.7	1.5	4.1	0.2	3.0	3.7	0.2	15.0	22.5	0.3	100.1	46.5	43.1	10.4
PUYU9-C21-22	45.5	2.7	7.9	0.4	4.9	2.7	0.1	13.0	22.7	0.4	100.4	49.0	38.9	12.1
PUYU 9 - C21 - Px 20	49.6	1.5	3.9	0.3	3.7	3.2	0.1	15.0	22.6	0.4	100.3	46.6	42.8	10.6
PUYU 9 - C21 - Px 21	49.7	1.7	3.7	0.1	2.8	4.9	0.2	14.1	22.7	0.3	100.1	47.1	40.6	12.3
PUYU9-C37 - Px 108	45.1	3.1	7.9	0.6	3.0	4.8	0.1	12.8	22.6	0.0	100.1	48.8	38.4	12.7
PUYU9-C44-146	50.2	1.4	3.7	0.2	2.8	3.8	0.1	15.3	22.3	0.3	100.2	45.8	43.8	10.4
PUYU9-C44-147	44.7	3.1	8.9	0.4	4.4	3.6	0.2	12.3	22.4	0.3	100.3	49.3	37.7	13.0
PUYU9-C44-148	49.8	1.4	3.9	0.3	3.2	3.7	0.2	15.1	22.4	0.3	100.2	46.0	43.3	10.7
PUYU9-C44-149	46.1	2.4	6.8	0.0	5.7	3.4	0.1	12.8	22.5	0.5	100.3	47.9	37.8	14.3
PUYU9-D15 - Px 101	45.6	3.1	7.0	0.1	5.2	5.5	0.1	12.2	21.6	0.4	100.9	46.4	36.5	17.0
PUYU9-D15 - Px 102	44.2	3.6	8.0	0.1	5.4	5.7	0.2	11.3	21.2	0.6	100.4	46.9	34.7	18.4
PUYU9-D21-57	45.9	2.2	7.3	0.4	5.9	1.9	0.1	13.4	22.7	0.4	100.2	48.3	39.8	11.9
PUYU 9 - D14 - Px 56	49.5	1.4	3.9	0.3	3.6	3.6	0.1	14.9	22.4	0.3	99.9	46.2	42.7	11.1
PUYU 9 - D14 - Px 57	44.2	3.3	8.0	0.5	5.5	2.7	0.1	12.2	22.6	0.5	99.6	49.7	37.2	13.1
PUYU 9 - D14 - Px 60	46.1	2.7	7.4	0.5	4.3	3.1	0.1	13.1	22.9	0.4	100.7	49.1	39.1	11.8
PUYU 9 - D23 - Px 84	50.6	1.3	3.7	0.3	1.5	4.3	0.1	15.2	22.2	0.3	99.5	46.5	44.3	9.3

Table 12: Results of the calculation of the structural formula of plagioclase based on 32 oxygen.

Sample	Si	Ti	Al	Fe(ii)	Ca	Na	K	TOTAL	An	Ab	Or
PUYU4-B37-79	2.27	0.00	1.72	0.02	0.72	0.26	0.01	5.0	72.6	26.4	1.0
PUYU4-B37-80	2.28	0.00	1.70	0.02	0.72	0.26	0.01	5.0	73.2	26.0	0.9
PUYU4-B38-63	2.28	0.01	1.69	0.02	0.72	0.27	0.01	5.0	71.9	27.2	0.9
PUYU4-B38-64	2.36	0.00	1.62	0.02	0.65	0.31	0.01	5.0	66.4	32.1	1.4
PUYU4-B-62	2.30	0.00	1.68	0.02	0.71	0.28	0.01	5.0	71.3	27.8	0.9
PUYU4-B-90	2.31	0.00	1.66	0.02	0.70	0.29	0.01	5.0	69.9	29.0	1.1
PUYU4-B-91	2.37	0.00	1.60	0.03	0.65	0.33	0.02	5.0	65.2	33.3	1.5
PUYU4-C26-114	2.34	0.00	1.64	0.03	0.68	0.29	0.01	5.0	69.0	29.7	1.3
PUYU 9 - A13 - Pl 6	2.28	0.00	1.70	0.03	0.72	0.26	0.02	5.0	72.2	26.0	1.8
PUYU 9 - A13 - Pl 7	2.31	0.00	1.67	0.03	0.70	0.27	0.02	5.0	70.5	27.5	2.0
PUYU 9 - A13 - Pl 8	2.26	0.01	1.71	0.03	0.72	0.27	0.02	5.0	71.4	26.6	2.0
PUYU 9 - D14 - Pl 61	2.31	0.01	1.67	0.02	0.70	0.28	0.02	5.0	70.1	27.8	2.0
PUYU 9 - D14 - Pl 62	2.30	0.01	1.67	0.03	0.70	0.27	0.02	5.0	70.9	27.1	2.0
PUYU9-A22-15	2.34	0.01	1.63	0.04	0.64	0.33	0.03	5.0	63.9	33.2	2.9
PUYU9-A31-94	2.30	0.00	1.68	0.02	0.70	0.28	0.02	5.0	69.9	27.9	2.2
PUYU9-C13-29	2.28	0.00	1.70	0.02	0.71	0.27	0.02	5.0	70.7	27.3	2.0
PUYU9-C13-30	2.29	0.00	1.69	0.03	0.69	0.28	0.02	5.0	69.7	28.2	2.0
PUYU9-C21-24	2.28	0.00	1.71	0.03	0.71	0.26	0.02	5.0	71.8	26.2	2.0
PUYU9-C22-27	2.28	0.01	1.71	0.02	0.71	0.27	0.02	5.0	70.9	27.1	2.1
PUYU9-C22-28	2.27	0.00	1.72	0.03	0.71	0.25	0.02	5.0	72.3	25.7	2.0
PUYU9-C36-130	2.28	0.00	1.69	0.03	0.71	0.28	0.02	5.0	70.4	27.5	2.1
PUYU9-C44-150	2.29	0.00	1.68	0.03	0.71	0.28	0.02	5.0	70.2	27.6	2.2
PUYU9-C44-151	2.30	0.01	1.66	0.04	0.70	0.29	0.02	5.0	68.9	28.7	2.4
PUYU9-D35-129	2.27	0.01	1.72	0.03	0.71	0.27	0.02	5.0	71.1	26.9	2.0
PUYU9-D31-63	2.30	0.00	1.67	0.03	0.70	0.28	0.02	5.0	69.9	28.1	2.0
PUYU9-D31-64	2.29	0.00	1.69	0.04	0.70	0.27	0.02	5.0	70.5	27.5	2.1
PUYU-18-48	2.30	0.00	1.67	0.03	0.73	0.26	0.01	5.0	72.9	26.1	1.0
PUYU-18-49	2.28	0.00	1.68	0.03	0.73	0.27	0.01	5.0	72.0	27.1	0.9
PUYU-18-64	2.33	0.00	1.63	0.03	0.69	0.30	0.02	5.0	68.3	30.1	1.6
PUYU-18-65	2.35	0.00	1.61	0.04	0.68	0.31	0.02	5.0	67.4	31.0	1.6

Sample	Si	Ti	Al	Fe(ii)	Ca	Na	K	TOTAL	An	Ab	Or
PUYU-18-95	2.37	0.00	1.60	0.04	0.65	0.32	0.02	5.0	65.8	32.4	1.9
PUYU-18-96	2.37	0.01	1.59	0.04	0.65	0.33	0.02	5.0	65.1	32.8	2.1